Cranfield University

Benjamin R Wakeling

Close space sublimation of CdTe for solar cells and the effect of underlying layers

Cranfield Defence and Security

PhD Thesis

Cranfield University

Cranfield Defence and Security

Department of Applied Science, Security and Resilience

PhD Thesis

Academic Year 2008 - 2009

Benjamin R Wakeling

Close space sublimation of CdTe for solar cells and the effect of underlying layers

Supervisor: Dr D. W. Lane

August 2009

This thesis is submitted in partial fulfilment of the requirements for the degree of Doctorate of Philosophy

Abstract

This work has focused on the design, construction and testing of a close space sublimation system for CdTe deposition. In addition, it also focused on variations to the treatment and fabrication procedures of the transparent conducting oxide and CdS layers prior to the CdTe deposition, in order to influence the structure and electrical properties of the CdTe/CdS interface.

CdTe was deposited by the physical vapour process, close space sublimation. The equipment used was custom built for this work and is therefore described in detail. Some of the deposition parameters of the equipment were varied in order to allow a comparison between the equipment in this work and those reported in the literature.

Bilayers of CdS have been created by depositing two individual CdS layers, on top of one another, whilst also varying the annealing treatment of the first layer. These bilayers were included in devices and which subsequently underwent a series of etches to allow analysis of the materials. The bilayers were shown to effect the preferred orientation of the CdTe layer deposited on top, but the results suggested the bilayers had a negative effect on the amount of current recombination in the depletion region.

The roughness of the transparent conducting oxide coated glass substrates used in this work, was proposed as a way of influencing the roughness of the CdS layer deposited on top and therefore the roughness of the layer the CdTe is deposited on. It was proposed that the CdTe material deposited on a roughened substrate may have an increased grain size; no evidence for this was found for samples including CdS layers. A second phase of CdTe was observed and assigned to the presence of a CdS_xTe_{1-x} alloy. The sulphur content of the alloy was found to increase as the roughness of the substrate increased.

CdS was deposited by the wet chemistry process chemical bath deposition. In situ monitoring of the deposition was carried out by studying the reflection of light from the interface at the end of an optical fibre placed within the solution. The results indicated

that the in situ monitoring was sensitive to the initial deposition but the sensitivity reduced as the film thickness approached 150 nm. The in situ monitoring technique and ellipsometry measurements of the CdS showed good agreement with the theory of two deposition mechanisms occurring during the deposition. The results showed that CdS grown by chemical bath deposition has a two layer structure consistent with; a low density CdS grown by homogeneous deposition, on top of dense CdS grown by ion by ion deposition. An ellipsometry model for the CdS and CdTe layers is presented, along with its optical properties over the wavelength range 245 to 1690 nm.

Contents

List of Figures

Acknowledgments

I would like to thank my supervisor Dr. D W Lane for his help and guidance throughout this work.

I have received assistance and help from many people and I would like to thank: Prof. K D Rogers for his assistance throughout the work and specifically relating to X-ray diffraction, Mr M Sellwood for his technical support with the design and construction of the close space sublimation equipment, Dr J D Painter for his help and advice, and Mr A J Mustey and Dr. J W Rock for their general assistance. Also thanks to Dr. G Kister and Dr. R B Degamber for their help with the work on optical fibres.

Special thanks for the support I received from a fellow student Dr. S Roncallo.

I would like to gratefully acknowledge the assistance and advice I received from Dr. M A Cousins.

During this project I have also received assistance from Prof K Durose and Mr M Alturkestani at Durham University who deposited some CdTe. Thanks also to Dr. C Jeynes and Dr. M Webb from Surrey University ion beam facility for their help with analysing the optical fibre data. Thanks also to G K Pribil from the J. A. Woollam Co. for his assistance with ellipsometric analysis.

This work was funded by the EPSRC under grant number EP/P501/776/1 and also as part of the SUPERGEN Consortium, Photovoltaic Materials for the 21st Century.

I also wish to thank my parents and Stephanie for their support.

Chapter 1

Introduction

1.1 Background

Global warming and concerns over dependence on foreign energy supplies have caused governments to increase funding for renewable energy projects. In 2007, 44 % of the total energy supply for the UK was imported, while the UK produced 545.7 million tonnes of carbon dioxide compared with 589.5 million tonnes in 1990 [1]. The European union is committed to reducing in greenhouse emissions to at least 20 % below the 1990 level by 2020 (2008/101/EC). The current government have targeted cutting UK greenhouse gas emissions by 34% of the 1990 levels by the year 2020 [2].

Renewable energy encompasses: wind, hydroelectric, geothermal, bio fuels and solar power. Solar energy can be harnessed in several ways, including using the light to heat water either to produce hot water or to generate steam for electrical production. Photovoltaic solar cells convert sun light directly into electricity. 5 % of the UK electricity was generated by renewable energies in 2007, with 47 % of the renewable electricity produced from biomass sources [1]. While across Europe 15.6 % of the gross electricity consumption was generated from renewable sources [3], see figure 1-1.

Currently the cost of electricity produced by photovoltaic solar cells is higher than that from fossil fuels, although cost parity is dependent on fossil fuel prices. Government subsidies and policies have been implemented as a way of making the photovoltaic solar cells financially competitive. One proposed outcome of such policies was to reduce the cost of solar cell manufacture through increasing production capacity and thereby bringing down the cost of each unit. Governments can use feed-in tariff policies which

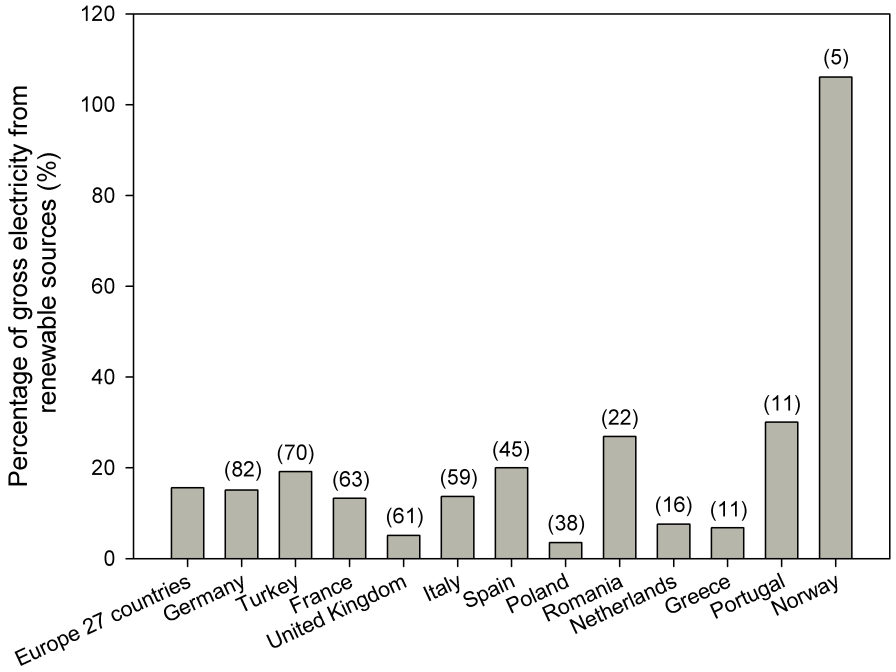

Figure 1-1: Electricity generated from renewable energy sources as a percentage of the gross national electricity consumption, for a selection of European countries, from 2007 [3]. The numbers in brackets are the populations of the countries in millions.

obliges utilities to buy the electricity produced by small scale electrical generators at a set minimum price. These feed-in tariffs can guarantee an investor a certain percentage return on investment and encourage participation in the scheme on a range of generating scales [4].

The Marketbuzz 2009 annual report of the world photovoltaic industry, reported 73 % of the 5.95 GW installed in 2008 was installed in either Germany or Spain [5]. This can be linked with these countries having developed feed-in tariff policies. The rapid growth of the industry is highlighted by the 110 % growth in the installed capacity in 2008. The total revenue of the global photovoltaic industry in 2008 was 37.1 billion US dollars.

1.2 Physics of solar cells

The solar spectrum at the surface of the earth is influenced by the absorption and scattering which takes place as the light passes through the atmosphere. To allow solar cell devices to be compared, standardised solar spectrum have been developed. The Air Mass

(AM) is used to indicate how absorption due to the atmosphere has affected the spectral content of the light. The *AM0* solar spectrum represents the spectrum in space above the Earth's atmopshere and it is similar to that of black body irradiance for a material as hot as the sun (5489℃), see figure 1-2. At the Earth's surface the value of the air mass can be calculated from the equation:

$$AM = \frac{1}{cos\theta} \tag{1-1}$$

Where θ is the angle incidence (with $\theta = 0$ when the sun is directly overhead) [6]. A solar spectrum of *AM1.5* is widely used as the standard for representing the spectrum for terrestrial applications and corresponds to a solar zenith angle of 48.19 °. Standardised solar spectrum can include a diffuse light component ('G' for global), or only the direct light component is represented ('D'). The intensity of the light has also been standardised to 1000 W/m^2.

As a comparison of the intensities measured in different locations the work by Craggs *et al.* found that the maximum irradiance in Newcastle (UK) in June to be 913 W/m^2 while the average was 227 W/m^2 [8]; simiarly work by Martinez-Lozano *et al.* measured the irradiance in Madrid (Spain) in June and found the maximum to be 1001 W/m^2 with

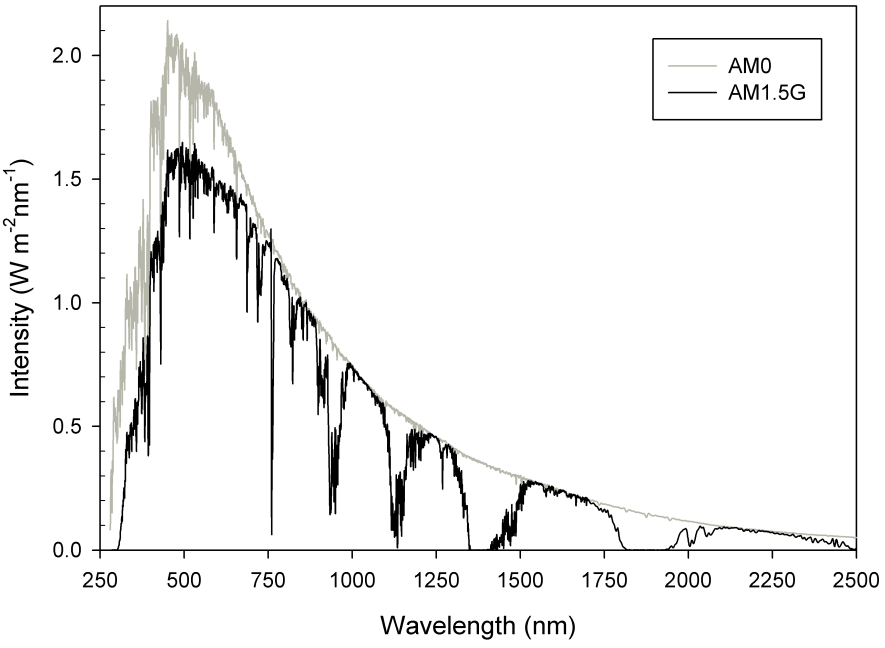

Figure 1-2: Examples of standardised solar spectrums, with the absorption due to atmosphere visible in AM1.5G spectrum [7].

an average of 490 W/m^2 [9].

The band gap (E_g) in a semiconductor is the energy difference between the top energy states of the valence band and the bottom states of the conduction band. In a direct band gap semiconductor, a photon of light with an energy greater then the band gap, can excite an electron from the valance to the conduction band, creating an electron hole pair. Similarly an electron in the conduction band can recombine with a hole in the valence band by a recombination process emitting radiation.

The Fermi level within a semiconductor at absolute zero denotes the energy above which all the states are empty, while all the states below this energy are full of electrons [6]. The addition of dopants to an intrinsic (undoped) material causes the Fermi level to move. A dopant is an atom with a different valency to the intrinsic atoms. If an atom has a valency one larger than the intrinsic atom (a donor) it will contribute the same number of electrons to its neighbours as an intrinsic atom, and it would also contribute an extra electron to the conduction band. An acceptor dopant has a valency of one less than the intrinsic atoms, and accepts an electron from the valence band creating an extra hole.

Two semiconductors with different energy levels can be joined together to form a pn junction, see figure 1-3. One of these materials has a Fermi level closer to the conduction band than the valance band, and is described as n-type material (electrons are the primary source of electrical conduction (the majority carrier)). While the other material is p-type with holes acting as the majority carrier. When the two types of material are joined together the majority carriers diffuse across the interface: Whereas the atoms with the different energy levels stay in their original positions. This causes each material to become charged in the region of the interface. The holes and electrons in this region recombine and create a depletion region, that is a region with a low number of carriers. The charges form a potential (an internal voltage) at the interface. If a photon is absorbed within a diffusion length of the depletion region the hole and electron it creates, can be separated by the potential, generating a current.

The electrical characteristics of a solar cell can be represented by an equivalent electrical circuit, see figure 1-4. The I_{sc} is an ideal current source and the circuit includes the series (R_S) and shunt (R_{Sh}) resistors. Two diodes are also present within the circuit, one represents recombination in the quasi neutral region (with an idealitiy (quality) factor of 1) while the other represents recombination in the depletion region (with an idealitiy

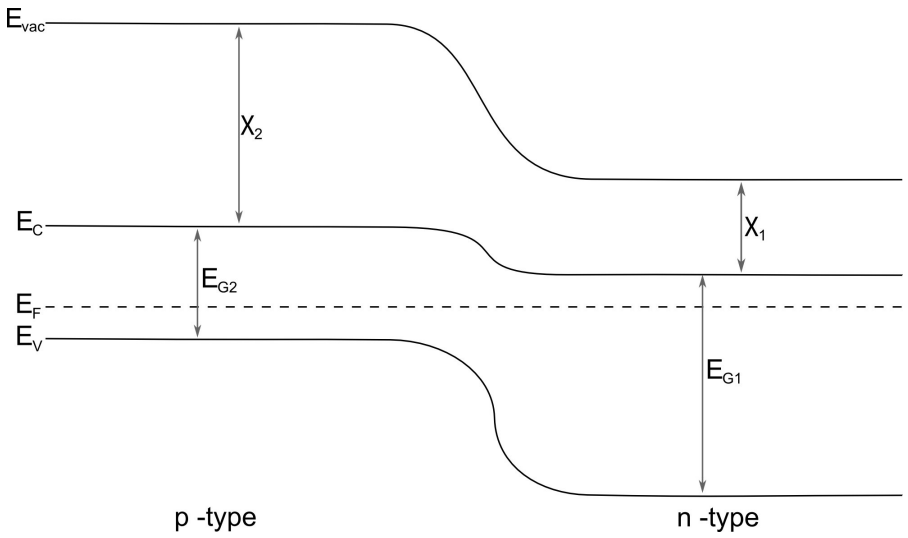

Figure 1-3: An energy band diagram of a semiconductor pn junction. Where E_{G1} and E_{G2} are the band gap energy of the two semiconductors, χ_1 and χ_2 and the electron affinity of the materials. The electron affinity is the energy required to remove an electron from the bottom of the conduction band to an energy level outside the material.

factor of 2) [6].

The current (I) produced by the solar cell can be described by equation 1-2. Where I_{01} and I_{02} are the dark saturation currents due to recombination, in the quasi-neutral regions and in the depletion region respectively, k is Boltzmann's constant, T is the absolute temperature, q is the magnitude of the charge on an electron, and V is the voltage across the solar cell.

$$I = I_{sc} - I_{01}\left(e^{q(V+IR_s)/kT} - 1\right) - I_{02}\left(e^{qV+IR_s)/2kT} - 1\right) - \frac{(V - IR_s)}{R_{sh}} \tag{1-2}$$

This expression can be rewritten with only one diode component, with this diode

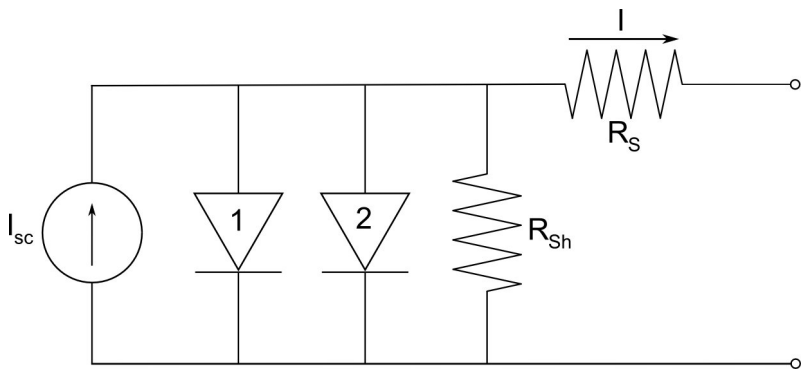

Figure 1-4: An equivalent circuit diagram of a solar cells electrical characteristics.

having an ideality factor between 1 and 2. In this case the diode ideality factor would be an indication of which region within the device the recombinations were dominant.

The major electrical characteristics of a solar cell can be assessed from plotting the current against the voltage (I-V curve), see figure 1-5. The short circuit current (I_{sc}), is the current produced by the device when a zero ohm load is applied to the cell. The open circuit voltage (V_{oc}) is the voltage when the load has been removed and no current is produced by the device. The maximum power point (V_{mp}, I_{mp}) defines the values of the voltage and the current where the power produced is at a maximum.

The fill factor (ff) describes the squareness of the I-V curve, see equation 1-3.

$$ff = \frac{V_{mp}I_{mp}}{V_{oc}I_{sc}} \tag{1-3}$$

The efficiency of a solar cell is the ratio of the maximum power of the cell over the incident power (P_{in}), with the efficiency of a cell given as a percentage, see equation 1-4. The incident power is determined from the irradiance of the light multiplied the surface area of the solar cell. The definition of the solar cell area is therefore an important

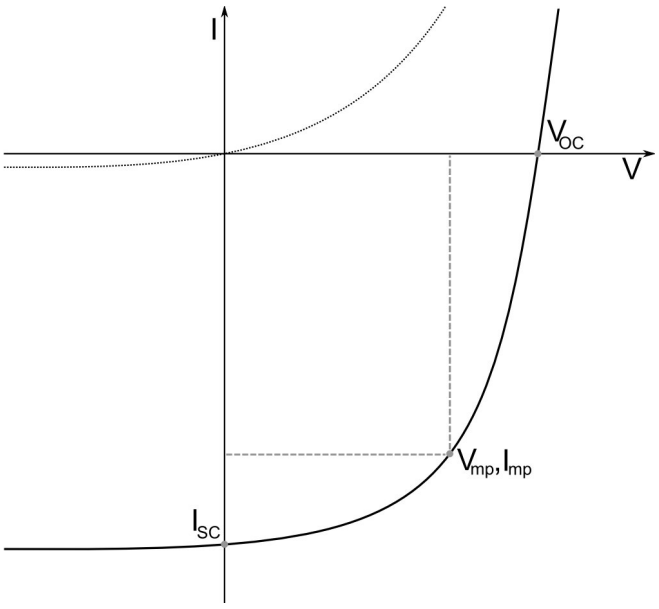

Figure 1-5: I-V plot for an unilluminated response (dotted line) and illuminated response (solid line). The short circuit current (I_{sc}), open circuit voltage (V_{oc}) and the maximum power point (V_{mp}, I_{mp}) are displayed.

consideration in efficiency measurements.

$$\eta = \frac{V_{mp} I_{mp}}{P_{in}} \tag{1-4}$$

The effect of the series and shunt resistance on I-V curves is presented in figure 1-6. The open circuit voltage is independent of the R_s, while the short circuit current is independent of the R_{sh}.

The equivalent circuit diagram described here applies to a solar cell with ohmic contacts. However a rectifying contact (Schottky barrier) can be formed between one of the semiconductor materials and a metal contact. In an ohmic contact, at low voltage, the current varies linearly with the voltage. The work function of a material is the difference in energy between the Fermi level and the energy of free space outside the solid. If the work function of a p-type semiconductor is larger then the work function of the connected metal, a rectifying contact will occur (the opposite is true for an n-type semiconductor).

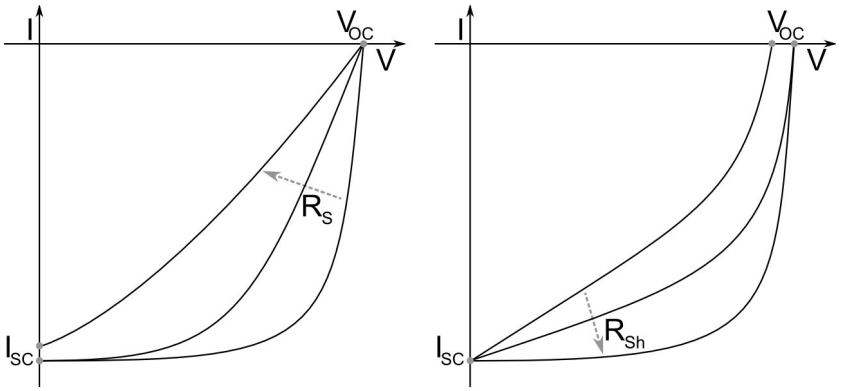

Figure 1-6: Illustrates how varying the R_S and R_{Sh} effect the I-V curve

1.3 Photovoltaic research

There are currently several different types of materials and technologies used in photovoltaic solar cell modules that are commercially available or being researched. To compare different devices the efficiency can be used, however the cost per Watt (typically US $/W) allows a commercial aspect of the modules to be evaluated. The cost per Watt uses the maximum power of the module under standard test conditions.

There are several different approaches being implemented to try and reduce the cost of photovoltaic solar cell modules. The monocrystalline silicon wafer modules have a

high efficiency (23 % [1]) but the cost of producing the semiconductor material causes the module price to be high. Polycrystalline silicon reduces the material cost and still produces good efficiencies (20 %). One approach to reducing the cost of the module is to use a concentrator to increase the solar flux on the module. This reduces the overall cost due to the fact that the concentrator is cheaper to produce than the solar modules. Tandem solar cells are multiple solar cells with different band gaps stacked on top of each other and these devices can reach efficiencies around the 30-40 % on a small scale. Tandem solar cells are very expensive but are suited to systems involving considerable concentration of the light. Nanotechnologies can also be applied to solar modules to improve efficiencies, relying on quantum optics.

To reduce the cost of photovoltaics another approach involves using very thin layers of the semiconductor materials and thereby reducing the material costs of the devices. These thin film solar modules have lower efficiencies but are cheaper to produce and can be fabricated on large areas. Thin film solar modules require a material with a high absorption coefficient to ensure the maximum amount of the available light is absorbed within the thin layers. The band gap of the material should also be close to the theoretically calculated optimum band gap ($1.1 \leq Eg \leq 1.6\,eV$) which produces the maximum efficiency for a single junction device under terrestrial solar illumination [11]. Amorphous silicon thin film solar modules (10 %) have a low absorption coefficient due to it being an indirect semiconductor. Cu(InGa)Se_2 (CIGS) (14 %) are the highest efficiency thin film solar modules. The third main thin film technology is cadmium telluride (11 %), which will be discussed in more detail in section 1.4.

Dye sensitised solar cells (10 % small area cell) work slightly differently to conventional cells, using dyes to absorb the light and form an exciton (an electron hole pair). The exciton then move to an interface (between an n- and p-type material) where the electron and hole are separated.

[1] The efficiencies presented in this section are the best module efficiencies unless stated otherwise [10].

1.4 Introduction to cadmium telluride/cadmium sulphide solar cells

The binary compound cadmium telluride (CdTe) is an ideal candidate for thin film solar cells due to its near ideal band gap of 1.45 eV and its optical absorbance coefficient which is greater than $1 \times 10^5\,\mathrm{cm}^{-1}$ (this means 90 % of the light which could be absorbed, is absorbed in the first few microns) [12]. Cadmium sulphide is regularly used as a n-type partner to p-type CdTe to form the thin film solar cell's pn junction. It is this type of device that is examined in this thesis.

The environmental impact and sustainability are an important aspect of any industrial process, this encompasses the availability of materials and their toxicity. Cadmium is a by product of zinc and lead refining, while both cadmium and tellurium can be refined from the copper refining process. Cadmium has widely been incorporated into batteries and also used in pigments, plating and as a plastic stabiliser [13]. The European Union has recently brought in legislation (2006/66/EC) to reduce the amount of hazardous material released into the environment; this includes the restriction that no more than 0.002% of cadmium (% by weight) may be incorporated into portable batteries (with some exceptions).

The major concern with CdTe base devices is the toxicity of the cadmium and tellurium. Studies have shown CdTe is a lung carcinogen and over a long period of time can damage the kidney and the liver [14]. The health risks to the workers and consumers, as well as the environmental effect have had to be examined carefully as there could be significant negative effect, of wide spread application of this technology. Research has shown water collected off of broken CdTe modules to have a concentration of Cd no higher than the level of CdTe allowed by the German drinking water limits [15]. While long term monitoring of employees in CdTe photovoltaic production lines has shown no significant occupationally related Cd exposure [14]. Controlling the distribution and disposal of the material is also a concern, with an economic and environmental way of recycling old CdTe modules being proposed [16].

CdTe solar modules are commercially available and produced by several companies. ANTEC solar GmbH produces CdTe solar modules using a process which involves close space sublimation. First Solar are one of the largest produces of CdTe modules with a

$ 1.2 billion revenue in 2008, and a reporting manufacturing cost of 0.93 $/W in the first quarter of 2009, producing modules with an average module efficiency of 10.9 %, [17], this is possibly one of the lowest manufacturing costs in the industry. The reduction in cost may be partially attributed to their single line module manufacturing process which creates a module on a sheet of glass in approximately 2.5 hours.

This project was concerned with the development of a piece of equipment to deposit CdTe by close space sublimation. Then through the fabrication of devices the structural properties of CdTe/CdS were investigated in order to improve the understanding of the fundamental processes and mechanisms involved. This is with a goal of furthering the knowledge of these complex devices to enable refinements of current fabrication processes.

1.5 Thesis outline

An outline of the remaining parts of this thesis is presented in this section. The second chapter gives an overview of research into CdTe/CdS solar cells, focusing on research into interdiffusion between the CdTe and CdS, and the effect of the CdTe crystallographic quality on the device performance. Chapter three describes the device process procedures as well as outlining the analytical techniques used in this work. This includes an explanation of the X-ray diffraction analysis, the Ellipsometry models and the analysis used to extract parameters from the current voltage data.

A chemical bath deposition process was used to deposit the CdS and it is discussed in chapter four. This deposition procedure does not have a well defined starting point, and an in situ fibre optic monitoring technique was developed to monitor the thickness of the deposited film.

CdTe was deposited by close space sublimation using a custom-built vacuum system. In chapter five this equipment is described in detail and it also lists the deposition parameters which were varied to produce a series of experimental samples. The effect of the deposition parameters on the deposited films was analysed and compared to results in the literature. This was done to determine if the equipment built in this work was comparable with those used by other research groups.

A hypothesis of the current work was that through depositing two layers of CdS, the second deposition on top of the first, it maybe possible to gain better control over

the properties of the CdS layer within the final device, and this proposal is investigated in chapter six. CdS 'bilayers' were created with different treatments to the CdS layer deposited first. These bilayers were included in devices and then destructively analysed to see the effect of the treatments.

Chapter seven developes another concept from the observation of a possible increase in the grain size of CdTe grown on scratched substrates. Transparent conducting oxide substrates were deliberately roughened and the effect on the CdS and CdTe layers deposited on top are reported. The conclusions and further work of the project are presented in chapter eight.

References

[1] I. MacLeay, K. Harris, and C. Micheals, *Digest of United Kingdom Energy Statistics* (A National Statistic Publication, 2008).

[2] National strategy for climate and energy, *The uk low carbon transition plan* (2009).

[3] European Communities, 1995-2009, *Electricity generated from renewable sources*, http://epp.eurostat.ec.europa.eu/tgm/table (Accessed: 11th June 2009).

[4] K. Cory, T. Couture, and C. Kreycik, Tech. Rep., NREL - National Renewable Energy Laboratory (2009).

[5] Solarbuzz, LLC, *World pv industry report summary*, http://www.solarbuzz.com/Marketbuzz2009-intro.htm (Accessed: 13th June 2009).

[6] A. Luque and S. Hegedus, *Handbook of Photovoltaic Science and Engineering* (John Wiley & Sons, 2003).

[7] NREL, *Reference solar spectral irradiance: Astm g-173*, http://rredc.nrel.gov/solar/spectra/am1.5 (Accessed: 29th June 2009).

[8] C. Craggs, E. M. Conway, and N. M. Pearsall, Solar Energy **68**, 179 (2000).

[9] J. A. Martinez-Lozano, F. Tena, and M. P. Utrillas, International Journal of Climatology **19**, 903 (1999).

[10] M. A. Green, K. Emery, Y. Hishikawa, and W. Warta, Progress in Photovoltaics **17**, 85 (2009).

[11] J. Loferski, Journal of Applied Physics **27**, 777 (1956).

[12] D. Bonnet, Thin Solid Films **361**, 547 (2000).

[13] M. Raugie, in *23rd European Photovoltaic Solar Energy Conference* (2008).

[14] Deparment of energy (DOE), and Brookhaven National Laboratory (BNL), *Nomination of cadmium telluride to the nationnal toxicology program* (2003).

[15] H. Steinberger, Progress in Photovoltaics **6**, 99 (1998).

[16] R. Sasala, J. Bohland, and K. Smigielski, in *25th IEEE Photovoltaic Specialists Conference* (1996), p. 865.

[17] First Solar, *Fast facts: Company overview*, www.firstsolar.com (Accessed: 16th June 2009).

Chapter 2

CdTe/CdS solar cells

2.1 Introduction

This chapter reviews published work on CdTe/CdS solar cells. There is a large amount of research which has been carried out in this field over the last forty years, what is presented here is an overview of some of the more important issues that relate to research undertaken in this project.

2.2 Structure of a device

This section gives a brief overview of the structure and required characteristics of the layers within a generalised CdTe/CdS solar cell. Devices are generally formed on transparent conducting oxide (TCO) coated glass. The glass provides structural support for the device, and in the superstrate configuration (see figure 2-1) the light passes through the glass before being absorbed by the semiconductor material. Therefore the optical transmission of the glass is required to be as large as possible. The properties of the TCO are a compromise between being as thin as possible to maximise the optical transmission and having a low electrical resistance. The TCO may also need to stop impurities within the glass diffusing into the semiconductor material [1].

The CdS layer needs to be thin to allow as much light through to the absorber layer, whilst being thick enough to cover the front contact and to create a p-n junction with the CdTe. The CdS has a wurtzite (hexagonal) structure and the CdTe has a zincblende (cubic) structure, hence the nature of the interface between these materials is important

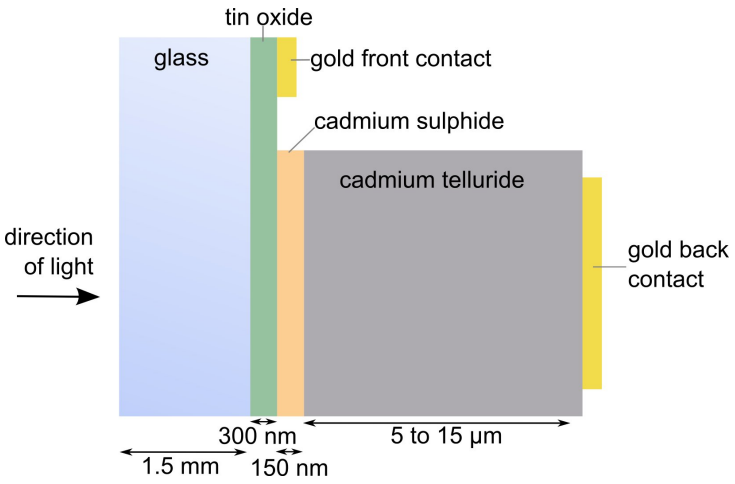

Figure 2-1: Diagram of the device structure focused on during this work.

as it is required to reduce the stress due to the lattice mismatch. The CdTe absorbs the light and so needs to be thick enough to maximise the amount of light absorbed. Any additional thickness of the layer needs to be limited as it increases the series resistance of the device. The back contact is required to form an electrical junction with the p-type material with as low a resistance as possible.

2.3 Deposition techniques

The properties of a deposited film can be affected by: the growth rates of the depositions, the temperatures at which the layer is formed and the types of precursors involved. Both CdS and CdTe can be successfully deposited by a range of deposition techniques and some examples are presented in this section.

Chemical bath deposition of CdS is a low temperature process at approximately 85 ℃ with a deposition rate of 0.003 µm/min [2]. One of the advantages of the chemical bath deposition process is the uniformity of the layer, which produces good coverage of the substrate [3]. More details of the chemical bath deposition can be found in section 4.1. Two examples of other techniques that have been used to deposit CdS are: spray pyrolysis where the substrate is heated to approximately 400 ℃ [4, 5], and sputtering coating, this involves the substrate reaching approximately 200 ℃, with a deposition rate of 0.02 µm/min [6].

CdTe has been deposited by close space sublimation which is a higher temperature technique with the substrate heated to approximately 500 ℃ and has a fast growth rate in

the order of magnitude of 1 μm/min [6], which is attractive for the commercial production of devices. Further information on close space sublimation can be found in section 5.2.

Other deposition techniques which have been used for CdTe include, metal organic chemical vapour deposition where the substrate has been held at 340 ℃ achieving a growth rate of 0.06 μm/min [7]. Electrodeposition of CdTe can occur at 90 ℃, with a deposition rate 0.02 μm/min and a grain size of 0.75 μm [8].

2.4 Structural properties

CdS can exist as both a wurtzite (hexagonal) or zincblende (cubic) phase [9]. As-deposited CdS has been reported sometimes as a polytype material with both structures present in the same material [10, 11]. Annealed CdS has been widely reported to form wurtzite structure [12, 13].

The zincblende structure of CdTe [14] is regularly reported with a (111) preferred orientation for the as-deposited thin film material [15]. Although the magnitude of the preferred orientation varies for different techniques and different deposition parameters, work by Moutinho *et al.* found CdTe deposited by physical vapour deposition could produce material which was completely aligned along the (111) direction whereas their material deposited by CSS had more randomly orientated grains [16].

There is disagreement over the trend of the preferred orientation with varying CSS deposition parameters. Alamri reported a reduction in the (111) preferred orientation with increasing substrate temperatures (335 to 530 ℃) [17]. While Ferekides *et al.* found CdTe deposited at higher substrate temperatures (600 ℃) has more (111) preferred orientation compared to a random orientation for those deposited at a lower substrate temperature (500 ℃) [18]. This apparent disparity on the affect of the deposition parameters on the amount of (111) preferred orientation may be linked with the decrease in the growth rate reported by Alamri for temperature increasing above approximately 500 ℃. However this would disagree with work by Qi *et al.* who reported preferred orientation occurs when grain growth rates are reduced [15].

Work by Woods *et al.* measured the lattice parameters for CdS and CdTe pellets which had been allowed to reach structural equilibrium at 1000 ℃, for wurtzite CdS a = 0.41361 ± 0.00003 nm and c = 0.67140 ± 0.00012 nm, and for zincblende CdTe

a = 0.64863 ± 0.00002 nm [19].

2.5 Electrical properties

Band structure calculations for the intrinsic dopants in CdTe showed Cd vacancies create shallow acceptor energy levels, while Cd substitution for Te produce intrinsic donor levels [20]. Extrinsic dopants Na, Au, Cu and Ag can be substituted for Cd to form shallow acceptor levels, whereas In, Ga, Al, substituting for Cd or Cu substituting for Te form donor levels. Interstitial Cu and Na atoms (additional atoms between the structural atoms) can also form shallow donor levels [20].

For an annealing process in air the formation of CdO is more energetically favourable than forming TeO_2, so the process can cause Cd vacancies to form [21]. The effect of included oxygen on the electrical properties of CdTe deposited by close space sublimation is not clear, but it has been reported not to increase the density of acceptors within the material [22].

A layer of CdS formed with 0.1 mole percent of Te added to the fabrication precursors was found to have a photoconductivity an order of magnitude lower than for pure CdS, which was attributed to the Te forming recombination or trap sites [23]. A reduction in the initial carrier lifetime was also observed with a change from 0.29 µs for pure CdS to 0.13 µs for CdS with Te.

2.6 Annealing and interdiffusion

Annealing the CdTe CdS structure has been reported as a crucial step to achieving high efficiency devices [24]. A $CdCl_2$ anneal typically involves depositing a layer of $CdCl_2$ onto the sample surface or exposing the sample to a solution containing $CdCl_2$, before heating the sample. The temperature and time of the heating process varies between different research groups with temperatures typically in the range 350 to 450 ℃ and the optimal heating time being 10 to 30 min [25, 26].

The $CdCl_2$ annealing process has been suggested to cause passivation of certain defects and grain boundaries within CdTe. For example, $CdCl_2$ treatment has been linked with a reduction in interface states which decreases the leakage current, but the treatment also

created traps associated with cadmium vacancies which reduce the open circuit voltage [27]. Also Cl donor states have been detected at the back surface of the CdTe, and Cd interstitial sites were detected in the CdS region [28].

Grain growth of the CdTe has been observed during the $CdCl_2$ annealing process [24]. A recrystallisation process is believed to occur as a means of reducing the lattice strain energy within the material through the nucleation and growth of new grains [16, 29]. The new grains which form during recrystallisation have been reported to be randomly orientated and so a change in the preferred orientation of CdTe before and after an annealing has been assigned to evidence of a recrystallisation process [16, 30, 31]. Although a change in the preferred orientation from an alignment along the (111) direction to the (422) direction as a result of a $CdCl_2$ annealing process has also been reported [24]. A recovery process or partial recrystallisation has also been reported to occur during an annealing process [16]. During a recovery process grains can grow at the expense of their neighbours and defect concentrations within the grains are reduced, while in partial recrystallisation new grains start to form in the grain boundaries between the existing grains.

A lack of grain growth in large grain CdTe deposited by CSS has been reported. The annealing process causes an increase in the grain size distribution of the material to an equilibrium limit, for a given temperature and in the presence of a flux ($CdCl_2$) [32]. It has been proposed that the grain distribution of CSS CdTe is already stable for the temperatures involved in the annealing process, although smaller grains near the CdTe/CdS interface region may undergo recrystallisation.

Observations of the interdiffusion between the CdTe and CdS layers have been made with many techniques including XRD and photoluminescence measurements [28, 29]. The diffusion coefficients of sulphur atoms in polycrystalline CdTe were found in work by Lane *et al.* [33]. The results show that two different speeds of diffusion occur, with the diffusion along the grain boundaries being quicker than the process through the bulk of the grains. A comparison between diffusion coefficients for the material with and without the presence of $CdCl_2$, showed that the diffusion is faster in the presence of $CdCl_2$. It has also been demonstrated that diffusion along grain boundaries may be partially limited by the diffusion of the S within the CdS layer [34].

Work by Roger *et al.* found that the sulphur diffusion could be limited by the mi-

crostructure within the CdTe [29]. They proposed that by controlling the parameters of the CdTe deposition it may be possible to achieve control over the amount of interdiffusion and sulphur diffusion which occurs within a device.

The properties of CdS_xTe_{1-x} alloy have been studied, with a phase diagram of the alloy being reported in work by Lane *et al.* [35]. Samples prepared at 700 ℃ were found to have a zincblende structure for $x \leq 0.2$ and a wurtzite structure was observed for samples with $x \geq 0.9$. A mixed phase of wurtzite and zincblende structure was observed for the values of x in between. An 11 % lattice mismatch exists between the CdS and CdTe [36]. The formation of the CdS_xTe_{1-x} alloy may help to relieve strain caused by the lattice mismatch in the CdTe CdS structure at the interface between the materials [33]. The lattice parameters of the alloy has been shown to vary linearly in each phase of the alloy according to Vergard's law, and coefficients for each phase have been presented [19]. The variation in the band gap of the CdS_xTe_{1-x} alloy can be described by the expression [37]

$$E_g(x) = E_0 + (E_1 - E_0 - b)x + bx^2 \tag{2-1}$$

Where E_0 is the band gap at $x = 0$ (i.e. CdTe), E_1 is the band gap at $x = 1$ (i.e. CdS) and b is the bowing parameter. For samples deposited by a physical vapour deposition the parameters for the expression were found to be $E_0 = 1.54 \pm 0.01$ eV, $E_1 = 2.36 \pm 0.02$ eV and $b = 1.88 \pm 0.07$ eV. The optical constant of CdS_xTe_{1-x} alloy have been presented by Wood *et al.* and Wei *et al.* [38, 39].

2.7 Defects and grain boundaries

Twinning defects are where a change in the crystallographic structure occurs, due to a change in the stacking sequence of the atoms or a rotation of the structure by a specific amount around a crystallographic direction [25, 40]. Work by Terheggen *et al.* showed CdTe deposited by close space sublimation had a higher ratio of grain volume to defect density than CdTe deposited by high vacuum evaporation [25]. A high density of twin boundaries can be a driving force for recrystallisation during an annealing process, although the density can be reduced through a recovery process [41].

Grain boundaries are sites of carrier recombination, which can be passivated by changing the properties of the grains and reducing the boundaries resistivity [42]. Work by Woods and Robinson proposed a model for the thermally assisted tunnelling transport

across the grain boundaries [43]. Their work compared the model to data and concluded a $CdCl_2$ treatment increased the barrier height at the grain boundary, which reduced the recombination of the carriers at the interface.

2.8 Electrical contacts

CdTe has a high work function (5.8 eV) and this prevents CdTe from forming an ohmic contact with the majority of metals [44]. The work function of a material is the minimum energy required to remove an electron from that material. For a p-type semiconductor if the work function of the metal is less than the work function of the semiconductor a rectifying contact occurs [45]. This is a non-ohmic contact and therefore the current does not vary linearly with the voltage across it. A Schottky barrier forms at the contact, with the barrier height (Φ_b) determined by the expression [46];

$$\Phi_b = E_g/q + \chi - \varphi_m \tag{2-2}$$

This expression assumes the Fermi level is not pinned by interface states and where q is the electronic charge, φ_m is the work function of the metal, E_g is the band gap and χ is the electron affinity of the p-type semiconductor.

The transport of the carriers across the interface can be by a thermonic emission or a tunnelling process. The width of the Schottky barrier can be decreased by increasing the concentration of dopants in the region of the contact, and this increases the probability of tunnelling [47].

There are several different approaches to producing a p^+ region at the back surface of the CdTe, which are reported by other research groups. Creating a Te rich region through chemically etching the surface has been reported to produce the required p^+ region. Two examples of chemical etches which have been used to produce a Te rich layer are: a bromine:methanol [48, 49] or nitric acid/phosphoric acid etch [50, 51]. Further doping of the back surface region has been achieved by diffusing dopants into the CdTe. Compounds which include copper have been used to dope the back surface of the CdTe in efficient devices, in particular copper graphite [52] and copper mercury telluride [53, 54]. However copper has been reported to diffuse into the CdTe/CdS interface at elevated temperatures, and this degrades the electrical properties of the device [55]. Non-copper contacts have

been developed to try and improve the stability of the devices. An example of a non-copper back contact is a molybdenum antimony tellurium alloy [44]. Gold or graphite paste are examples of materials which can be used as the lateral contact material [56].

The transparent conducting oxide front contact is regularly a tin oxide base material. However indium tin oxide has been reported to be unsuitable for CdTe/CdS solar cell deposited at high temperature due to the indium diffusing through the CdS and causing unwanted doping of the CdTe [1, 14]. Alternative materials such as cadmium stanate are also used [57].

2.9 Best efficiency

The most recent improvement in the maximum efficiency achieved for CdTe based solar cells was in 2001 by Wu *et al.* [54]. The device included a customised front contact which had a low resistance and high optical transmission. A zinc stannate (Zn_2SnO_4) buffer layer was also incorporated between the front contact and CdS layer, which was reported to reduce the shunt resistance and allowed a thinner CdS layer to be used, which reduced losses due to CdS absorption. The CdS layer was deposited by a chemical bath deposition and the CdTe layer was deposited by close space sublimation. The best efficiency reported was 16.5 % (16.7 % [58][1]). The parameters of this cell shows the present limits for producing the maximum power: a short circuit density of 26 mA/cm^2, a open circuit voltage of 845 mV and a fill factor of 76 %.

[1]The efficiency has since been revised due to a change in the standardised solar spectrum.

References

[1] D. Bonnet, Thin Solid Films **361**, 547 (2000).

[2] I. O. Oladeji, L. Chow, J. R. Liu, W. K. Chu, A. N. P. Bustamante, C. Fredricksen, and A. F. Schulte, Thin Solid Films **359**, 154 (2000).

[3] A. I. Oliva, R. Castro-Rodriguez, O. Ceh, P. Bartolo-Perez, F. Caballero-Briones, and V. Sosa, Applied Surface Science **148**, 42 (1999).

[4] J. Touskova, D. Kindl, and J. Kovanda, Thin Solid Films **214**, 92 (1992).

[5] R. K. Sharma, K. Jain, and A. C. Rastogi, Current Applied Physics **3**, 199 (2003).

[6] N. Romeo, A. Bosio, R. Tedeschi, A. Romeo, and V. Canevari, Solar Energy Materials and Solar Cells **58**, 209 (1999).

[7] R. A. Berrigan, N. Maung, S. J. C. Irvine, D. J. Cole-Hamilton, and D. Ellis, Journal of Crystal Growth **195**, 718 (1998).

[8] B. Basol, in *21st IEEE Photovoltaic Specialists Conference* (1990), p. 588.

[9] H. Metin and R. Esen, Semiconductor Science and Technology **18**, 647 (2003).

[10] P. N. Gibson, M. E. Ozsan, D. Lincot, P. Cowache, and D. Summa, Thin Solid Films **361**, 34 (2000).

[11] U. Ketipearachchi, D. Lane, K. Roger, J. Painter, and M. Cousins, in *Materials Research Society Fall Meeting* (2004).

[12] R. Jayakrishnan, S. Kumar, and R. Pandey, Semiconductor Science and Technology **9**, 97 (1994).

[13] Y. H. Lee, W. J. Lee, Y. S. Kwon, G. Y. Yeom, and J. K. Yoon, Thin Solid Films **341**, 172 (1999).

[14] R. W. Birkmire and E. Eser, Annual Review of Materials Science **27**, 625 (1997).

[15] B. Qi, D. Kim, D. L. Williamson, and J. U. Trefny, Journal of the Electrochemical Society **143**, 517 (1996).

[16] H. R. Moutinho, M. M. Al-Jassim, D. H. Levi, P. C. Dippo, and L. L. Kazmerski, Journal Of Vacuum Science & Technology A **16**, 1251 (1998).

[17] S. N. Alamri, Physica Status Solidi A-Applied Research **200**, 352 (2003).

[18] C. S. Ferekides, D. Marinskiy, V. Viswanathan, B. Tetali, V. Palekis, P. Selvaraj, and D. L. Morel, Thin Solid Films **361**, 520 (2000).

[19] D. A. Wood, K. D. Rogers, D. W. Lane, G. J. Conibeer, and D. Parton, Journal of materials science letters **17**, 1511 (1998).

[20] S. H. Wei and S. B. Zhang, in *Naitional Centre Photovoltaic program review meeting* (2001).

[21] Y. Marfaing, Thin Solid Films **387**, 123 (2001).

[22] D. Rose, D. Levi, R. Matson, D. Albin, R. Dhere, and P. Sheldon, in *25th IEEE Photovoltaic Specialists Conference* (1996), p. 777.

[23] R. K. Ahrenkiel, D. H. Levi, S. Johnston, W. Song, D. Mao, and A. Fischer, in *26th IEEE Photovoltaic Specialists Conference* (1991), p. 535.

[24] A. Romeo, D. L. Batzner, H. Zogg, and A. N. Tiwari, Thin Solid Films **361**, 420 (2000).

[25] M. Terheggen, H. Heinrich, G. Kostorz, A. Romeo, D. Baetzner, A. N. Tiwari, A. Bosio, and N. Romeo, Thin Sold Films **431**, 262 (2003).

[26] M. D. G. Potter, D. P. Halliday, M. Cousins, and K. Durose, Thin Solid Films **361**, 248 (2000).

[27] S. A. Ringel, A. W. Smith, M. H. MacDougal, and A. Rohatgi, Journal of Applied Physics **70 (2)**, 881 (1991).

[28] M. D. G. Potter, M. Cousins, K. Durose, and D. P. Halliday, Journal of Materials Science-Materials in Electronics **11**, 525 (2000).

[29] K. D. Rogers, J. D. Painter, M. J. Healy, D. W. Lane, and M. E. Ozsan, Thin Solid Films

339, 299 (1999).
[30] G. Zoppi, K. Durose, S. J. C. Irvine, and V. Barrioz, Semiconductor Science and Technology **21**, 763 (2006).
[31] K. D. Rogers, D. A. Wood, J. D. Painter, D. W. Lane, and M. E. Ozsan, Thin Solid Films **361**, 234 (2000).
[32] M. A. Cousins and K. Durose, Thin Solid Films **361**, 253 (2000).
[33] D. W. Lane, J. D. Painter, M. A. Cousins, G. J. Conibeer, and K. D. Rogers, Thin Solid Films **431**, 73 (2003).
[34] M. A. Cousins, D. W. Lane, and K. D. Rogers, Thin Solid Films **431-432**, 78 (2003).
[35] D. W. Lane, G. J. Conibeer, D. A. Wood, K. D. Rogers, P. Capper, S. Romani, and S. Hearne, Journal of Crystal Growth **197**, 743 (1999).
[36] K. Ohata, J. Saraie, and T. Tanaka, Japanese Journal of Applied Physics **12**, 1198 (1973).
[37] D. W. Lane, Solar Energy Materials and Solar Cells **90**, 1169 (2006).
[38] D. A. Wood, K. D. Rogers, D. W. Lane, and J. A. Coath, Journal of Physics-Condensed Matter **12**, 4433 (2000).
[39] K. Wei, F. H. Pollak, J. L. Freeouf, D. Shvydka, and A. D. Compaan, Journal of Applied Physics **85**, 7418 (1999).
[40] K. Durose and G. J. Russell, Journal of Crystal Growth **101**, 246 (1990).
[41] M. Terheggen, H. Heinrich, G. Kostorz, D. Baetzner, A. Romeo, and A. N. Tiwari, Interface Science **12**, 259 (2004).
[42] T. P. Thorpe, A. L. Fahrenbruch, and R. H. Bube, Journal of Applied Physics **60**, 3622 (1986).
[43] L. Woods, G. Robinson, and D. Levi, in *28th IEEE Photovoltaic Specialists Conference* (2000), p. 603.
[44] A. E. Abken and O. J. Bartelt, Thin Solid Films **403**, 216 (2002).
[45] S. Fonash, *Solar cell device physics* (Academic Press, 1981).
[46] S. H. Demtsu and J. R. Sites, Thin Solid Films **510**, 320 (2006).
[47] R. H. Bube, *Photoelectronic properties of semiconductors* (Cambridge University Press, 1992).
[48] B. McCandless and R. Birkmire, Solar Cells **31**, 527 (1991).
[49] M. Emziane, K. Durose, D. P. Halliday, A. Bosio, and N. Romeo, Applied Physics Letters **87**, 261901 (2005).
[50] H. R. Moutinho, R. G. Dhere, C. S. Jiang, M. M. Al-Jassim, and L. L. Kazmerski, Thin Solid Films **514**, 150 (2006).
[51] K. Mitchell, C. Eberspacher, F. Cohen, J. Avery, G. Duran, and W. Bottenberg, Solar Cells **23**, 49 (1988).
[52] T. Okamoto, Y. Harada, A. Yamada, and M. Konagai, Solar Energy Materials and Solar Cells **67**, 187 (2001).
[53] D. H. Rose, F. S. Hasoon, R. G. Dhere, D. S. Albin, R. M. Ribelin, X. S. Li, Y. Mahathongdy, T. A. Gessert, and P. Sheldon, Progress in Photovoltaics **7**, 331 (1999).
[54] X. Wu, J. C. Keane, R. G. Dhere, C. DeHart, D. S. Albin, A. Duda, T. A. Gessert, S. Asher, D. H. Levi, and P. Sheldon, in *17th European Photovoltaic Solar Energy Conference* (2001).
[55] K. D. Dobson, I. Visoly-Fisher, G. Hodes, and D. Cahen, Solar Energy Materials and Solar Cells **62**, 295 (2000).
[56] A. Niemegeers and M. Burgelman, Journal of Applied Physics **81**, 2881 (1997).
[57] D. Levi, W. Xuanzhi, A. Swartzlander-Guest, F. Hasoon, and R. Matson, Photovoltaic Specialists Conference, 2000. Conference Record of the Twenty-Eighth IEEE **28**, 525 (2000).
[58] M. A. Green, K. Emery, Y. Hishikawa, and W. Warta, Progress in Photovoltaics **17**, 85 (2009).

Chapter 3

Procedures and characterisation techniques

3.1 Introduction

A description of some of the processes used to fabricate the samples in this work is given in sections 3.2 to 3.5 of this chapter. The deposition procedures for the CdS and CdTe layers are discussed in detail in the next two chapters, respectively. The techniques used to analyse the samples in this work are discussed in section 3.6 to 3.13.

3.2 $CdCl_2$ and air annealing

A saturated solution of $CdCl_2$ dissolved in methanol was used for $CdCl_2$ anneals. The samples were placed within this solution for 2 min, after which they were rinsed with methanol and blown dry with nitrogen gas. The samples were then loaded onto a glass mount in the end of a tube furnace, four samples could be annealed at the same time. The tube furnace was then set to heat up to 450 ℃, the actual temperature measured within the furnace was found to be 420 ℃. After the furnace had reached temperature the samples were then moved into the central hot region of the furnace for 20 min. This was similar to $CdCl_2$ annealing procedures reported in the literature [1, 2]. The furnace was then switched off and the samples were moved back to the end of the furnace, where they were allowed to cool. This procedure was carried out in air.

The procedure above was also done without the samples being submerged in a satu-

rated methanol:$CdCl_2$ solution. This was referred to as an air anneal where the samples were just heated in the furnace for 20 min.

3.3 Bromine:methanol etch

To prepare the back surface of the CdTe before the gold contacts were evaporated onto the surface, a solution consisting of 25 ml methanol and 0.05 ml bromine was used to etch the back surface. The samples were placed in the solution for 10 sec, then rinsed in methanol and blown dry. Similar preparation techniques were reported in the literature [3, 4].

When trying to remove some of the CdTe layer by an etching process a more concentrated bromine:methanol solution was used. The solution consisted of 25 ml methanol and 0.1 ml bromine. The samples were submerged in this solution for up to 4 min. Then they were removed from the solution, rinsed in methanol and blown dry.

3.4 Gold evaporation

The back contacts for the cells fabricated in this work were gold layers deposited by evaporation. The samples were placed on metal masks with six 5 mm diameter round holes in them. These masks were mounted above a source crucible in a bell jar evaporator. The samples were approximately 230 mm from an aluminium oxide coated boat where the source material was placed, 99.999% metal basis gold. The chamber was pumped down to a vacuum of approximately 1.5×10^{-5} mbar, using a rotatory and a diffusion pump. The boat was heated by electrical resistive heating. The current to the crucible was slowly turned up to 65 % (of an arbitrary normalise maximum) over 6 min, it was then left there for 10 min before the current was turned down. Four samples could undergo deposition at the same time, with approximately 0.1 g of gold being used for each deposition. The gold layers deposited were approximately 60 nm thick.

3.5 Sample preparation for electrical measurements

The front contact, the TCO layer, is covered during the deposition of the later layers (CdS and CdTe). A region of the TCO had to be made accessible for the electrical measurements. In order to remove the CdTe and CdS without damaging the TCO two

chemical solutions were used. A solution of hydrogen peroxide saturated with citric acid efficiently dissolves the CdTe. While hydrochloric acid is used to remove the CdS layer. The CdS on the glass side of the sample was also removed with hydrochloric acid.

3.6 X-ray diffraction (XRD)

X-ray diffraction (XRD) measurements give information about the crystallographic structure within a material [5]. The peaks on a diffractogram are the result of constructive interference from the X-rays scattered off consecutive layers of ordered atoms within the material. This is governed by Bragg's law:

$$\lambda = 2dsin(\theta) \tag{3-1}$$

Where λ is the wavelength of the X-rays, d is the spacing between the layers of atoms and θ is half the angle between the transmitted beam and the diffracted beam.

The X-rays used in this work were produced from a copper target, where the $K_{\alpha 1}$ and $K_{\alpha 2}$ characteristic lines of copper were the intense lines within the X-ray source beam. The $K_{\alpha 1}$ and $K_{\alpha 2}$ lines cause the reflections produced by the samples to be doublets, with the more intense lower angle peak due to the $K_{\alpha 1}$ line and the less intense higher angle peak was due to the $K_{\alpha 2}$ line. Measurements were either made with a 0.02° 2θ angular resolution where the detector stopped at each incremental position, or a 0.005° 2θ angular resolution was used with a continuous measurement technique where the detector was moved continuously. The higher resolution technique was only used to measure the regions around the diffraction reflections.

The X-ray measurements in this work used a reflection powder diffraction technique with Bragg Brentano optics. This powder technique gains information about the sample in the illuminated volume assuming the 'particles' within the powder are randomly arranged, and small enough that a large number of particles are interrogated, so all possible orientations are inspected. In this work the materials examined are polycrystalline films, not powders, and so any preferred orientation within the film will effect the data. Only the planes of atoms parallel with the surface of the sample will satisfy Bragg's law due to the geometry of the experiment. The reflections for the different orientations therefore are the result of different grains within the material, see figure 3-1. This is an important

consideration when looking at the difference in the properties of each crystallographic orientation.

The preferred orientation of a material is concerned with how the relative intensity of the different crystallographic directions compares with the intensities of a randomly powdered material. The information for reference materials came from the International Centre for Diffraction Data (ICDD) PDF-2 powder diffraction file (release 2004). In this work the expressions used to quantify the amount of preferred orientation are, [6–8].

$$C_{hkl} = \frac{\frac{I_{hkl}}{I_{ref,hkl}}}{\frac{1}{n}\sum_{n}\frac{I_{hkl}}{I_{ref,hkl}}} \tag{3-2}$$

$$\sigma = \sqrt{\sum \frac{1}{n}(C_{hkl}-1)^2} \tag{3-3}$$

Where the I_{hkl} refers to the intensity of the hkl peak, $I_{ref,hkl}$ is the intensity of the hkl peak in a reference CdTe material (here CdTe material with card reference 65-440 from ICDD), n is the number of reflections, C_{hkl} is the texture coefficient of each peak and σ is reported in other work as the preferred orientation. In this work σ is referred to as the texture coefficient.

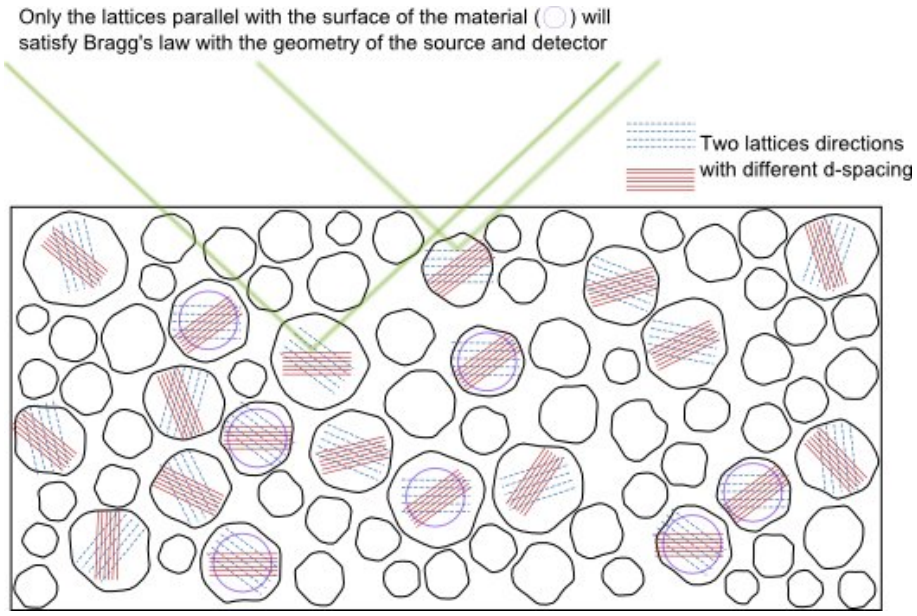

Figure 3-1: The diagram illustrates diffraction for the different orientations will result from the plains in different grains. This diagram applies to the sample with rotational symmetry around the axis normal to the sample surface.

The lattice parameters of the materials in this work were calculated from a set of reflections by extrapolating a linear fit to the Taylor Nelson function (F_{TN}) to find the intercept [9, 10].

$$F_{TN} = \frac{cos^2\theta}{sin\theta} + \frac{cos^2\theta}{\theta} \tag{3-4}$$

The larger the gradient of the linear fit the greater the systematic error in the data, while the scale of the scatter within the data indicates the size of the random error. This method has been applied to CdTe by Mountinho *et al.* and Romeo *et al.* [6, 11]. An example of a Taylor Nelson plot can be seen in figure 5-13.

In this work the term 'coherence length' will be defined as the average dimension of a structurally ordered domain. The 'crystallite size' is a region of the material where the planes have the same orientation. A 'grain' here refers to a bound particle observed by microscopy techniques. The implication is that the coherence length size, as determined by XRD, can be smaller than the grain size measured by other techniques looking at the volume defined by grain boundaries.

The width of the XRD reflection is the result of a combination of the resolution of the equipment, the finite crystallite size and any local non uniform strain. Uniform strain within the material can affect the peak position by changing the space between the layers of the atoms (d spacing) by a constant amount, see figure 3-2. Increased broadening of the reflection due to the size of the coherence length becomes a measurable effect if the coherence length is smaller then approximately 0.1 μm [5].

A Williamson Hall plot allows the broadening of the XRD reflections due to the finite crystallite size and non-uniform strain within the material to be assessed. A standard with a large coherence length can be used to calculate the broadening which results from the measurement technique. In this work silicon powder (640C NIST) reference material was used to determine instrumental effects. This instrument correction (g) was calculated using a function defined by Langford [12]. The integral breadth (β = area/intensity) of each reflection was corrected to remove the broadening caused by the instrument. A function of the integral breadth β_f could then be calculated using equation 3-5. For a Williamson Hall plot a function on the integral breadth is plotted against the d^{-1}, see equation 3-6. An example of a plot can be seen in figure 5-14. For a Williamson Hall plot if the integral breadth function is found not to vary with inverse d spacing it would

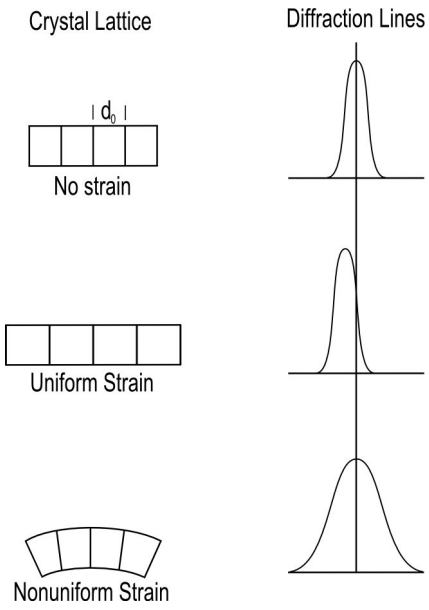

Figure 3-2: The figure illustrates the effect of strain within the crystal lattice on the resulting diffraction reflection [5].

indicate the broadening was due to the crystallite size alone.

$$\beta_f = (\frac{A}{I} - g)\frac{cos\theta}{\lambda} \tag{3-5}$$

$$d^{-1} = \frac{2sin\theta}{\lambda} \tag{3-6}$$

Where A is the net integrated area of the reflection, I is the intensity of the reflection and d is the d-spacing.

If it is assumed that the width of a reflection is solely due to the size of the coherence length (t), then the Scherrer equation is an expression for estimating the coherence length from the integral breath of the peak, see equation 3-7.

$$t = \frac{0.9\lambda}{\beta cos\theta} \tag{3-7}$$

3.6.1 Two phase analysis

In the literature two phases of material have been identified in CdTe reflections by Moutinho *et al.* [13]. The two phases were only reported for the CdTe material deposited on CdS after annealing, the absence of two phases in the material deposited on ITO allowed them to conclude the extra peaks were caused by the formation of a

CdS_xTe_{1-x} alloy. Two phases of material were also identified in work by Vamsi Krishana and Dutta who used glancing angle X-ray diffraction and demonstrated the variation in the composition of the alloy with depth within a CdTe layer [14].

The XRD analysis measured with the higher angle resolution (0.005°) indicated some of the XRD reflections in this work had an unusual intensity ratio of the $K_{\alpha 1}$ and $K_{\alpha 2}$ components (see figure 3-3). It was also noted that the reflections appeared to have asymmetric high angle tails. To enable the asymmetry of the reflections to be studied more closely a symmetrical peak shape was used to fit the data. A Voigt profile shape function involves a convolution of a Gaussian with a Lorentzian, see equation 3-8 [12]. For the lower resolution data (0.02°) a split pseudo Voigt function was used. This is not necessarily a symmetric function and involves separate parameters being fitted to each side of the reflection. In comparison, the higher resolution reflections were fitted using pseudo Voigt functions where the function is symmetrical. This symmetrical nature of the function would cause large amounts of asymmetry in the reflection to reduce the quality of the fit of the function to the reflection.

$$I(x) = \frac{\beta}{\beta_G} I_0 Re(w(\pi^{\frac{1}{2}} \frac{x}{\beta_G} + i(\frac{\beta_L}{\pi^{\frac{1}{2}}} \beta_G))) \tag{3-8}$$

Where β_L and β_G are the integral breadth of the Lorentzian and Gaussian components and the bracketed term is the real component of the full width half maximum function (=2w).

To attempt to try and fit the XRD reflections with the unusual shape, multiple pseudo Voigt functions were fitted to a single reflection. Fitting with three or more functions at the same time, produced a good fit. However the solution varied depending on the suggested starting positions of the functions. When two profiles were used to fit the data a good agreement between the fit and the data was achieved, see figure 3-4. The solutions were consistent for a range of starting positions, as long as both functions were started with positions near the reflection. From these fits it is deduced in the current work that two phases are present within the material. The measurement technique used in this work introduces some asymmetry into the data. This asymmetry contribution is a function of the angle, it is largest at low angles and is zero at 90° 2θ. The large amount of asymmetry in the first CdTe peak at approximately 26.7° 2θ due to the measurement technique caused this first peak not to be fitted with two phases, since it was not possible

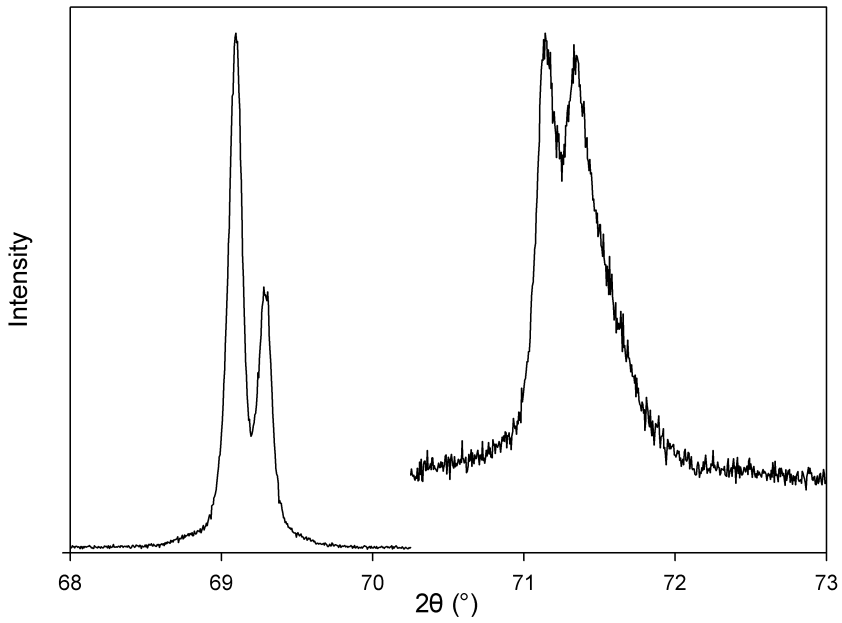

Figure 3-3: Normalised X-ray reflections, the left reflection is for a silicon standard material and the right reflection is for CdTe deposited on a roughened substrate. The figure displays one of the most extreme examples observed in this work of asymmetric tails. Also the $K_{\alpha 1}$ and $K_{\alpha 2}$ component ratio is unusual in the CdTe reflection, the ratio of the two identifiable peaks in each reflection should be very similar. The expected ratio of the two components can be seen in the reflection from the silicon standard material.

to consistently fit two functions to this reflection. The two phases should have the same structure, as no additional reflections were observed and the second peak was present in all of the reflections (except the first (111) reflection).

The parameter R_{wp} is the weighted residual from fitting a peak function to a reflection. As a comparison, fitting the reflection in figure 3-4 with one peak $R_{wp} = 10.22$, fitting with two peaks $R_{wp} = 8.28$ and fitting the reflection with three peaks $R_{wp} = 8.21$. This shows fitting with two peaks decreased the weighted residual by a large amount and an additional peak had a smaller effect. This supports the assumption of two phases being present within this data instead of a larger number of phases. In this work the peak with the largest d-spacing was referred to as the 1^{st} phase.

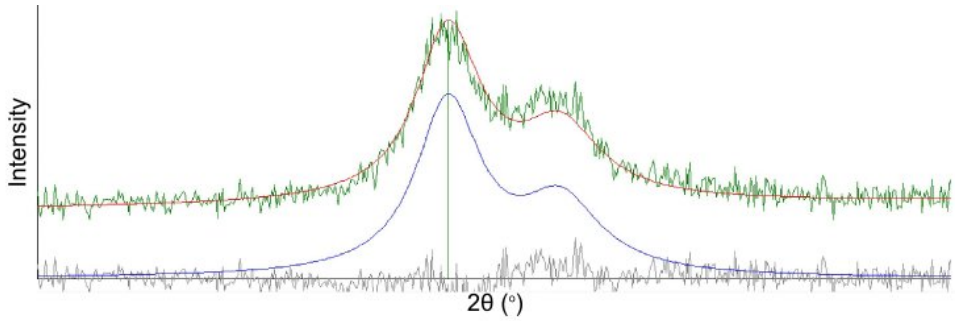

(a)

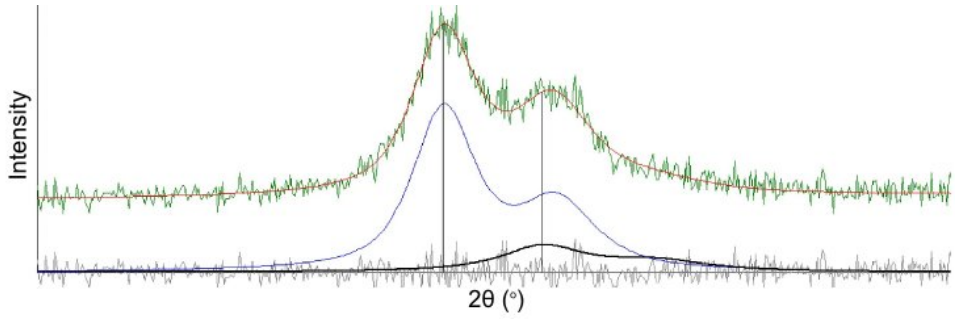

(b)

Figure 3-4: Examples of fitting (a) one pseudo Voigt function or (b) two pseudo Voigt functions to a CdTe reflection at 97.1°. In each image, the raw data is the top noisy line, the middle smooth curves represents the pseudo Voigt functions and the noisy line at the bottom is the residual of the fit. Comparing the two figures, it is possible to see the single Voigt function can not encompass the asymmetry of the reflection.

3.7 Rutherford backscattering spectrometry (RBS)

This technique utilises the interaction of accelerated ions colliding with atoms within the sample to allow information about the composition and structure to be determined. A detector positioned at a known angle to the sample measures the energy of the backscattered ions. Through knowing the energy of the incident beam of ions and the geometry of the experiment, a model can be made to simulate the suggested interaction undergone by the ions in the beam and therefore determine information about the sample.

The energy (E_1) of an ion scatter by a surface atom of the sample can be calculated from the equation 3-9 [15].

$$E_1 = E_0[[\{1 - (\frac{M_1 sin\theta}{M_2})^2\}^{\frac{1}{2}} + (\frac{M_1 cos\theta}{M_2})]^2/(1 + \frac{M_1}{M_2})] \quad (3\text{-}9)$$

Where E_0 is the ions incident energy, M_1 and M_2 are the masses of the ions and the surface atoms of the target material, respectively and θ is the scattering angle. The ratio

of the final energy of the ion over the initial energy of the ion is called the Kinematic factor. The Kinematic factor is only dependent on the masses of the ions and target atoms and the scattering angle.

The relationship between the number of target atoms and the number of detected ions is given by the scattering cross section $\sigma(\theta)$, see equation 3-10 [16]. The number of target atoms per unit area can be calculated using the scattering cross section knowing the geometry of the experiment, the number of incident ions and the number of detected scattered ions.

$$\sigma(\theta) = \left(\frac{Z_1 Z_2 e^2}{4E}\right)^2 \frac{1}{sin^4\theta/2} \tag{3-10}$$

Where Z_1 and Z_2 are the atomic numbers of the ion and the target atoms respectively and E is the incident kinetic energy of the ion. This expression assumes the mass of the ion is much less than the mass of the target ion.

A 2 MeV Van de Graaff accelerator was used for the majority of the RBS in this work, with the exception of the measurements carried out at Surrey ion beam facility on the optical fibres. The accelerator consists of a Van de Graaff generator for creating a large potential along a beam tube (2 m in length). A mixed gas of hydrogen and helium was used as the ion source in this work. The ions are accelerated down the tube by the potential and then deflected by a magnet towards the sample. The potential down the vertical column determines the coarse energy of the beam, while the deflection of the beam by the magnet allows the energy distribution of the accelerated ions to be reduced. The geometry of the experiment was arranged so that the detector was set up to be 15 ° from the sample normal, at an angle of 165 ° backscatter.

The SIMNRA software (Max-Planck-Institut fur Plasmaphysik) enabled a layer model of the sample to be created, where the atomic composition of each layer could be defined. The parameters of the model were adjusted to fit the data. The error in the thickness values were obtained by adjusting the parameters of the model and recording the limits the values could have. This is a very simple estimation of the error in the thickness values and did not include errors from the assumption made in the calculations.

3.8 Scanning electron microscopy (SEM)

The topography of the samples was imaged using either secondary electrons (with an Everhart-Thornley detector) or back scattered electrons (with a Robinson detector) [17]. The electron beam was produced by an electron gun and then focused onto the sample. The majority of the samples examined were not coated with a conducting layer, this allowed them to be examine by other techniques. This lead to some of the samples being analysed with the system in an environmental mode to reduce the affect of surface charging. In this mode a reasonably high vacuum is maintained in the microscope column while a higher pressure exists in the chamber near the sample. These samples analysed in the environmental mode had a reduction in the resolution of the images due to elastic scattering between the electrons and the gas molecules.

Energy dispersive X-ray (EDX) analysis (with a silicon drift detector) was used to measure the composition of the materials. Quantitative analysis of the composition of a sample using EDX is a complex problem when variations between the samples and calibration standard materials are considered. The main correction factors considered in quantitative analysis are: the atomic number of the sample in comparison to a standard, since this is concerned with how efficiently the X-rays are generated; the absorption coefficient, which refers to the reduction in intensity of the X-rays due to absorption within the materials; and the fluorescence factor, which is concerned with higher energy X-rays exciting atoms which emit characteristic radiation [17]. Other factors which require consideration are the interaction volume of the electron beam and the topography of the sample surface, with a flat sample being preferential.

3.9 Alpha step surface profiler

An Alpha step 100 stylus surface profiler (Tencor instruments) was used to make physical thickness and roughness measurements. The equipment is very simple and uses a stylus on a counter levered arm to determine changes in the height of the surface of the sample. The measurements are displayed on paper or on a computer. The equipment is capable of measurements down to a 5 nm resolution.

3.10 4 point probe resistance measurements

Thin film resistance measurements were carried out using a four point probe (A. and M. Fell Ltd.) and a Keithley 2000 multimeter. The technique consist of four equally spaced probes, where a current is passed between the outer two probes and the voltage is measured across the middle two probes. This enables the contact resistance between the probes and the material to be minimised due to the high impedance of the voltage measurement. The sheet resistance (R_s) is given by:

$$R_s = \frac{\rho}{t} = \frac{\pi}{ln2}\frac{V}{I} \tag{3-11}$$

Where ρ is the bulk resistivity and t in the sample thickness.

3.11 Ellipsometry

Ellipsometry is a technique which uses polarised light to investigate optical and structural properties of thin film materials. Polarised light is light with an electric field component with a preferential direction [18]. Ellipsometry measures the change in the polarisation of light reflected off the surface of a sample. The equipment here used a white light source which was passed through a polariser enabling the polarisation state of the light to be known before it was shone onto the sample. A rotating compensator allows the polarisation of the light reflected off the sample to be determined from the intensity of the light measured by a detector.

The parameters used in ellipsometry to describe the ratio of the polarisation states (ρ) are given by:

$$\rho = \frac{r_p}{r_s} = tan(\psi)e^{i\Delta} \tag{3-12}$$

Where r_s and r_p are components of the polarisation perpendicular and parallel to the plane of incidence respectively, Δ is the relative phase of the components and ψ is the relative amplitude of the components. Information about ψ and Δ were collected as a function of wavelength and also at multiple measurement angles, where the angle is defined between the sample normal and the path of the light from the source. A layered model of the sample can then be created with the values of ψ and Δ calculated and compared to the measured values. The properties of the model can be adjusted so that

the calculated values of ψ and Δ match those of the data, and the properties of the model can be inferred to be the same of those of the sample. A mean squared error function was used to compare the ψ and Δ calculated from the model to the measured values from the sample [19].

In this work a J.A. Woollam Co. M2000UI rotating compensator ellipsometer equipped with CompleteEASE software (version 3.81) was used to make the measurements. This is an automated piece of equipment and the version used in this work was capable of taking measurements over the wavelength range 245 to 1690 nm. The majority of the measurements are made in a reflectance mode, however the equipment is capable of making transmission measurements.

When modelling a material it is important to start with as simple a sample as possible and to build up the complexity of the sample as models for each layer are created. The substrate is therefore always the starting point. With TCO covered glass, the TCO can be polished off and just the glass can be examined. For a semiconducting film it is easier to obtain the thickness of the film first and then to determine the optical constants. This is achieved by limiting the measurement wavelength range to the transparent region below the band gap. In this region the film is treated as transparent and a Cauchy function can be fitted to the semiconductor. The thickness values obtained from the Cauchy function can then be used in a new model of the semiconductor, over the whole wavelength range.

The model should be as simple as possible in order to increase the chance of a single solution for the parameters being found. The material optical properties can be either a tabulated set of optical constants or described by a set of mathematical expressions. The mathematical expressions can either be selected and adjusted individually or incorporated into a complex layer model.

In this work a general layer model called B-spline has been used for the initial modelling, this was in order to reduce the chance of omitting small features within the film data due to an over simplistic model. This model allows its optical constants to initially be set to a reference material. The optical constants were then parameterised by series of individual expressions to allow more control over the fitting parameters. There are several different approaches reported in the literature regarding parameterising the optical properties. The sum of a series of Lorentzian or Gaussian expressions can be used to reproduce the optical properties [20], see figure 3-5. This approach can produce a good

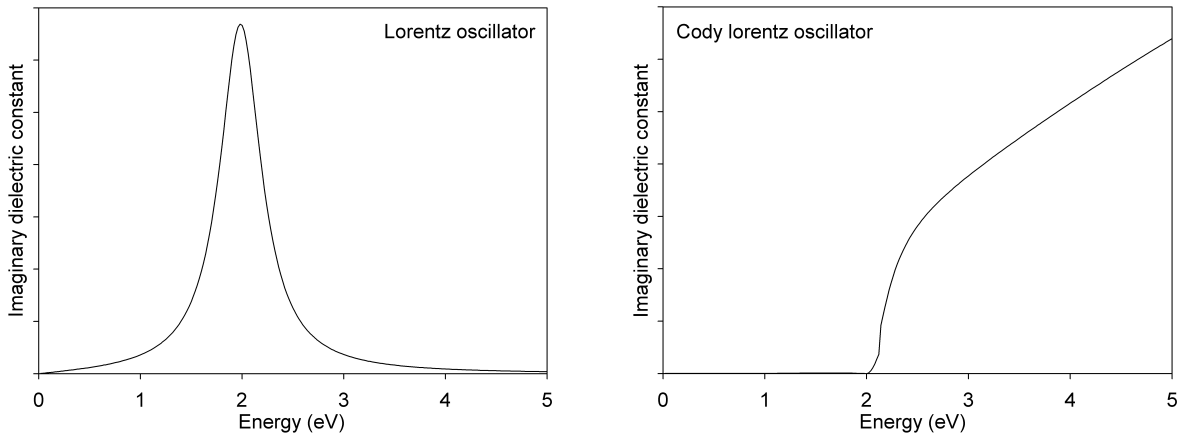

(a) (b)

Figure 3-5: Examples of expressions used in ellipsometry to model the dielectric function of materials. The E_g term in each expression was set equal to 2 eV.

match between the experimental and calculated data, however it can have a large number of fitting parameters. In this work a Cody-Lorentz and a series of Lorentz oscillators were used to parameterise the optical constants [19]. The Cody-Lorentz oscillator was used as it was believed it could describe the properties due to the interband transitions and reduce the total number of oscillators required to describe the parameters [21].

An Effective Medium Approximation layer (EMA) allows two sets of optical constants to be combined. This provides a way of modelling roughness or intermixing between layers. Different expressions for combining the optical constants can be used, here a Bruggeman or linear expression was used [22].

3.12 Current voltage measurements (IV curves)

The current voltage measurements consisted of illuminating the sample solar cells with an AM 1.5G spectrum. The current produced by the device was then monitored as the voltage was varied. In this work a ScienceTech (SS150W) solar simulator was used, with a 150 W xenon arc lamp, see figure 3-6. The system illuminates a uniform area approximately 50 mm in diameter and used a segmented mirror to scramble the beam from the lamp. This allowed a whole sample to be illuminated at once, which meant the sample did not need to be repositioned during the measurements. A Kipp and Zonen (SPlite) pyranometer was used to measure the intensity of the light, with the current

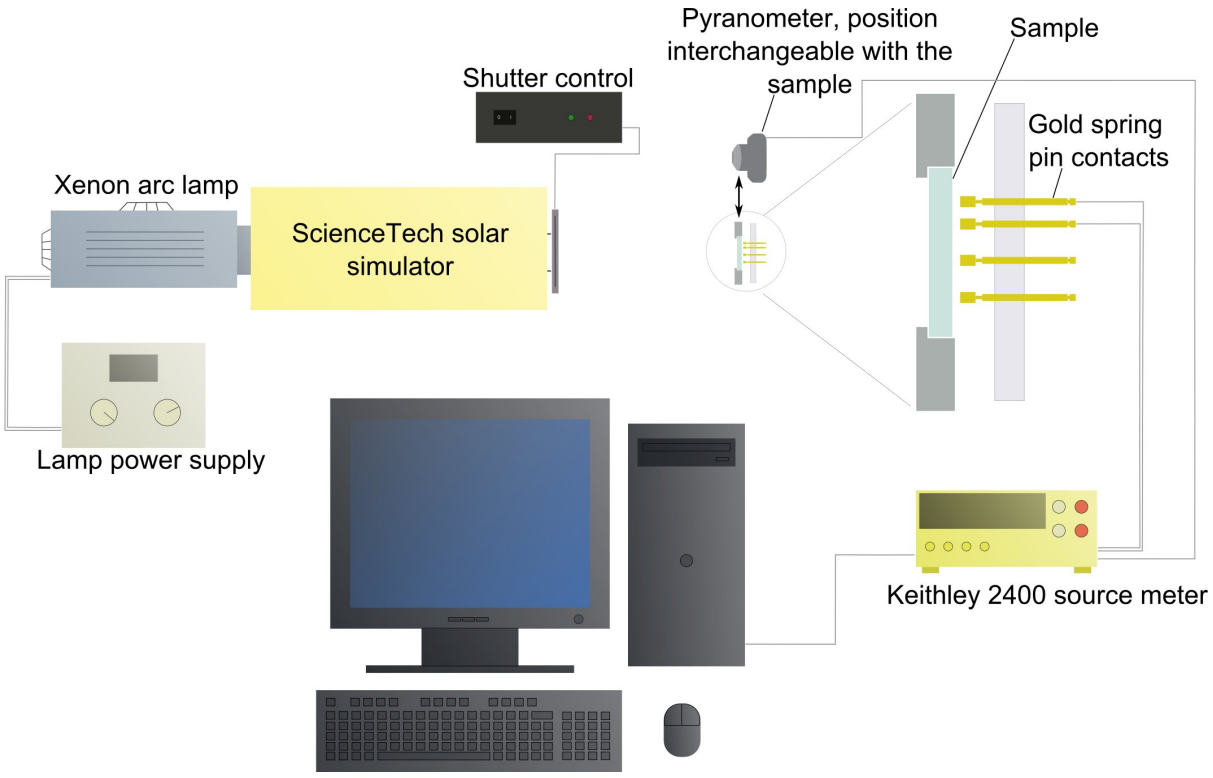

Figure 3-6: A diagram of the IV measurement equipment. Seven gold spring pin contacts held the sample in place, whilst making electrical contact with the six gold discs on the sample, with the seventh pin making contact with the transparent conducting oxide. The wires connected to the source meter could then be connected to different contact pins to measure different cells on the sample.

to the arc lamp being adjusted to achieve the correct intensity. The solar simulator illuminated the sample while a Keithley 2400 source meter varied the voltage applied to the sample and measured the current, controlled by a Visual basic computer program written by Dr Mike Cousins.

The temperature of the cell can increase during a measurement due to the illumination, although the standardised measurement conditions state the cell should be held at 25 ℃. The room in which the equipment was located in was air conditioned, and this indirectly kept the cell at close (± 5 ℃) to the desired temperature.

In this study a two diode solar cell model created by the Energy research Centre of the Netherlands (ECN) was use to fit the IV data [23]. The two diode model was used in this work because of the good fit between the model and the data for the cells in this work with the higher efficiencies. The ECN software initially fits polynomials to the IV curves to determine the open circuit voltage (Voc), short circuit current density (Jsc), fill factor (ff) and the maximum power point. From this the efficiency of the device can be

calculated. The software also fits an expression with two diodes (equation 1-2) allowing information about resistances and current recombination to be determined.

The area of the solar cell fabricated during this investigation was assumed to be the area of the back contact. This is known to be an approximation since carriers generated within a diffusion length of the contact can contribute to the current. The diffusion length of the minority carrier within the grains in thin film CdTe is between 1 to 5 µm [24]. Therefore the current density measured in this work is a slight overestimation of the actual value by approximately 4 % or less. This has repercussions on the other parameters subsequently calculated.

3.13 Spectral response

The spectral response (external quantum efficiency) measurements, measured the current produced by the cell when it was illuminated by monochromatic light of different wavelengths. An Oriel lamp housing with a xenon arc lamp and an Oriel monochromator were used to make the measurements, see figure 3-7. The equipment was surrounded by a black out box and the main lights of the room were turned off during the measurements to try and exclude external light sources. The current produced by the cell was maximised to align the cell with the monochromatic light beam. This technique used a reference cell which here was a GaAs cell, with an efficiency of 19.3 %, which was tested at Newcastle photovoltaic cell test facility. The reference cell's response was measured using the experimental setup and the results were corrected using the reference data from Newcastle in order to determine a calibration function. Measurements of the samples cells were then made using the calibration function. This technique allowed the sample cells to be compared to each other.

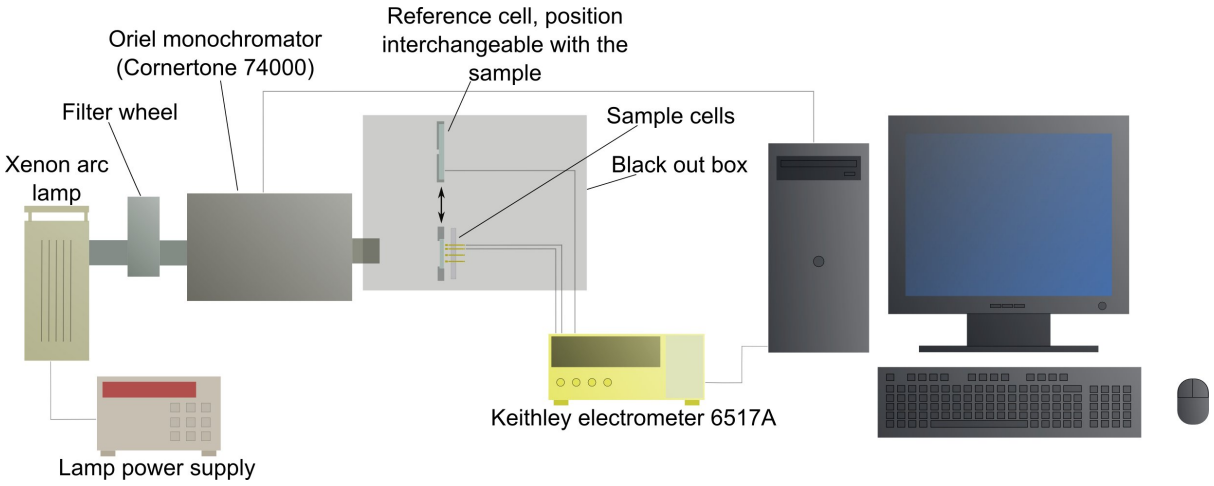

Figure 3-7: The spectral response experimental set up.

References

[1] M. A. Cousins and K. Durose, Thin Solid Films **361**, 253 (2000).

[2] T. Okamoto, Y. Harada, A. Yamada, and M. Konagai, Solar Energy Materials and Solar Cells **67**, 187 (2001).

[3] B. McCandless and R. Birkmire, Solar Cells **31**, 527 (1991).

[4] H. R. Moutinho, R. G. Dhere, C. S. Jiang, M. M. Al-Jassim, and L. L. Kazmerski, Thin Solid Films **514**, 150 (2006).

[5] B. Cullity, *Element of x-ray diffraction* (Addison-Wesley Publishing Company, Inc., 1978), 2nd ed.

[6] H. R. Moutinho, M. M. Al-Jassim, D. H. Levi, P. C. Dippo, and L. L. Kazmerski, Journal Of Vacuum Science & Technology A **16**, 1251 (1998).

[7] G. Zoppi, K. Durose, S. J. C. Irvine, and V. Barrioz, Semiconductor Science and Technology **21**, 763 (2006).

[8] K. H. Kim and J. S. Chun, Thin Solid Films **141**, 287 (1986).

[9] A. Taylor and H. Sinclair, Proceedings of the Physical Society **57**, 126 (1945).

[10] J. Nelson and D. Riley, Proceedings of the Physical Society **57**, 160 (1945).

[11] A. Romeo, D. L. Batzner, H. Zogg, and A. N. Tiwari, Thin Solid Films **361**, 420 (2000).

[12] J. Langford, in *Accuracy in Powder Diffraction II* (1992), p. 110.

[13] H. Moutinho, M. Al-Jassim, F. Abufoltuh, D. Levi, P. Dippo, R. Dhere, and L. Kazmerski, in *26th IEEE Photovaltaic Specialists Conference* (1997).

[14] K. V. Krishna and V. Dutta, Thin Solid Films **450**, 255 (2004).

[15] P. E. J. Flewitt and R. K. Wild, *Physical method for materials characterisation* (Institute of Physics Publishing, Bristol and Philodelphia, 2003), 2nd ed.

[16] L. C. Feldman and J. W. Mayer, *Fundamental of surface and thin film analysis* (North-Holland pulbishing company, 1986).

[17] P. J. Goodhew, J. Humphreys, and R. Beanland, *Electron microscopy and analysis* (Taylor & Francis, 2001), 3rd ed.

[18] H. G. Tompkins and E. A. Irene, *Handbook of Ellipsometery* (William Andrew Publishing/Noyes, 2005).

[19] J. Orava, T. Wagner, J. Sik, J. Prikryl, M. Frumar, and L. Benes, Journal of Applied Physics **104**, 043523 (2008).

[20] S. Adachi, T. Kimura, and N. Suzuki, Journal Of Applied Physics **74**, 3435 (1993).

[21] J. Price, P. Y. Hung, T. Rhoad, B. Foran, and A. C. Diebold, Applied Physics Letters **85**, 1701 (2004).

[22] L. Yan, J. A. Woollam, and E. Franke, Journal of Vacuum Science and Technology. A. Vacuum, Surfaces, and Films **20**, 693 (2002).

[23] A. R. Burgers, J. A. Eikelboom, A. Schonecker, and W. C. Sinke, in *25th IEEE Photovoltaic Specialists Conference* (1996).

[24] A. Morales-Acevedo, Solar Energy Materials & Solar Cells **90**, 678 (2006).

Chapter 4

Chemical bath deposition monitored by an in situ optical fibre

4.1 Introduction

The chemical bath deposition (CBD) of cadmium sulphide requires a source of Cd ions (here $CdCl_2$) and a source of S ions (thiourea ($CS(NH_2)_2$)). These precursors are combined in an aqueous solution with ammonia. An ammonium salt is used as a buffer within the solution (NH_4Cl was used here). Acetate salts are also commonly used [1] and ethylenediamine has been used instead of ammonia [2].

There are two suggested mechanisms for the formation of CdS, the preferred being the heterogeneous reaction in which CdS forms ion by ion on the substrate surface. Alternatively the homogeneous reaction involves the formation of CdS particles or clusters within the solution. The homogeneous reaction results in particles being adsorbed by the film. This causes the films to be powdery and non-adherent to the substrate [3]. The formation of particles in the solution has also been shown to reduce the potential final thickness of the deposited film and to increase the diffuse scatter of the films deposited [1].

The equilibrium reaction 4-1 is important in the determination of the pH of the solution with the pH being dependent on the ratio of the NH_3/NH_4^+.

$$NH_3 + H_2O \rightleftarrows NH_4^+ + OH^- \tag{4-1}$$

A mechanism for the atom by atom reaction forming CdS has been suggested by Borges and Lincot [4], see equation 4-2. This involves the two step decomposition of the

thiourea with the formation of cyanamide (CN_2H_2).

$$[Cd(OH)_2]_{abs} + SC(NH_2)_2 \rightarrow [(Cd(SC(NH_2)_2)(OH)_2]_{abs} \rightarrow CdS + CN_2H_2 + 2H_2O + site \quad (4\text{-}2)$$

Their work suggested that for the heterogeneous mechanism to be dominant the concentration of the $Cd(OH)_2$ has to be below its precipitation limit. Where the formation of $Cd(OH)_2$ occurs by reactions 4-3 [4] and 4-4 [1]. The homogeneous reaction has been linked with the formation of the cadmium hydroxide bulk precipitate [4]. Similarly it has been suggested that the homogeneous reaction may be suppressed by reducing the amount Cd^{2+} in solution [1].

$$Cd(NH_3)_4^{2+} \rightleftarrows Cd^{2+} + 4NH_3 \quad (4\text{-}3)$$

$$Cd^{2+} + 2OH^- \rightleftarrows Cd(OH)_2 \quad (4\text{-}4)$$

The effect of the major deposition parameters on the growth rate of the deposited layer was studied by Borges and Lincot [4]. Increasing the reaction temperature of the bath would increase the rate of the reaction. Raising the cadmium or thiourea concentration would also increase the reaction rate, while an increase in the ammonia concentration would decrease it, by reducing the pH of the solution. The pH of the solution has also been shown to have an effect on the structure of the deposited film. CdS deposited with a solution pH in the region of $8.5 < pH < 10.5$ was found to be a polytype structure (a mixture of wurtzite and zincblende phases, predominantly zincblende) [5]. Stirring the solution was suggested as a way of stopping the reaction growth rate from being diffusion limited, and it was found that the growth rate of the film was almost independent of the speed of the stirring [4].

Lincot and Borges work examined the change in the growth rate during a deposition and identified three distinct regions [6]. Firstly an induction time was reported where nucleation takes place on the substrate surface. Then a region of linear growth occurs with the growth of a compact layer possibly by an ion by ion growth mechanism. A third region is associated with an increase in the growth rate due to a change in the growth mechanism which creates a porous layer possibly indicating a particle or cluster mechanism. This change in the mechanism shows the chemistry in the solution changes

as the reaction progresses.

Ultrasonic agitation of the solution during a CBD has been shown to reduce the number of CdS particles on the surface of the deposited film [5]. Other research groups have reported cleaning the deposited film with an ultrasonic process after the deposition [1]. This could be linked with the suggested low adherents of the porous layer reported by Lincot and Borges [6].

4.2 Deposition method

The CBD method used in this work was was devised by Ketpearachchi [7]. The method involves weighing out the precursors with the appropriate amount of deionised water so that the total solution volume was 500 ml. The deposition solution contained:

- thiourea (0.057 M),
- ammonium chloride (0.028 M),
- cadmium chloride (0.002 M).

The chemicals used had a purity of 99+% or higher and the deionised water had a resistivity of approximately 16 MΩ cm. During the deposition ammonia solution was added to the solution to keep the pH at approximately 10.5. The solution was placed in a double walled beaker where heated water could be pumped through the walls via a water heater, see figure 4-1. This beaker was placed within an ultrasonic bath. The clean samples were mounted (conducting side up) in a glass mount which was suspended from a motor. The samples could then be rotated in the solution throughout the deposition at approximately 2 Hz. This ensured the solution composition remained homogeneous.

For a deposition the samples were set rotating within a solution at room temperature and then the ammonia solution was added at the same time as the water heater was turned on. The water was heated to a temperature of 70 ± 2 ℃ from room temperature at a rate of 3 ℃ per minute (taking approximately 15 min). When the solution had reached 70 ℃ the ultrasonic bath was switch on. The colour of the solution would then change from clear to pale green, to yellow, through to opaque yellow. A deposition of 15 minutes would deposit an approximately 150 nm thick film. To stop the reaction, the ultrasonic bath and sample motor were turned off and the samples were immediately removed from

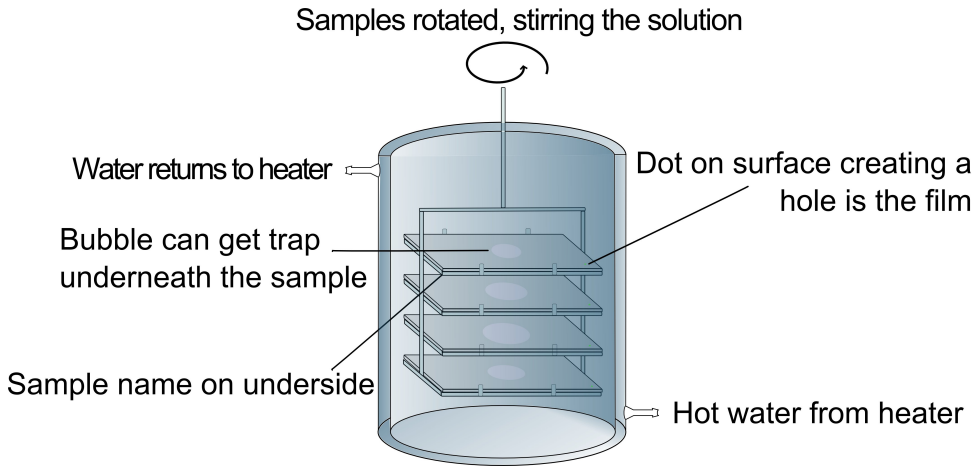

Figure 4-1: A diagram showing the way the samples are mounted in the doubled walled beaker.

the solution, rinsed with deionised water to remove the solution from the surface (to stop the deposition) and then blown dry.

During early experiments Nippon sheet glass (10-FP190C-X45) was used as the TCO substrate, Pilkington Tec 15 glass was used in later experiments, for example during device fabrication. The substrates were cut to a size of 30 x 20 mm for this investigation. They were then cleaned before the CdS deposition by a sequential process. Firstly the substrate surfaces were wiped with a tissue to remove particulate contamination. Then they were rinsed in deionised water, followed with an immersion in acetone to remove organic contaminates, then they were immersed in detergent (Decon 90) to remove salts and finally they were rinsed in deionised water to remove the detergent.

In this procedure the deposition solution along with the ammonia are heated up together to 70 ℃ in the beaker. This causes the determination of the precise starting time of the deposition to be uncertain. This makes predicting the thickness difficult. Monitoring the thickness of the film in situ would allow the start of the reaction to be determined more precisely and also allows the deposition rate of the reaction to be determined. Being able to determine the thickness and growth rate in situ would allow the deposition process to be optimised further for the specific requirements of the deposited film. This has been done by another research group who used a combination of in situ quartz crystal microbalance and electrochemical impedance measurements [6]. The change in the transparency of a CBD ZnS solution has also been used to monitor the deposition in situ [8]. Where the end point of the deposition was determined by measuring a given value

of transparency. This technique was used for depositions of 20 nm thick films and the transparency was required to only change by 20 %. An in situ optical fibre monitoring technique has been used to determine the thickness of sputtered films of titanium and titanium oxide by Caranto *et al.* [9]. Their results matched well with the theoretical calculations in the work of the reflectance from the interfaces at the end of the optical fibre using a two interface (a three medium) expression.

In this work a convenient in situ monitoring technique is suggested using light reflected off of the end of an optical fibre immersed in the reaction solution. The small diameter of the fibres enables the in situ technique to be implemented without any changes to the reaction chamber, and its flexibility allowed for the optical equipment to be positioned in a convenient location.

4.3 In situ optical fibre monitoring of the chemical bath deposition

The principle behind the optical fibre measurements relies on light being sent down an optical fibre and a fraction of the light reflecting off of the end and back along the fibre. The reflection of the light from the end of the fibre is dependent on the optical properties of the interface at the end of the fibre. The basis of this work was that CdS would deposit on the end of the fibre during CBD causing the intensity of the reflected light to change by a measurable quantity. This would enable a measurement of the amount of material deposited on the end of the fibre [9].

The in situ optical fibre measurements where made using SM1550 optical fibre connected to a Lumen Photonics ASE (LPB-1550-D) broadband light source operating at 1550 nm (0.800 eV), the optimum wavelength for the fibre. The fibre passed through a 2 x 2 coupler and was fixed to the inside of the double walled beaker. The optical fibre was positioned carefully within the chamber so that it was close to the wall of the beaker and at least 10 mm from the top or bottom of the solution. The reflected light passed through an Anritsu (MN9664A) optical channel selector and to an Anritsu (MS9710B) optical spectrum analyser. To reduce the number of intensity peaks recorded the bandwidth over which the reflection peaks were monitored was set at 1540 to 1560 nm (0.805 to 0.795 eV). The plastic buffer around the immersed end of the optical fibre was removed

and only the bare fibre was immerse into the bath. The bare fibre has a diameter of 150 µm the majority of which is cladding, only a 6 µm core carries the light. The end of the fibre was cleaved and wiped with isopropanol before the fibre was fixed in place. Between runs the submerged part of the optical fibre was broken off and then the new end could be used for the next run.

The measurement consisted of recording the intensity of the reflected signal with time. The intensity of the reflected light was corrected for the background (R_{back} (nW)). This was done by subtracting the average intensity of the initial solution before the reaction started, from the later measurements. This correction takes into account the difference in the quality of the cleaved surface between different depositions. The measured reflectance intensity, R_m (nW), was converted to the change in the reflectance intensity (ΔR (dB)), see equation 4-5.

$$\Delta R = 10 log_{10} \frac{R_m}{R_{back}} \tag{4-5}$$

The thicknesses of the films deposited on the samples during the depositions were measured using an Alpha step 100 surface profiler. A dot of permanent ink was marked onto the clean conducting surface of the TCO before the CdS deposition. After the deposition the samples were rinsed in acetone causing the dot of permanent ink to dissolve dislodging the CdS deposited on it. The surface profiler was then used to measure the thickness of the deposited layer.

4.4 Theoretical reflection from optical fibre interface

The reflection of light from the end of the optical fibre was modelled as the reflectance from the interfaces between three media, see figure 4-2. Where the first medium is the optical fibre core with a refractive index (n_0) of 1.46, secondly the CdS film on the end of the fibre with a refractive index (n_1) of 2.25 (at 1550 nm CdS thin film [10]) and thirdly the solution which was approximated to water with a refractive index of 1.33 (n_2). The reflectance R is then given by equation 4-6, ([11] Page 73).

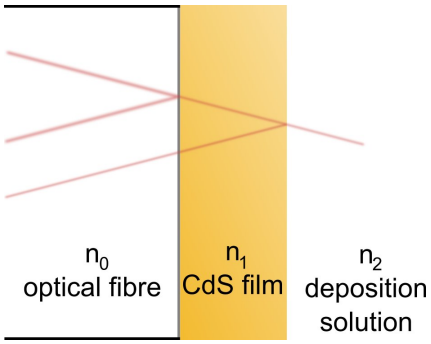

Figure 4-2: The optical model used for the calculations with three different optical mediums at the interface at the end of the fibre.

$$R = \frac{r_1{}^2 + 2r_1r_2cos2\delta_1 + r_2{}^2}{1 + 2r_1r_2cos2\delta_1 + r_1{}^2r_2{}^2} \tag{4-6}$$

$$\text{Where} \quad r_1 = \frac{n_0 - n_1}{n_0 + n_1}, \qquad r_2 = \frac{n_1 - n_2}{n_1 + n_2} \tag{4-7}$$

$$\text{and} \quad \delta = \frac{2\pi}{\lambda} n_1 d_1 cos\psi_1 \tag{4-8}$$

Where λ is the wavelength of the light in nm (1550 nm), d_1 is the thickness of the middle medium, the CdS films, and ψ_1 is the angle of incidence, which is assumed to be normal incidence in this case and so has a value of zero. The optical fibres have a 16.8° cone of acceptance for light to be transmitted along the optical fibre (light can be at a maximum of ± 16.8° from the normal of the fibre).

The change in the intensity of the reflected light was then calculated using the reflectance for when no CdS film was present, as a reference point. The change in reflectance for different thickness of CdS film is given in figure 4-3. A maximum reflectance occurs when the optical thickness (t_m) is equal to one quarter of the wavelength of the light, see equation 4-9. The calculations show that ΔR is not very sensitive to small variations in the thickness of the middle medium, in the region 150 to 200 nm.

$$t_m = \frac{\lambda}{4n_2} = \frac{1550}{4\times 2.25} = 172.2\,nm \tag{4-9}$$

4.5 Optical fibre measurements

The results from the initial experiments clearly showed a change in the intensity of the reflected signal with time, see figure 4-4. The start of the reaction can easily be identified

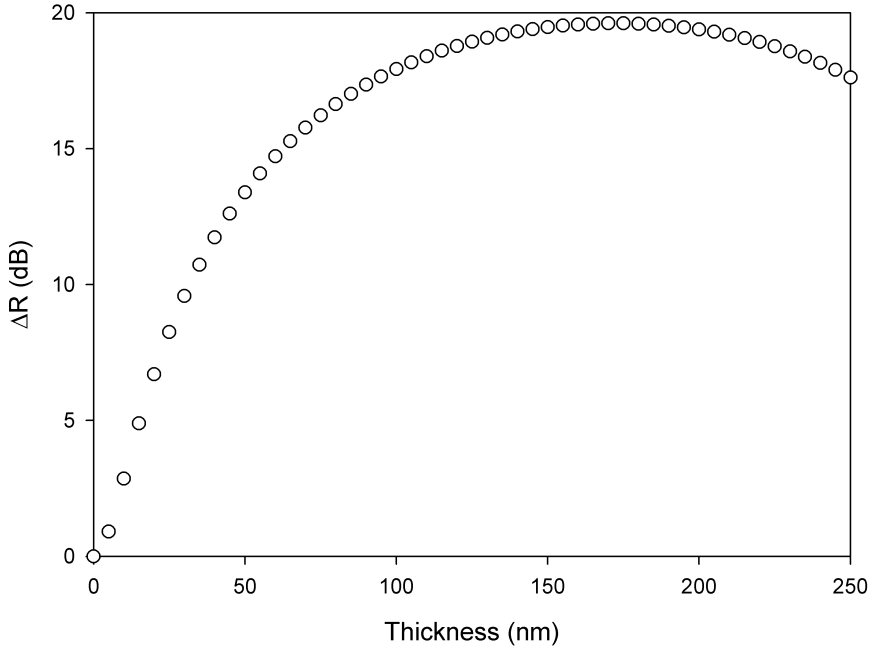

Figure 4-3: The variation in the calculated ΔR with film thickness, for light with a wavelength of 1550 nm. It shows a significant change in the reflectance can be expected during CdS deposition.

by the sharp increase in the change of reflectance. The change of ΔR with time does not vary as would be expected if the change was due to the variation in thickness of the film alone, compared with figure 4-3. This result suggests the growth rate of the material on the end of the fibre changes during the reaction or another process is affecting the intensity of the reflected light.

The deposition time of the CBD was varied so that the final thickness of the deposited films on the samples would vary without requiring any change of the other deposition parameters. The thickness of the CdS deposited on the samples was measured and plotted against the largest change in the reflectance for each of the depositions, see figure 4-5. The calculated and measured values for ΔR appeared to follow the same trend. However the calculated data consistently had a higher ΔR value then those values found experimentally.

In order to assess the assumptions of the model, some of the parameters were varied to allow the model to be fitted to the data. The quality of the models fit to the data was calculated by summing the square of the difference between the data and values calculated from the model, giving the RMS value, a value of zero would show perfect

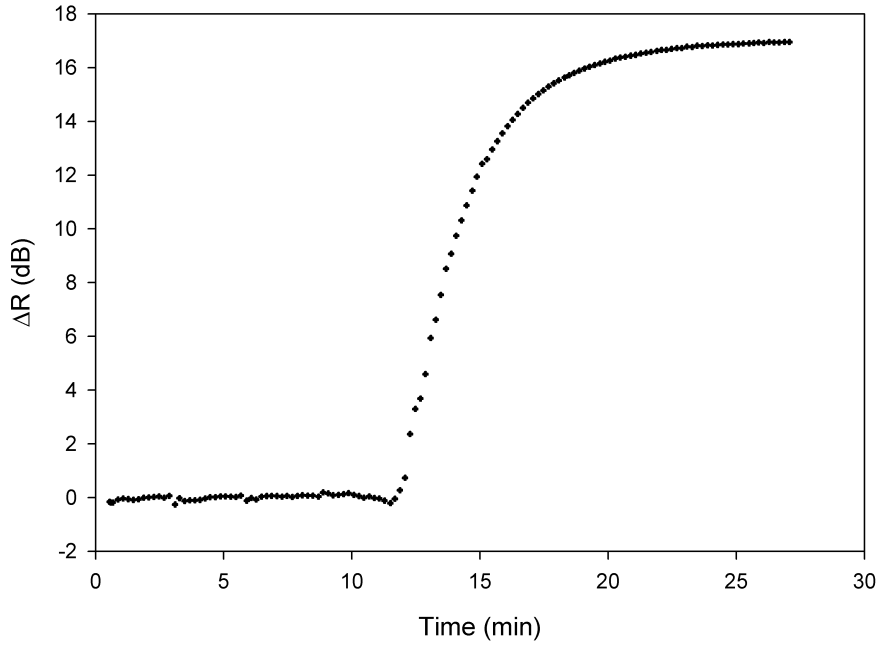

Figure 4-4: The change of the intensity of the light reflected from the end of an optical fibre during a CBD run.

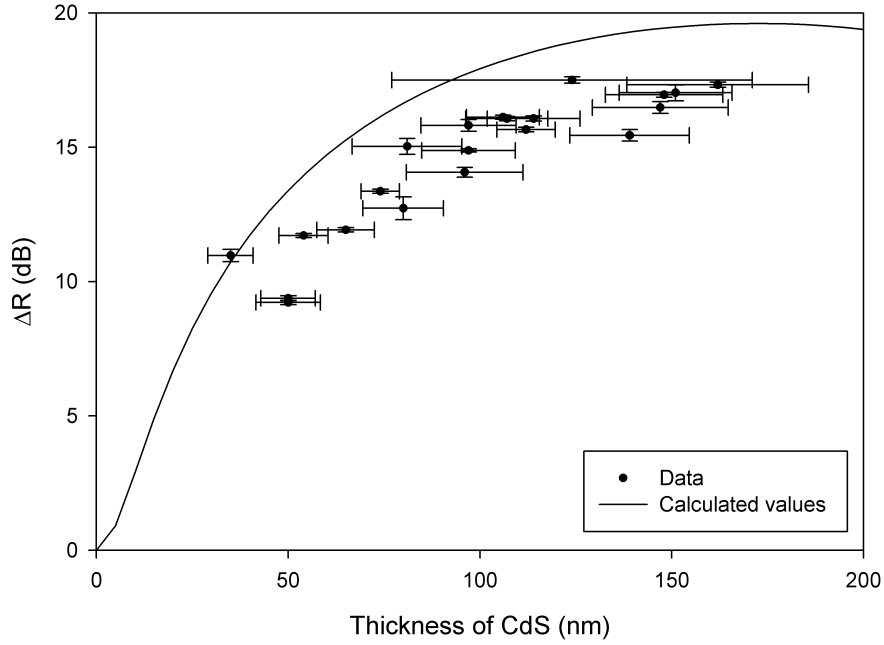

Figure 4-5: The change in reflectance intensity at the end of the deposition is plotted against the thickness of the CdS deposited on the samples. The calculated values from the previous section are also included for comparison.

agreement.

Two model parameters were varied to see their influence on the RMS value, the refractive index of the middle medium and the angle of incidence of the light on the interface, see table 4-1. The angle from the normal to the optical fibre surface has to be 16.8° or less so that the light undergoes total internal reflection as it pass along the fibre. If this angle is used instead of assuming all the light is normal to the surface, the RMS value of the fit changes from 2.76 to 1.09. When the optical constants of the CdS material were varied to allow the model to fit the data, the minimum RMS value reduced to 0.98. This improvement in the RMS may be linked with the CdS layer having a double layered structure, described in Lincot and Borges work, and the change in the optical constant represents a better approximation of the doubled layer structures properties [6]. Although changing both parameters was found to improve the agreement between the model and the data, other factors may influence the results and are discussed in later sections.

Equations 4-5 to 4-8 were used with the data collected for two depositions to calculate the approximate thickness of the layer as a function of deposition time, see figure 4-6. It can be seen from the figure that initially the deposition changes linearly during the deposition, in agreement with the results reported by Lincot and Borges [6] for heterogeneous deposition. The start time of the reaction is not defined in the same way as it was in their work, so no comment on the induction time reported in that work can be made here. The deposition rate observed here implies that two deposition mechanisms are dominant at different times during the longer depositions. While the ultrasonic bath used in this work was intended to reduce the adsorption of large particles on the surface of the film it

Table 4-1: The effect of varying two parameters on the RMS value is presented, where the model has been fitted to the alpha step thickness measurements. Other model parameters were held constant. The top (highlighted) parameters were used to generate the theoretical values displayed in the graphs.

Angle of light on interface (°)	**Refractive index of CdS, medium 1, (n_1)**	**RMS value**
0	2.25	2.76
16.8	2.25	1.09
0	2.02 (fitted parameter)	0.98

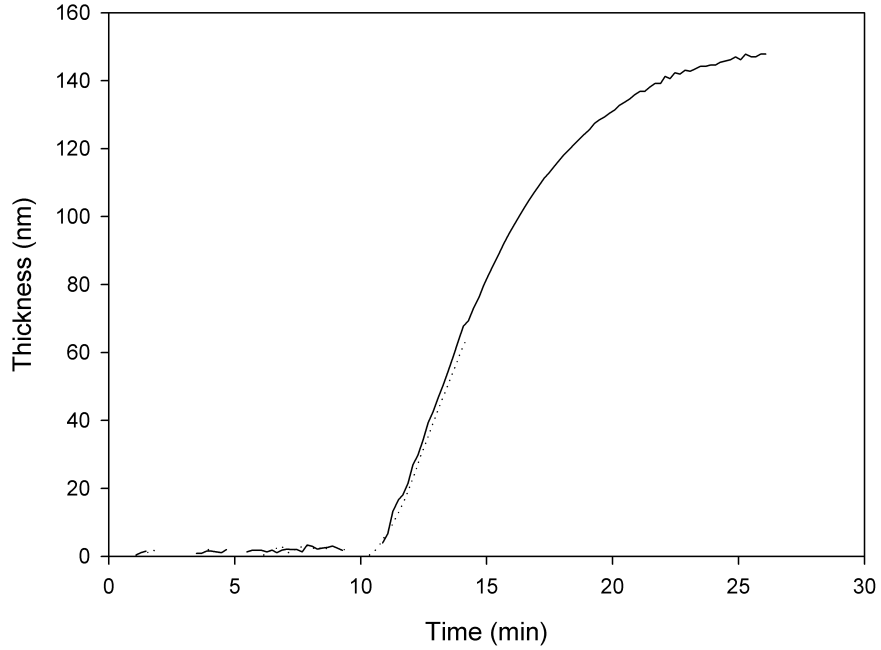

Figure 4-6: The change in the approximate thickness of the film with time, for two depositions, calculated from the change in the reflectance. For these two depositions the thickness of the layers on the samples measured after the deposition were 148 ± 15.3 nm (solid line) and 65 ± 7.5 nm (dotted line).

does not seem to have any effect on the deposition mechanism, with the linear region for heterogeneous deposition followed by a non linear region for homogeneous deposition.

In the above work it was assumed the measured change in the reflectance is due to a thin film deposition on the end of the fibre. The possibility of changes within the reaction solution and direct measurement of the film on the end of the optical fibre are discussed below.

4.6 Near infra red spectroscopy of solution

The optical model described in the previous section assumed that the refractive index of each material remains constant during film growth. However as the films were deposited the bath solution becomes depleted and its optical properties may change. The change in the optical absorbance of the reaction solution under heating was investigated using a spectrometer.

Thin vessels were created to contain a small amount of reaction solution. These were

fabricated from three microscope cover slips. One of the cover slips was used to create a u-shaped spacer which was fixed between the other cover slips with resin. A small amount of reaction solution including the ammonia solution was placed in the vessel using a syringe. This vessel was then loaded into a heating mount within a Nicolet (Magna IR 760) spectrometer. The spectrometer was setup to take a measurement every 30 seconds. The solution was then heated to 71 ℃ over 20 min and then held at that temperature for 60 min, while the chemical reaction occurs. A selection of the spectra collected at different times during the measurement can be seen in figure 4-7.

The two large absorbance peaks are possibly due to water absorbance but there could also be contribution from the ammonia and primary amine groups within the solution [12]. Further analysis would be required to confirm the levels of contribution from the different groups. The spectrum shows a small change over the period of the measurements. As the solution was heated the energy of the bonds within the material changes and this would cause a small shift in the absorbance peaks [12]. Also as the solution was heated water would evaporate and so the concentration of the solution would increase.

Only a small amount of solution was used in this measurement and the solution was

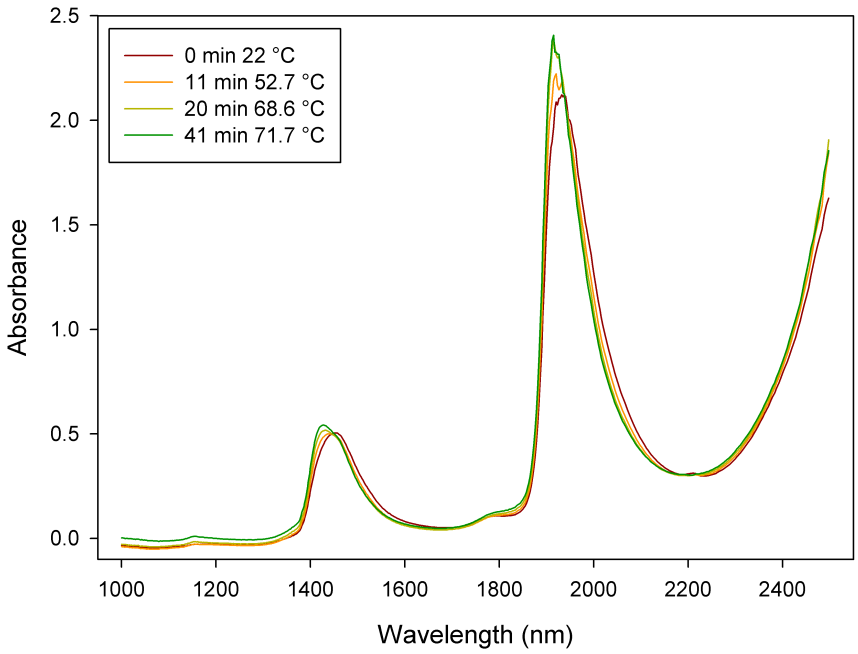

Figure 4-7: The near IR absorbance spectrum of a small amount of the reaction solution as it was heated to and then held at 71 ℃. The wavelength of the light used in the optical fibre measurements was 1550 nm.

not stirred or mixed during the measurements. It is therefore suggested that any solid material which formed particles within the solution during the deposition settled at the bottom of the vessel and did not effect the measurement significantly. This result partially validates the assumption that the change in the reflectance measured in the optical fibre data is due to the deposition of a film on the end of the fibre and not a change in the properties of the solution.

4.7 Rutherford backscattering of optical fibres

The thickness of the deposited CdS on the end of the optical fibre has been assumed to be similar to the CdS deposited on the samples. Rutherford backscattering spectrometry (RBS) measurements at Surrey University were used to measure the thickness of the deposited material on the end of six optical fibres. Scanning electron microscopy (SEM) was used to examine the ends of the fibres measured by the RBS, see figure 4-8) The SEM images showed that three of the optical fibres had non ideal CdS coverage across the end of the fibre, an example can be seen in figure 4-8(d). However only the 6 μm core in the middle of the fibre carries the light and so only the uniformity in this region is of a concern. The three non uniform optical fibres coincidently corresponded to the fibres with the lowest ΔR, for the six fibres.

The non uniformity of the films on the ends of the fibres may possibly be explained by considering the variation in the mounting of the fibre near the beaker wall. The fibre was mounted so that it may or may not be in contact with the walls of the beaker, and this variation may have resulted in the observed variation in the uniformity of the films.

Surrey University has a 2 MV Tandem accelerator. To study the end of the fibres a 1.557 MeV $4He^+$ beam was used with a spot size of approximately 10 μm × 10 μm and a beam current of approximately 300 pA. A RBS detector was position at 155 ° scattering angle and a particle induced x-ray emission (PIXE) detector (a E2V Si(Li) 80 mm^2 crystal) was positioned at 45 °.

The PIXE results showed the presence of Si, Cd, S and Cl. The uniformity of the Cd across the surface from the PIXE measurements agreed with the uniformity of the SEM images (not shown). It was possible to identify some of the samples from the PIXE images of the Cd distribution. The results indicate the CdS deposited was not stoichiometric,

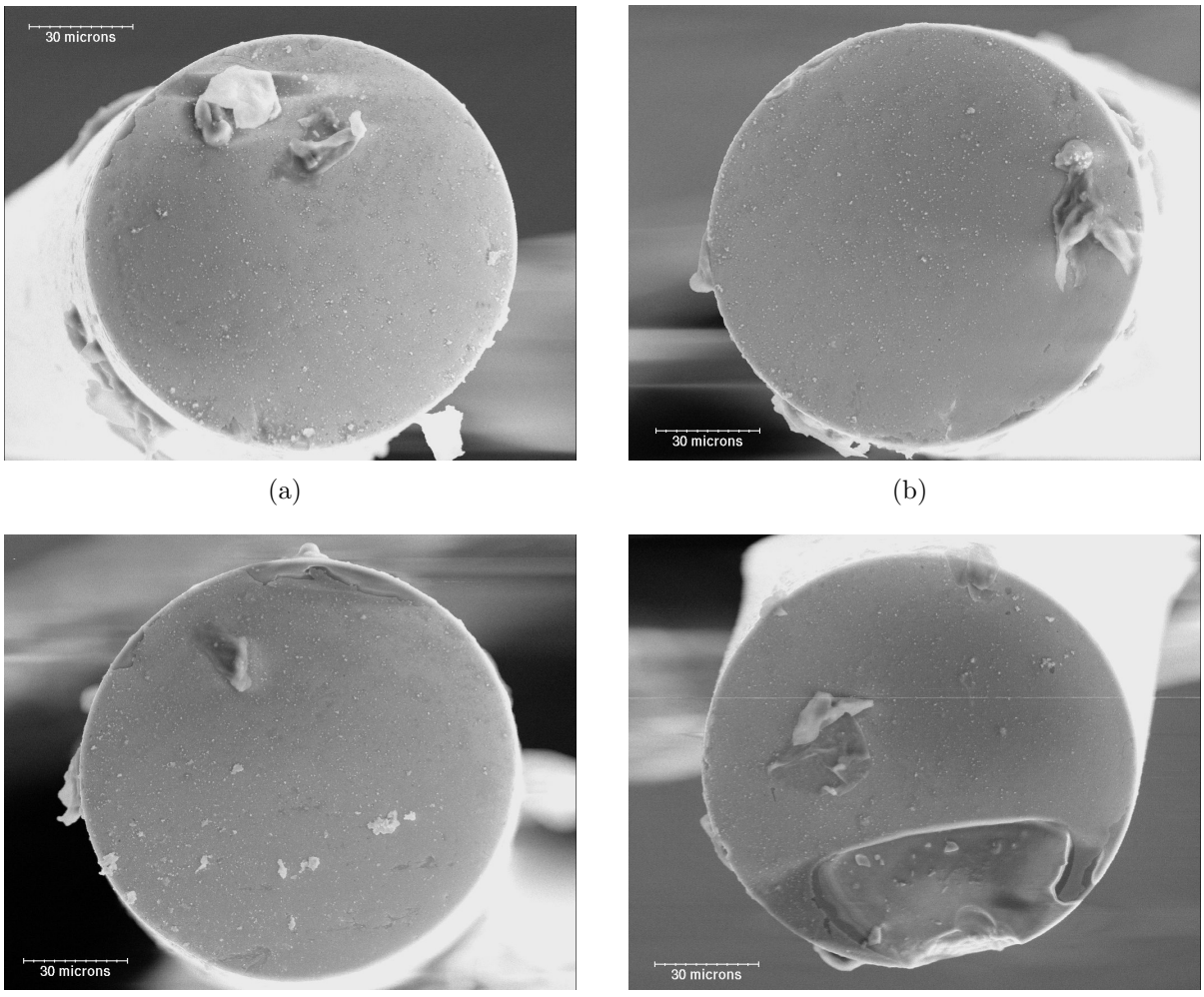

(a) (b)

(c) (d)

Figure 4-8: SEM images of the ends of four optical fibres from the CdS depositions. Three of the six optical fibres visibly did not have uniform CdS coverage on their end surface (only one of these fibres is shown here (d)). Scale bar represents 30 μm.

Table 4-2: Compares the surface profiler measurements of thicknesses made on the samples to the RBS measurements of the films on the end of the optical fibres, which were deposited in the same deposition. The table also shows the Cd:S ratio of the CdS material determined by PIXE.

	Six different optical fibres and their corresponding samples					
Thickness of samples measured by Alpha step (nm)	54 ± 6	80 ± 11	98 ± 12	112 ± 8	147 ± 18	148 ± 15
PIXE determined Cd:S ratio (error 10% or less)	1.39	1.32	1.14	1.40	1.30	1.26
RBS thickness of Cd (1 e^{15} atom/cm^2) (error 1.5% or less)	47.4	106.7	132.8	139.9	160.5	159.7
RBS thickness of S (1 e^{15} atom/cm^2) (error 9.5% or less)	34.1	80.8	116.7	123.9	127.0	100.1
Approximate film thickness on optical fibre calculated only using Cd values assuming stoichiometric CdS (nm)	23.6 ± 0.3	53.0 ± 0.6	66.0 ± 0.7	69.5 ± 0.7	79.8 ± 1.2	79.4 ± 0.7

they show the samples to be Cd rich, see table 4-2. The uncertainty in the sulphur values and not knowing the density of the proposed composition meant the thickness of the film could not be directly calculated. The thickness was approximated using only the cadmium concentration and assuming that the cadmium was present as stoichiometric CdS. This allowed the thickness to be calculated using the density and molar mass of CdS (see appendix A.1 for details). Using these assumptions to calculate the thickness, the results indicate that the films deposited on the end of the optical fibre are thinner then the films deposited on the samples.

The RBS models used to analyse these films included an oxygen component (not shown). The presence of oxygen within CdS deposited by CBD and the effect on the material has been reported by other groups [13]. The presence of oxygen within the film may cause the film to be thicker than the values calculated and it may also affect the optical constants of the layer.

The thicknesses calculated from the RBS measurements for the films on the fibres agrees much better with theoretical ΔR values, compared to the thicknesses of the films on samples measured by the surface profiler, see figure 4-9. This shows that the change in the reflectivity calculated from the optical model (using the original parameters) may

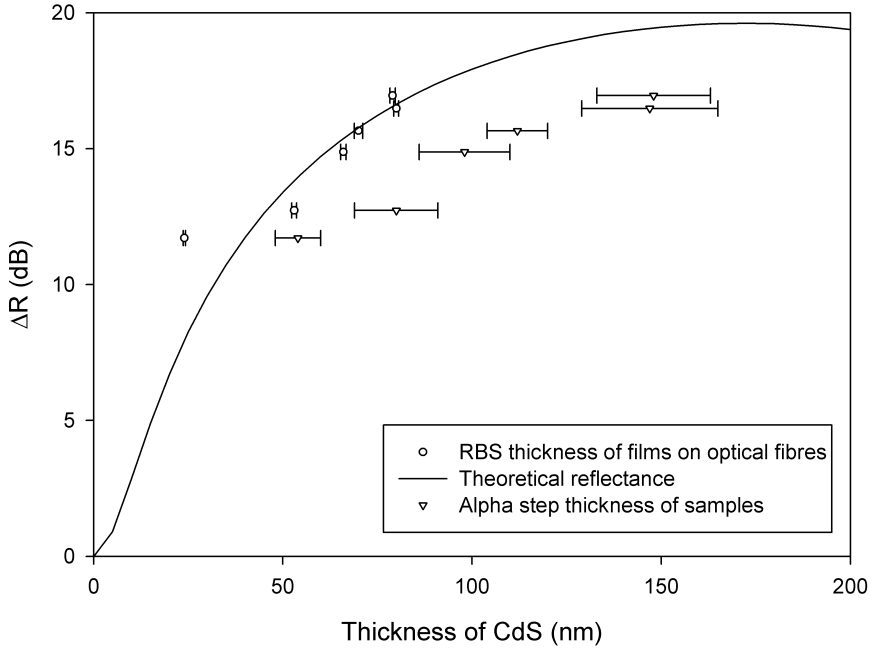

Figure 4-9: The thickness of the films on the optical fibres calculated from the RBS data is compared with the thickness measured by the surface profiler for the layers deposited on the corresponding samples. The errors for the RBS measurements were calculated from the uncertainty in the Cd thickness.

more accurately represent the fibre interface using the thicknesses found with the RBS measurements (a RMS of 1.67 was found for the six thicknesses).

The presence of Cl in the PIXE measurements for the optical fibre (not shown) may indicate contamination from the hydrochloric acid used to clean the deposition beaker between deposits. The same procedure was used through out the work in this thesis and so the presence of Cl may need to be considered in the following chapters.

4.8 Ellipsometry measurements

Individual layers of CdS were grown on the silica substrates to provide simple, controlled structures for ellipsometry measurements. These measurements allowed an oscillator model to be created for the CdS. Work by Ninomiya and Adachi produced a detailed oscillator model for single crystal CdS based on the energy band structure of wurtzite CdS [14]. This model was used as a guide to create a model for polycrystalline material in this study. To create a model, a Cauchy oscillator was used to fit the optical constants of

the silica substrates (for details see appendix A.2). For an as-deposited CdS layer, three oscillator functions were used to model the optical constants: a Cody Lorentz oscillator and two Lorentzian oscillators.

The single layer of as-deposited CdS was initially modelled by a single layer within the model, see figure 4-10. However this model did not produce a good match to experimental data, with a MSE of 25.87. A second model with two layers representing the CdS produced a very good match to the data, with a MSE 3.44, see figure 4-11. The first layer was comprised of the three oscillators which modelled the broad optical constants of CdS, see figure 4-12. A second layer combined the properties of the first CdS layer with those of a 'void' material (n = 1, k = 0) in an effective medium approximation layer (EMA) using a Bruggeman function. Details of these models can be seen in the appendix A.2. The inclusion of the second layer improved the quality of the fit around and above the band gap. The second layer indicates the presence of a less dense layer of CdS on top of dense CdS. This agrees with the CBD mechanism proposed in the literature by Lincot and Borges [6]. Work by Podesta *et al.* found fitting ellipsometry data for undoped CdS deposited by sputtering was greatly improved with the presence of an EMA layer on top of the oscillator layer [15]. In their work, the EMA was used to model surface roughness with the percentage of void material to CdS fixed at 50:50. However work by Sandoval-Paz *et al.* used spectroscopic ellipsometry to suggest properties of the microstructure of the CdS layer deposited by CBD [16]. Their work refers to the reults of Lincot and Borgers and they gave details of the thicknesses of the two layers used in their model for films deposited for different lengths of time. They found the two layer model worked well for films deposited with sodium citate, while only an EMA layer was used to model films with an ammonia agent. The results of the current work suggest that differences in the procedures cause the ammonia base deposition in the present study to have an ion by ion dominant mechanism for a longer time. This causes the compact CdS layer to be observed in the present studies ellipsometry analysis.

The samples deposited during the optical fibre monitoring were deposited on Nippon TCO glass. No optical model of this glass could be found in the literature and so the physical accuracy of the model's assumed multilayered structure could not be verified. A model for the Nippon glass was constructed for the limited wavelength range 245 to 1200 nm. The fit produced an MSE of 8.65, see figure 4-13 and for details see

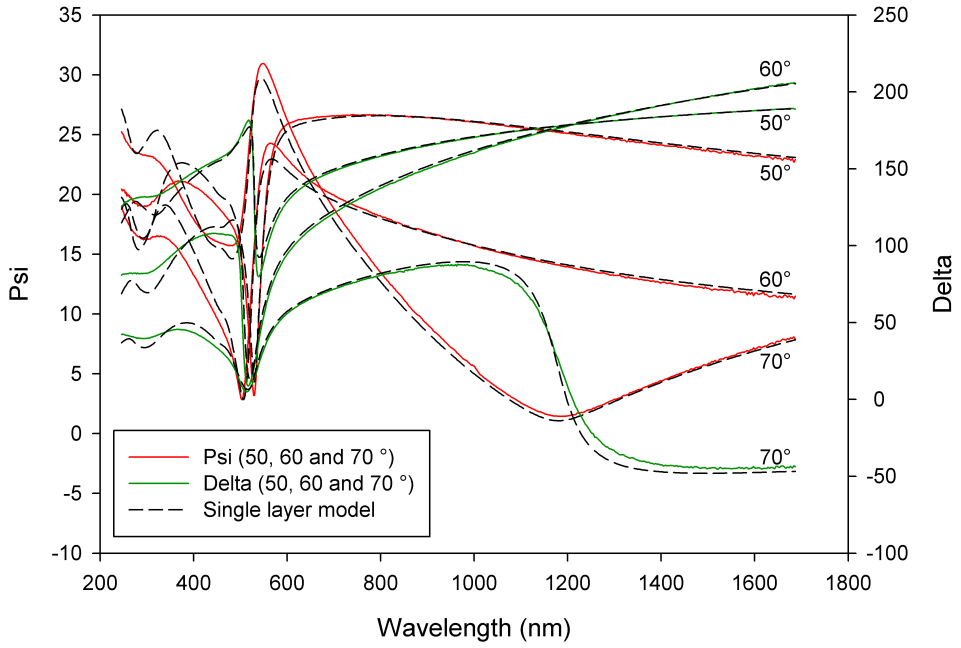

(a)

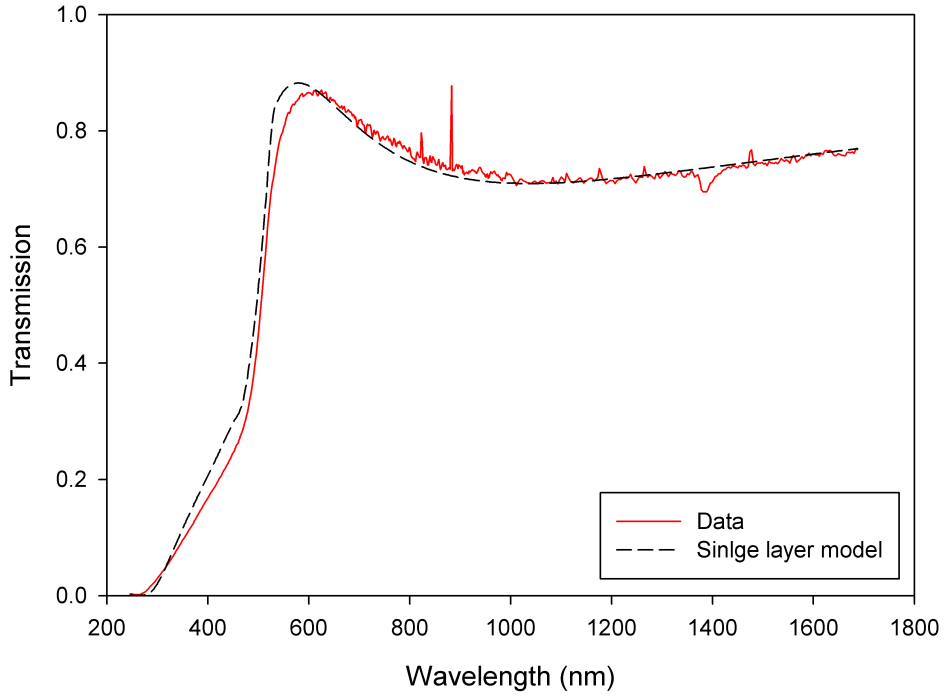

(b)

Figure 4-10: Ellipsomtry data for as-deposited CdS on a silica substrate modelled with a single layer. The figure shows data measured in (a) reflection and (b) transmission modes. The model fitted the data with a MSE of 25.87.

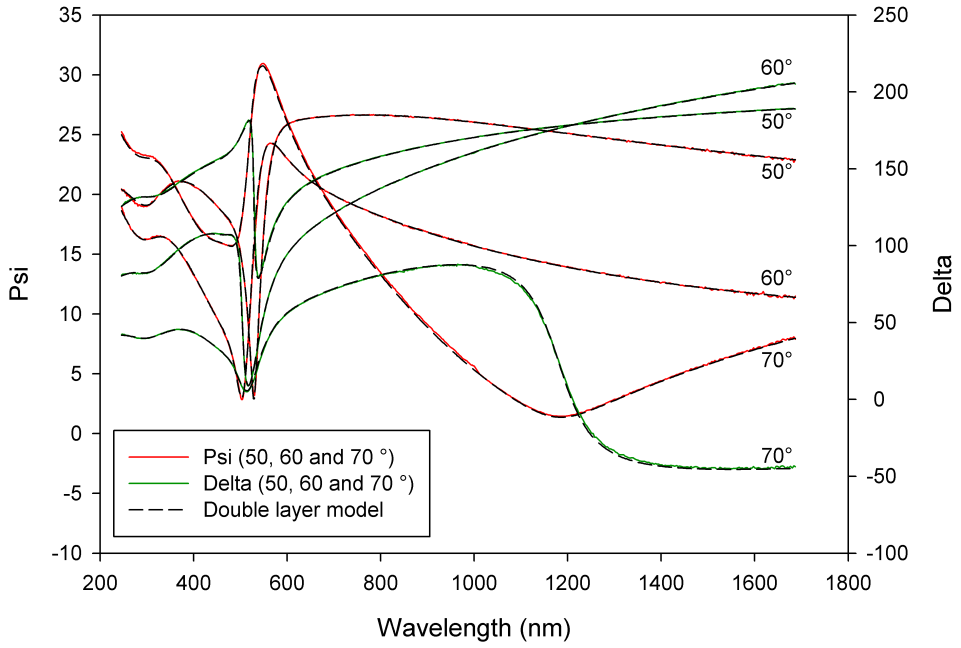

(a)

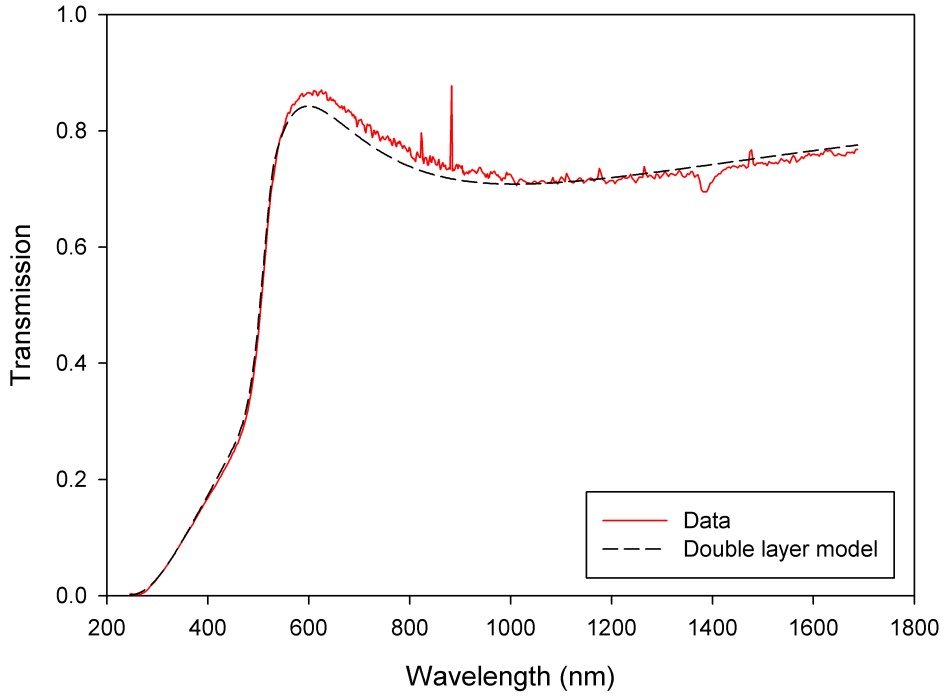

(b)

Figure 4-11: Ellipsomtry data for as-deposited CdS on a silica substrate modelled with a double layer. The figure shows data measured in (a) reflection and (b) transmission modes. The model fitted the data with a MSE of 3.44.

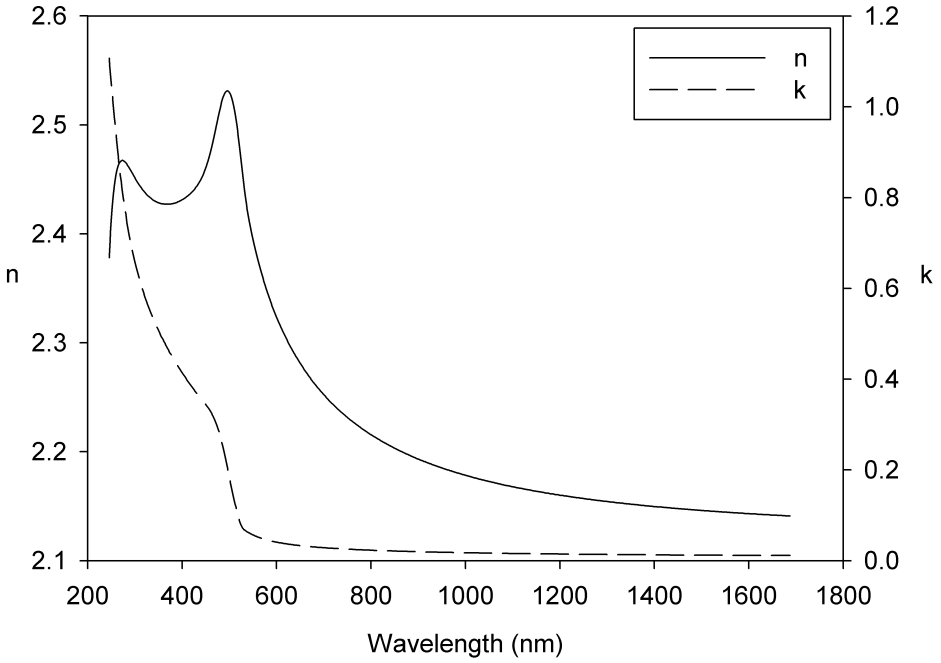

Figure 4-12: Optical constants found for as-deposited CdS on a silica substrate.

appendix A.2.

The samples from the optical fibre depositions were fitted by combining the model of the Nippon TCO glass with the model of the CdS layers on the silica substrate. The only parameters of the model which were allowed to vary were the thicknesses of: the roughness layer, CdS EMA layer and CdS oscillator layer. The optical constants of the CdS layer were held constant. The MSE of the fit to the data varied from 21 to 47, with the model fitting thicker films slightly better than the thinner ones, see figure 4-14. It was proposed that the proportion of the EMA layer as a component of the total CdS model thickness would increase as the thickness of the films increased. This would be expected for longer depositions where more of the film was deposited when the homogeneous process was dominant. The thickness of the EMA and oscillator layers in the fitted model is shown in figure 4-15. The results show the thickness of EMA did not change significantly as the thickness of the CdS films increased. The reason behind this result is unclear. The models which fitted with an MSE close to 40, highlights the possible inaccuracy of the model to match the data, due to the limited number of fitting parameters. An additional contribution towards the models inaccuracy may be due to the optical constants of the CdS layer, which were originally refined for one thickness of CdS film. If the model does

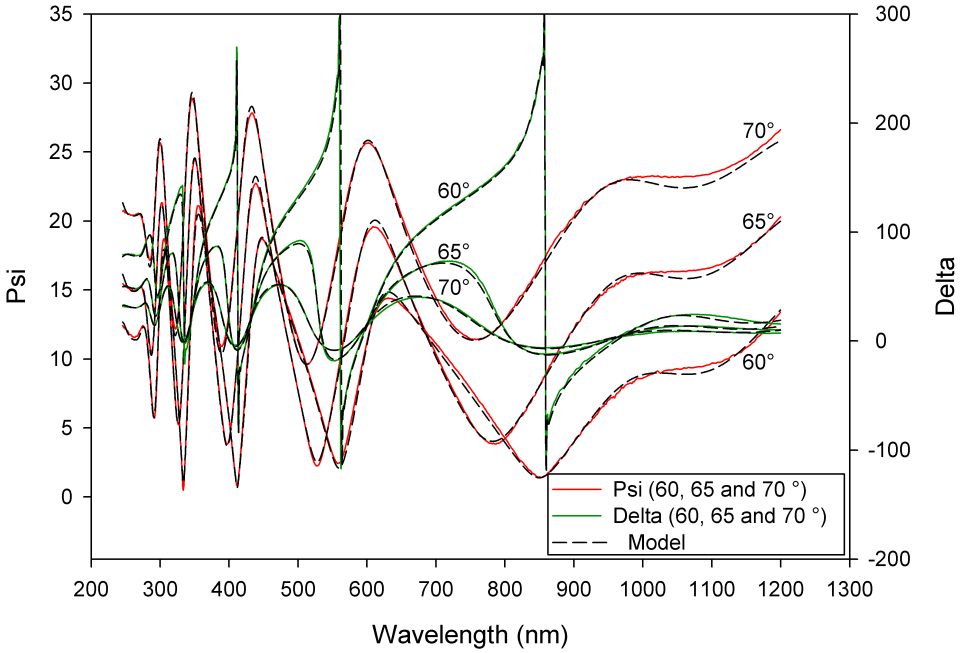

(a)

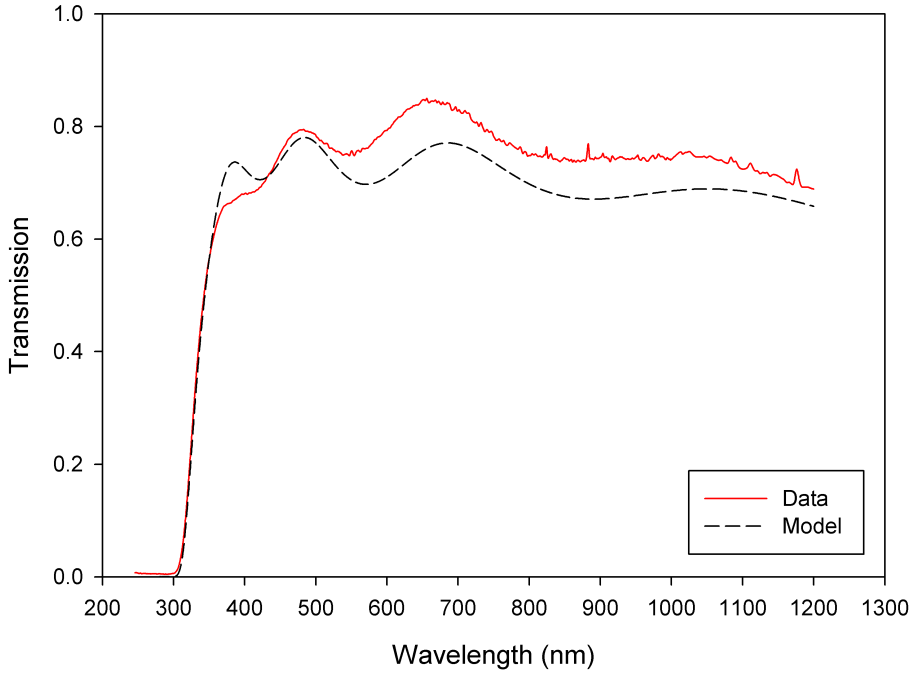

(b)

Figure 4-13: The figure shows (a) the Psi and Delta measurement parameters and (b) the transmission for Nippon TCO glass fitted with a multilayered model to produce an MSE of 8.65.

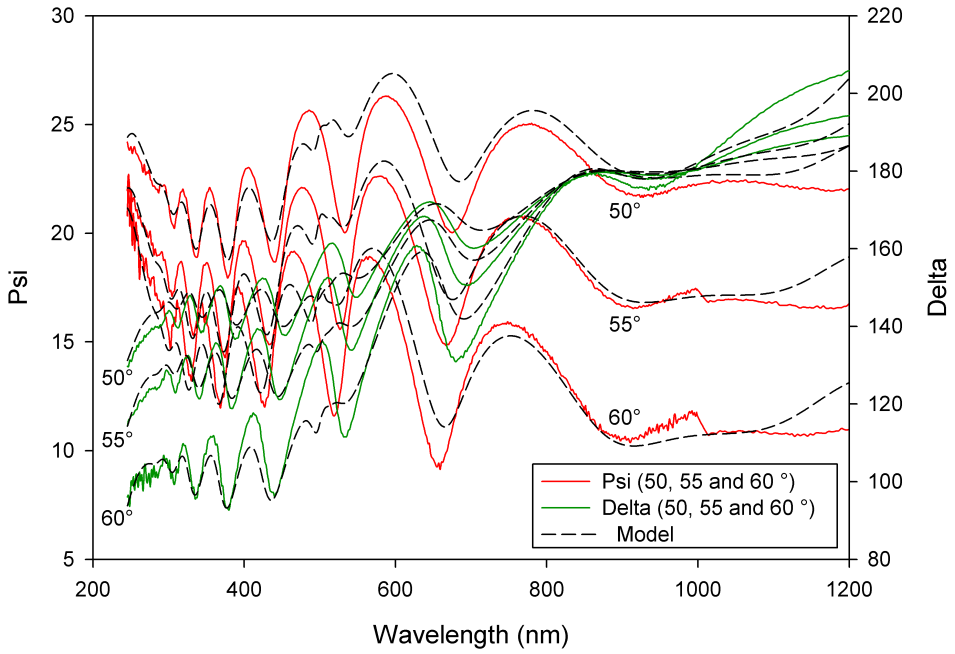

Figure 4-14: An example of Psi and Delta for a sample of CdS on Nippon TCO glass deposited during an optical fibre monitored deposition. The model fitted to the data with a MSE of 35.25.

accurately represent the samples, then it could imply a process where the spaces in the porous material are filled by the heterogeneous process with time. This could limit the thickness of the porous material in the final samples.

4.9 Conclusions

An optical fibre placed within a CBD reaction solution showed a change in ΔR (the change of reflectance) during the deposition. As the theory suggested the reflectance is sensitive to the presence of a thin film on the end of the fibre. The sensitivity decrease as the film thickness approaches 150-200 nm which is a typically final thickness. As an in situ technique it is well suited to identify the start point of the reaction characterised by the sharp increase in the change in the reflectance.

Although the thicknesses of the films deposited on the end of the optical fibres were not the same as those of the films on the samples there seems to be a similar trend. This enables this technique to be used to monitor the thickness of the deposited films during the CBD process. The results from the calculated in situ thickness against time show

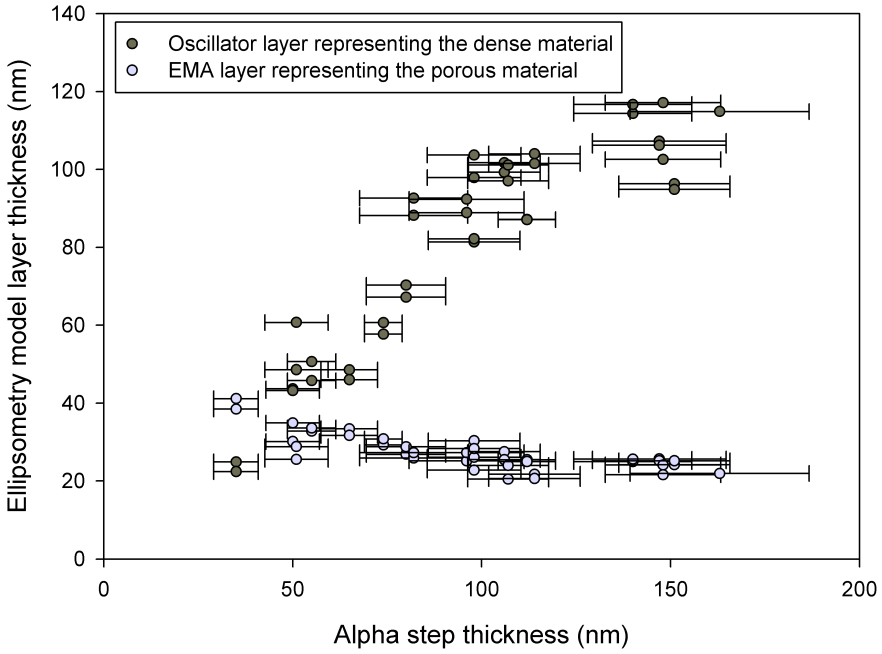

Figure 4-15: The layer thicknesses of the CdS EMA and oscillator layers for a multilayered model fitted to CdS deposited on Nippon TCO glass

two deposition mechanisms are present in the longer CBD depositions. However if the deposition was stopped after approximately 100 nm had been deposited the film would have been deposited with a near constant deposition rate. This would correspond to the whole layer being deposited while a single deposition mechanism is dominant, which has been suggested to be the heterogeneous mechanism [6].

The near infra red spectroscopy of the solution showed a small change in the absorption during a reaction deposition and this partially justified the assumption of the parameters used in the theoretical model.

The model used in this work is in reasonable agreement with the thickness calculated by the RBS measurements on the optical fibres. This is consistent with the agreement between theory and measurements found by other research groups for other deposition techniques [9]. The quality of the fit to the data can be improved through adjusting the angle of the light at the interface and the refractive index of the middle medium. However without more information on the inaccuracy of each parameter it has not been possible to suggest how they could be adjusted to create a better fit to the data with physically relevant approximations.

A possible explanation for the thinner films on the optical fibre compared to the

layers on the sample may be that there is a different nucleation stage due to the different substrates (silica compared to TCO).

The two layered optical structure used to model the as-deposited CdS in the ellipsometry indicates a source of error in the expression used to model the reflectance for the optical fibre. The expression used assumed a homogeneous layer with a single refractive index value.

References

[1] I. O. Oladeji and L. Chow, Journal of the Electrochemical Society **144**, 2342 (1997).

[2] M. Archbold, D. Halliday, K. Durose, T. Hase, D. Smyth-Boyle, and K. Govender, in *31st IEEE Photovoltaic Specialists Conference* (2005), p. 476.

[3] T. L. Chu and S. S. Chu, Solid-State Electronics **38**, 533 (1995).

[4] R. Borges and D. Lincot, Journal Electrochemical Society **140**, 3464 (1993).

[5] U. Ketipearachchi, D. Lane, K. Roger, J. Painter, and M. Cousins, in *Materials Research Society Fall Meeting* (2004).

[6] D. Lincot and R. O. Borges, Journal of The Electrochemical Society **139**, 1880 (1992).

[7] U. S. Ketipearchichi, Ph.D. thesis, Cranfield University (2005).

[8] R. Saez-Araoz, D. Abou-Ras, T. P. Niesen, A. Neisser, K. Wilchelmi, M. C. Lux-Steiner, and A. Ennaoui, Thin Solid Films **517**, 2300 (2009).

[9] N. R. Y. Caranto, S. C. Kadduk, J. Szajmans, M. M. Murphy, S. F. Collins, and D. J. Booth, Measurement Science & Technology **4**, 865 (1993).

[10] E. D. Palik, *Handbook of optical constants of solids* (Academic Press, 1997).

[11] O. Heavens, *Optical properties of thin solid film* (Butterworths Scientific Publications, 1955).

[12] J. Workman and L. Weyer, *Practical guide to interpretive near-infrared spectroscopy* (CRC Press, 2007).

[13] R. Jayakrishnan, S. Kumar, and R. Pandey, Semiconductor Science and Technology **9**, 97 (1994).

[14] S. Ninomiya and S. Adachi, Journal of Applied Physics **78**, 1183 (1995).

[15] A. Podesta, N. Armani, G. Salviati, N. Romeo, A. Bosio, and M. Prato, Thin Solid Films **511**, 448 (2006).

[16] M. G. Sandoval-Paz, M. Sotelo-Lerma, A. Mendoza-Galvan, and R. Ramirez-Bon, Thin Solid Films **515**, 3356 (2007).

Chapter 5

Close space sublimation equipment

5.1 Introduction

A new piece of equipment was designed and built for this project to deposit CdTe by close spaced sublimation (CSS). The main design requirement for the equipment was to minimise the number of sources of extrinsic impurities which could be included in the deposited film. This requirement lead to a design which minimised the number of impurity sources that would be heated to high temperatures and reduced the number of wires required to enter the chamber.

Expressions for the growth rate of material deposited by CSS are considered. The equipment and some aspects of the development are described. The films deposited by the equipment for varying deposition parameters are discussed.

5.2 Theory

Sublimation describes the direct phase transition between a solid and gas state. A close space sublimation deposition is dependent on:

- the sublimation process at the surface of the source,
- the transport of the gas from the source to the substrate surface,
- the sublimation process at the surface of the substrate.

Phase diagrams of CdTe show a very narrow composition where the CdTe binary compound exists as a solid without any other phases, with an atomic percentage of

tellurium equal to approximately 50 %. The melting point of the material is also a maximum at this point and equal to 1099 ℃ [1]. Calculation by Greenberg, calculated the range of tellurium concentration over which the material is in a purely solid phase to be 49.996 to 50.012 atomic percent [2]. A pressure phase temperature diagram of CdTe has also been published which indicates the boundary of a solid to vapour transition [3]. The sublimation of CdTe occurs in the region where the CdTe is in a pure solid phase as calculated by Greenberg. This region is defined by the solid liquid vapour transition as the upper limit, the sides are defined by the limits of Cd and Te saturation in CdTe and the bottom is defined by the line of stoichiometric congruent sublimation (where the vapour has the same composition as the solid) [4]. The sublimation reaction is reported to be [5]:

$$CdTe(s) \rightleftarrows Cd(g) + \frac{1}{2}Te_2(g) \tag{5-1}$$

However several other vapour species are possible although the absence of $CdTe_2$ gas and the presence of a Te_4 gas species have been reported [5]. The vapour partial pressure of the Te_2 (p_{Te_2}) for congruent sublimation of CdTe is approximately given by [6];

$$logp_{Te_2}(atm) = \frac{-1.00 \times 10^4}{T} + 6.346 \tag{5-2}$$

Work by Brebrick and Strauss presented the ratio of the partial pressures, $p_{Cd}/p_{Te_2} = 2.00$ [6]. Using this equation values for the partial pressures at a typical source temperature (650 ℃) were calculated to $p_{Te_2} = 0.033$ mbar and so p_{Cd} would equal 0.066 mbar.

Depending on the deposition parameters the process can be described as either diffusion limited or the sublimation limited case [7, 8]. Alamri [7] calculated the mean free path (h) of the atoms and molecules of the source material for the deposition parameters, using equation:

$$h = \frac{kT}{\sqrt{2}\pi d^2 P} \tag{5-3}$$

Where k is Boltzmann's constant, T is the temperature, d is the diameter of the gas molecules and P is the pressure. The principle suggestion was that the sublimation limited case would end as the pressure of the chamber was increased, when the mean free path was less than the distance between the source and substrate. Alamri's application of this formula is an approximation as the source temperature rather than an average temperature was used. Also the diameters of the atoms/molecules considered were only for Cd or Te_2. This would only be an accurate description if the gas had a homogeneous

composition. Models of the deposition process have also been suggested by Cruz-Campa and Zubia [8] and their work compared the growth rates for both the diffusion limited and the sublimation limited cases. Their simulation estimated the growth rate from which every case had the minimum growth rate.

The growth rate (G_R) for the diffusion limited case proposed by Cruz-Campa and Zubia consists of [8]:

$$G_R = \alpha F_{Cd} \frac{m_{CdTe}}{\rho_{CdTe} N_A} \tag{5-4}$$

$$F_{Cd} = \frac{D_{Cd}}{kt}\left(\frac{P^{Cd}_{sou}}{T_{sou}} - \frac{P^{Cd}_{sub}}{T_{sub}}\right) \tag{5-5}$$

Where m_{CdTe} is the molar mass of the CdTe, ρ_{CdTe} is the density of the CdTe, N_A is the Avogadro's number, α is a parameter which can be adjusted so that the model matches experimental data. F_{Cd} is the cadmium flux defined by equation 5-5, where t is the source substrate separation, D_{Cd} is the diffusion coefficient for Cd, T_{sou} and T_{sub} are the source and substrate temperatures respectively, P^{Cd}_{sou} and P^{Cd}_{sub} are the vapour pressures for Cd. For the sublimation limited case if it is assumed all of the atoms which arrive at the substrate form the layer, the net growth rate is given by [8][1]:

$$G_R = \frac{\alpha\beta(P^i_{sou}(T_{sou}) - P^i_{sub}(T_{sub}))N_A}{\sqrt{\pi m_i R T_{av}}}\left(\frac{m_{CdTe}}{\rho_{CdTe}}\right) \tag{5-6}$$

Where $P^i_{sou}(T_{sou})$ and $P^i_{sub}(T_{sub})$ are the vapour pressures for substance i (where i can be Cd or Te), R is the gas constant and T_{av} is the average temperature. Work by Mitchell *et al.* fitted the following expression for the growth rate to experimental data [9]:

$$G_R = G_{R0} exp - \left(\frac{\Delta E}{kT}\right) \tag{5-7}$$

Where G_{R0} is a constant and ΔE is the activation energy. Their worked showed using the source temperature as T, the expression fitted for a range of temperatures for deposition pressures of 1.33 mbar and 1013 mbar. From these fits they calculated the activation energies to be; 2.53 eV at 1.33 mbar and 1.82 eV at 1013 mbar.

The effect of varying certain deposition parameters on the growth rate has also been reported. Alamri showed two distinct growth rate regions when increasing the source substrate distance for a series of depositions [7]. This would indicate a change in the growth mechanism, presumably from a sublimation limited to diffusion limited case. The

[1]The equation has been corrected from the version printed in the paper

growth rate was found to be independent of the substrate temperature (over a 100 ℃ region), for temperatures substantially lower than source temperature and with a low deposition chamber pressure (10^{-5} mbar). This result does not appear to agree with the theory for a sublimation limited case suggested by Cruz-Campa and Zubia. No reason for this disagreement can be found from the experimental detail provided. As the distance between the source and substrate increased at low pressures, the growth rate was reported to decrease due to the divergence of the gas. Work by Nagayoshi and Suzuki observed that the deposition rate increased as the source temperature increased for a deposition under vacuum, in agreement with a sublimation limited case [10]. They also varied the substrate temperature and showed for a source temperature of 650 ℃ the growth rate was a maximum for a substrate temperature of 520 ℃. The occurrence of a maximum deposition rate for a series of experiments where only the substrate temperature was varied would imply varying this parameter changed the deposition mechanism. Work by Anthony *et al.* showed the composition of the environment gas also has an effect on the diffusion limited process. They proposed the faster growth rate in a helium environment compared to an argon was due to the small molecular weight and diameter of the helium [11].

5.3 Close space sublimation system

The deposition chamber built for this research consists of a horizontal quartz tube with two stainless steel end flanges. Two graphite blocks are positioned within the chamber to support a crucible containing the source material and a single sample. These blocks are heated through the quartz tube by infra red lamps positioned outside the chamber, see figure 5-1.

A pyrolytic boron nitride crucible (Almath Crucibles Ltd.) was used to hold the source material as boron nitride is chemically inert and has good thermal conductivity. The crucible has a diameter of 52 mm, it initially was 13 mm deep but this was reduced during the project to 4 mm so that less source material was required to fill it. The source material used during this work was 99.999% CdTe (Alfa Aesor, stock number 14367, -325 mesh (has particles that measure less than 44 μm in size)). During the whole of this project the distance between the deposition surface and the top of the crucible was 8 mm.

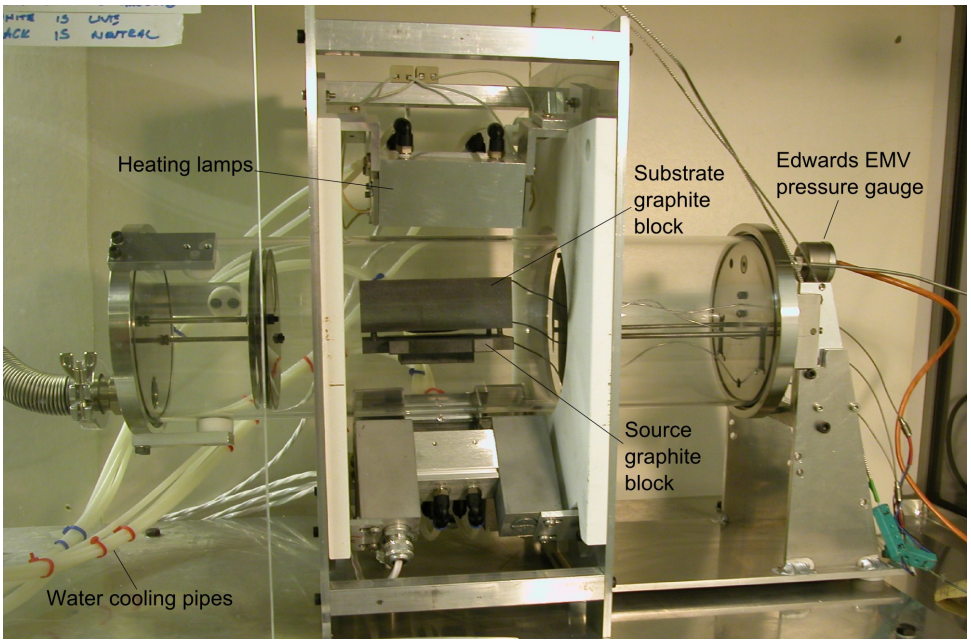

Figure 5-1: Photo of the CSS equipment used during this project.

However the source material was allowed to reduce in volume over several runs increasing the source substrate distance.

The crucible was positioned within a cylindrical hole in a graphite block, this block is referred to as the source graphite block. This block rested on the inside of the quartz tube supporting itself in the correct position. The substrate block was held above the source block on four graphite spacers (cylindrical graphite rods). The substrate graphite block had a rectangular hole cut through it, with a rim around the bottom on which a sample could be rested, see figure 5-2. The source blocked was; 120 mm long, 135 mm wide and weighed 276 g, and the substrate blocked was; 120 mm long, 80 mm wide and weighed 233 g. The large masses of the blocks meant that they would retain their temperatures better than lighter versions due to a larger thermal mass, enabling easier regulation of their separate temperatures. The disadvantage to this design was that the larger masses took longer to reach a set temperature, for the same input power.

The temperatures recorded for the substrate graphite block and the source graphite block were assumed to be the temperature of the substrate and the source material respectively. The source material crucible sat in a well where a good contact with the graphite block was made across the bottom of the crucible, and so the assumption of a good thermal equilibrium between the block and crucible seems reasonable.

The quartz tube had an external diameter of 148 mm with 4 mm thick walls and was

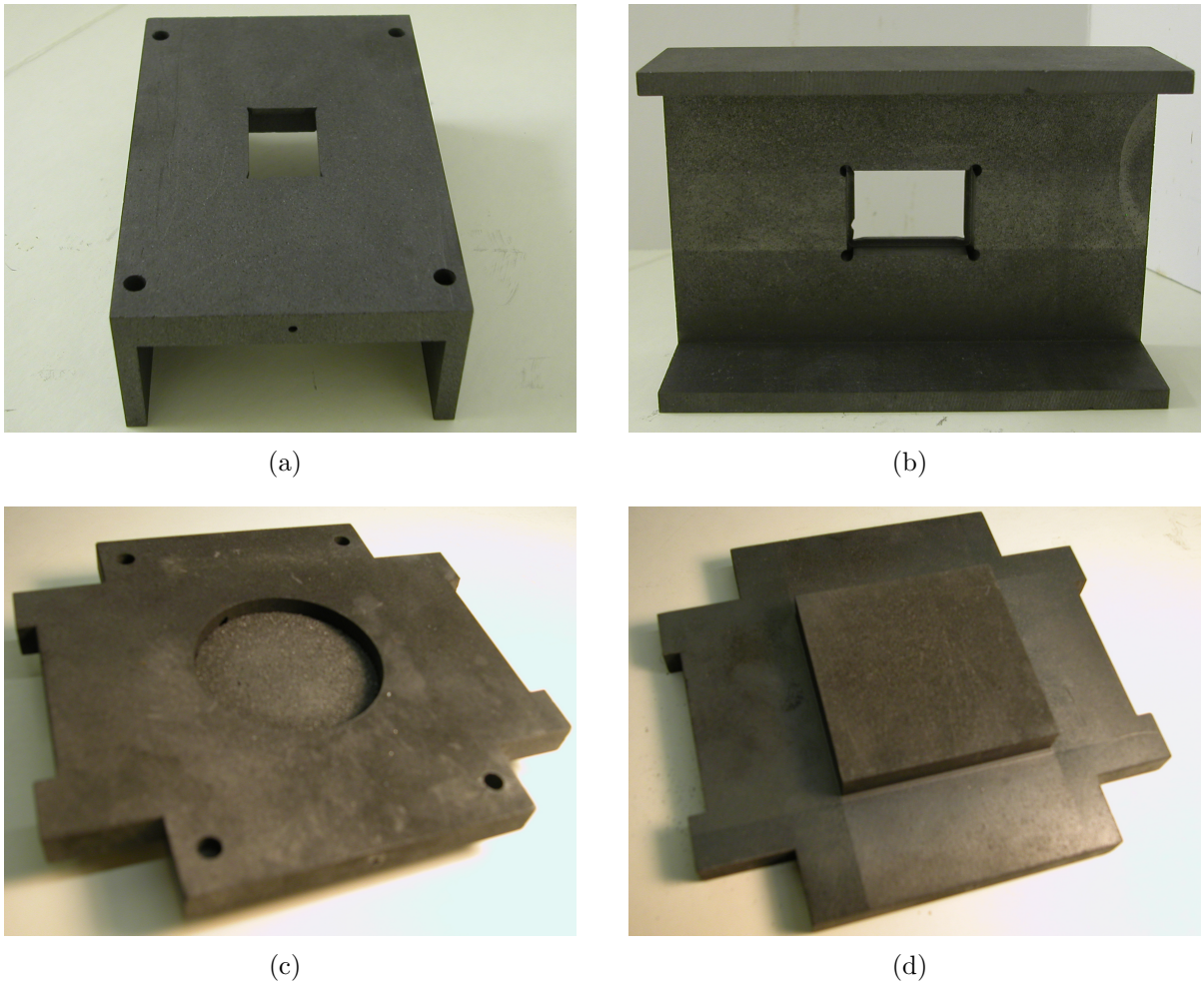

(a) (b)

(c) (d)

Figure 5-2: Photos of graphite blocks used for the ((a) and (b)) substrate and ((c) and (d)) source material.

500 mm long. Fluorocarbon O-rings (James Walker (FR10/80 139.3 mm DS 5.7 mm)) were located within circular grooves in the stainless steel flanges to enable a vacuum seal to be formed with the tube. Three feedthroughs were used to allow k-type thermocouples into the reaction chamber.

The heating of the chamber was supplied by five, 50.8 mm long (2 inch) 120 V, 1 kW infra red heating lamps (Q1H120 100R12 Ushio America inc.). The lamps were positioned outside the chamber with two lamps heating the substrate block and three heating the source block. The lamps have solid aluminium water cooled focusing mirrors which allow the infrared light to be directed onto the small areas on the graphite support blocks to enable more controlled heating, see figure 5.3(b).

Sets of four stainless steel discs were mounted approximately 120 mm from the inside

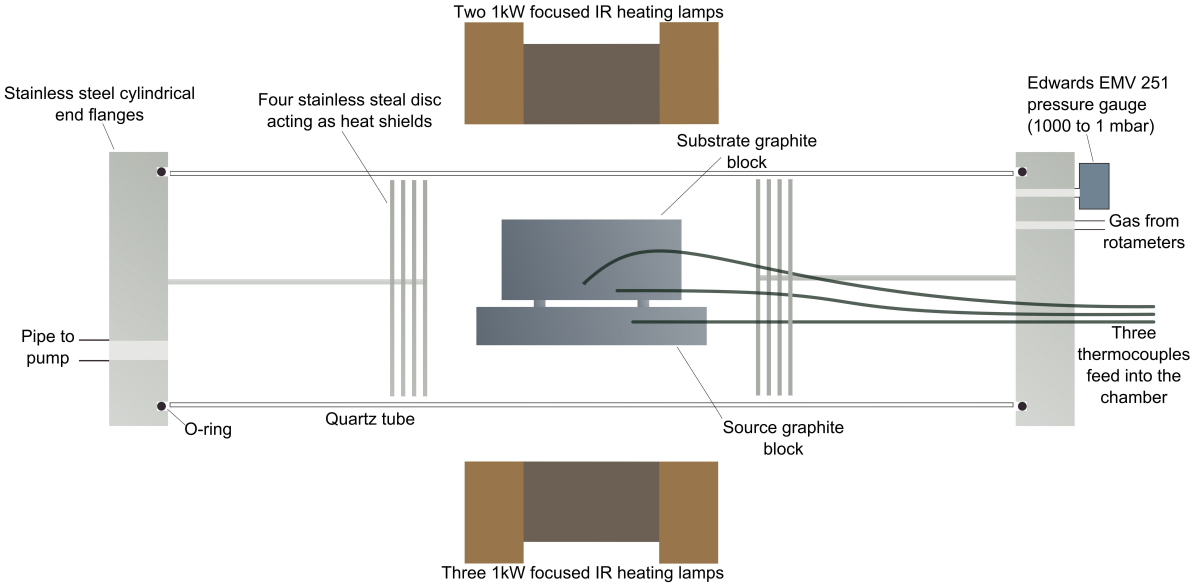

(a)

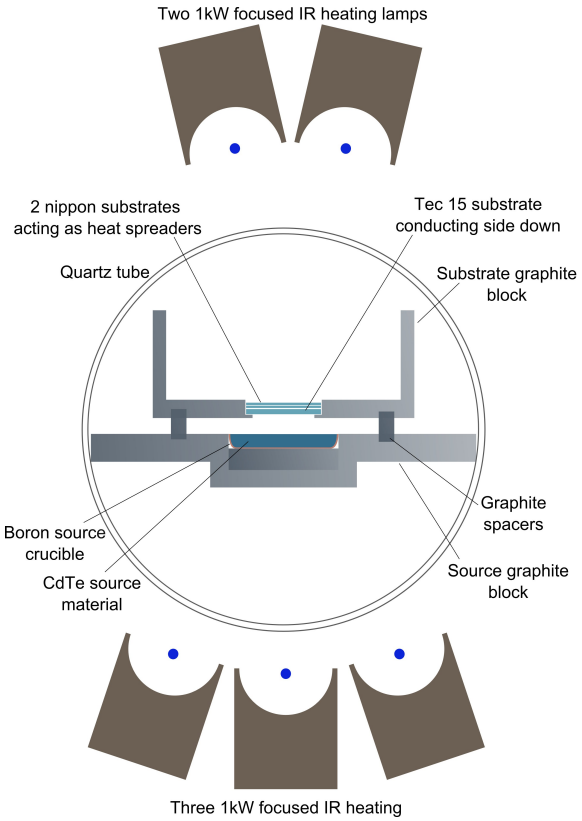

(b)

Figure 5-3: Schematic representations of the CSS equipment built for this research. The diagrams show (a) the geometry of the equipment and (b) a cross section through the middle of the two graphite blocks. The substrate rests on the rim of a rectangular hole in the top substrate block, while the crucible rests in a cylindrical hole in the source block.

of the steel flanges to act as 'heat shields'. These had two effects, firstly reducing the temperature of the end flanges, so that the components attached to them did not get too hot. Secondly, the heat shields reduced the amount of heat lost out of the chamber and so decreased the time it took to heat up the chamber.

The lamps are controlled as two sets (source and substrate) by proportional integral derivative (PID) controllers (Eurotherm 0216 and 0316). These controllers vary their output depending on the difference between a measured temperature of the block and a set point temperature. The controllers have a 'SMART' algorithm which adjusts the parameters of the controllers to improve the effectiveness of the control. For our equipment the two controllers were given an opportunity to 'test heat' the system (heat without any source material or a substrate being present) every time the set points were changed to enable them to 'learn' the best way to adjust the controllers.

The chamber had a rotary vacuum pump (Pfeiffer DUO 016 B (16 m^3/h)) attached to one flange (via a 2000 mm long pipe) with the option to allow gas to flow into the other flange. The flow rate through the pump had to be reduced so that the flow of gas going into the chamber was of the order of one litre/minute. To control the pumping rate a valve was positioned between the pump and deposition chamber, a pipe which bypassed the valve had a smaller diameter to restrict the flow of gas. The pressure in the chamber was measured by two gauges; the first was an Edwards EMV 251 absolute capacitance gauge located on the end flange with the gas inlet, see figure 5.3(a). This gauge had a working range from 1 mbar to atmospheric pressure. The second gauge an Edwards AGD Pirani gauge was located 600 mm away from the chamber down the pipe to the pump. This gauge measured pressures over the range of 10 mbar to 1×10^{-3} mbar. With no gas flowing into the chamber the pump could draw a vacuum of 2×10^{-2} mbar.

Each graphite block had a hole in which a thermocouple could be placed. These thermocouples were connected to the controller which controlled the lamps which heated the respective block. The thermocouples were also connected to the computer using a Measurement Computing USB device (USB-TC) and its associated software (InstaCal and TracerDAQ). This software allowed the temperature of the thermocouples to be recorded against time so a temperature profile for each deposition could be collected. The temperatures were recorded every 10 seconds.

Argon and oxygen gases were connected to the system. The argon gas was used as

an inert gas and was controlled via a 0.2 to 2.0 l/min rotameter (1100 Mobrey). The oxygen cylinder was connected by a 0.1 to 0.7 l/min rotameter (1100 Mobrey). The two gases were brought together in a tee-piece and then passed into the chamber. The use of a tee-piece meant that the flows of the gases were dependent on each other and so a stabilisation period was required each time the gas flows were adjusted.

During the development of the equipment the introduction of flexible insulation (calcium-magnesium silicate) around the quartz reaction tube was found to reduce the time needed to heat up the graphite blocks, but it also reduced both the cooling rate, and the temperature difference between the graphite blocks. Therefore no additional insulation was used in the equipment. Some aspects of the design were modified after initial tests. Insulated board (calcium silicate) was used to support the quartz tube loosely after early test showed that the boards were susceptible to cracking under thermal stress. Also the thickness of the quartz tube was increased from 2 to 4 mm after the ends of the thinner quartz tubes cracked during the initial runs. Another aspect of the design which was changed early on was the source graphite block was originally supported by two quartz bars, but these were found to slow the heating rate, and so were removed.

5.4 Deposition procedure

Normally the deposition chamber was left under vacuum between runs. When it was necessary to open the chamber, gas was fed inside to bring the pressure up to atmosphere. The end flange with the gas inlet would be removed and the graphite blocks would be removed from the chamber. To monitor changes in the source material the crucible was weighed in between depositions and the relative height of the source material compared to the top surface of the crucible was recorded using a Vernier height gauge (Sylvac). The sample was placed in the substrate block and two glass samples were placed on top acting as heat spreaders (details given in 5.6). The graphite blocks were then placed in the end of the tube and the thermocouples were positioned within the blocks. The blocks were then pushed into the centre of the quartz tube and the chamber was pumped to a vacuum. After a vacuum had been achieved the gas rotameters could then be adjusted to obtain the desired environment within the chamber. When the environment was stabilised the heating sequence was started and the temperature monitoring began. The CSS deposition

parameters used to deposit CdTe through out this project, unless stated otherwise, were:

- source temperature 650 ℃,
- substrate set point 500 ℃,
- source substrate separation 8 mm,
- deposition time 30 min (with additional 10 min warm up),
- 7 mbar argon environment (2.0 l/min).

After the heating sequence was completed the deposition equipment was left for a few hours to allow the graphite blocks to cool under the same environmental conditions.

5.5 Temperature profiles

In this experimental system the starting point of a deposition could not be controlled by using a shutter, so an alternative method had to be devised. The parameters which can be adjusted during a run to affect the deposition process are; the temperature of the source and substrate graphite blocks and the pressure of the chamber. Other research groups have equipment which does not include a shutter, and they have controlled the deposition through the heating sequence of the source and substrate [10, 12]. Similar controls have been used in the current work and an example of the heating profiles can be seen in figure 5-4. Throughout this work the substrate lamps were turned on ten minutes before the source lamps. This allowed the substrate block to reach an elevated temperature which would stop any deposition during the initial heating of the source material. Ten minutes was chosen as it allowed the substrate block to reach a temperature close to its designated set point, before the source material was directly heated. This ensured any deposited material would form at temperatures close to those prescribed by the controller set points. It can be seen in figure 5-4 that the source material's temperature increases as the substrate block is heated, this highlights the fact that the temperature of the two blocks are dependent on each other. The profiles also show that the temperature difference between the source and substrate blocks decreases rapidly when the lamps are turned off (40 minutes after the substrate lamps were turned on)

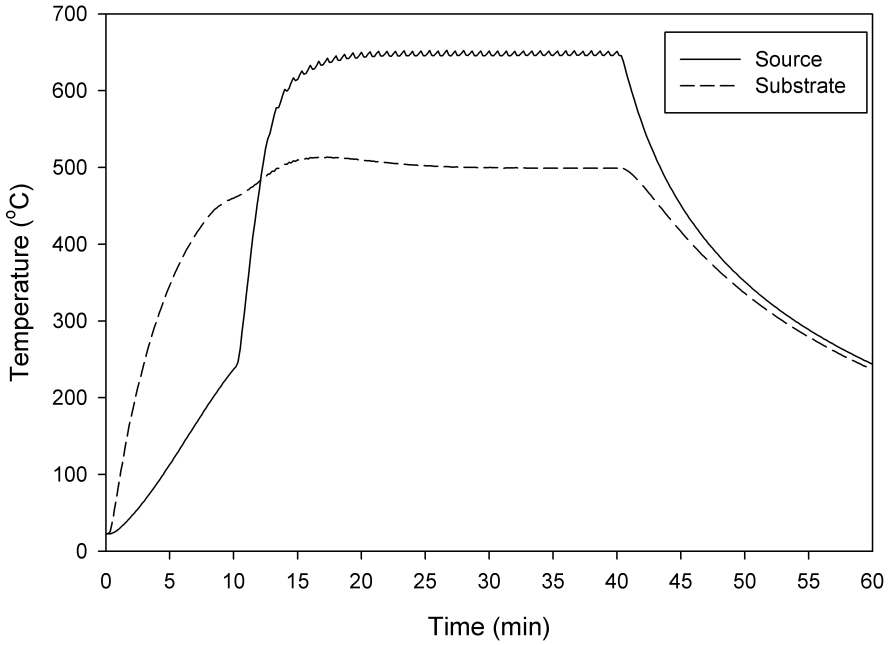

Figure 5-4: A typical heating profile of the source and substrate graphite block during a deposition run. In this example the source was set to 650 ℃, and the substrate was set to 500 ℃. The oscillation in the temperature profile of the source material is caused by the controller operating the lamps.

A series of samples were deposited to observe at what point in the heating profiles the deposition was initiated. The substrate lamps were turned on for 10 min before the source lamps were turned on. The 'deposition time' was defined as the amount of time the source lamps were on. Deposition times of 0, 3, 5, 6, 6.5, 7, and 7.5 min were investigated. The substrate heating profiles for some of the deposition times can be seen in figure 5-5. No material was observed on the surface of the CdS for deposition times of 0 to 6 min. A thin layer of CdTe was observed for the 6.5 min deposition and thicker layers of material were observed for the longer deposition times. This demonstrates that no deposition occurs before the graphite blocks have reached their set point temperatures. It was assumed that this would be valid for all operating temperatures.

5.6 Heat spreaders

When a sample is mounted in the substrate graphite block, it simply rests on the rim of a window within the block. When first setting up the equipment, a small graphite block

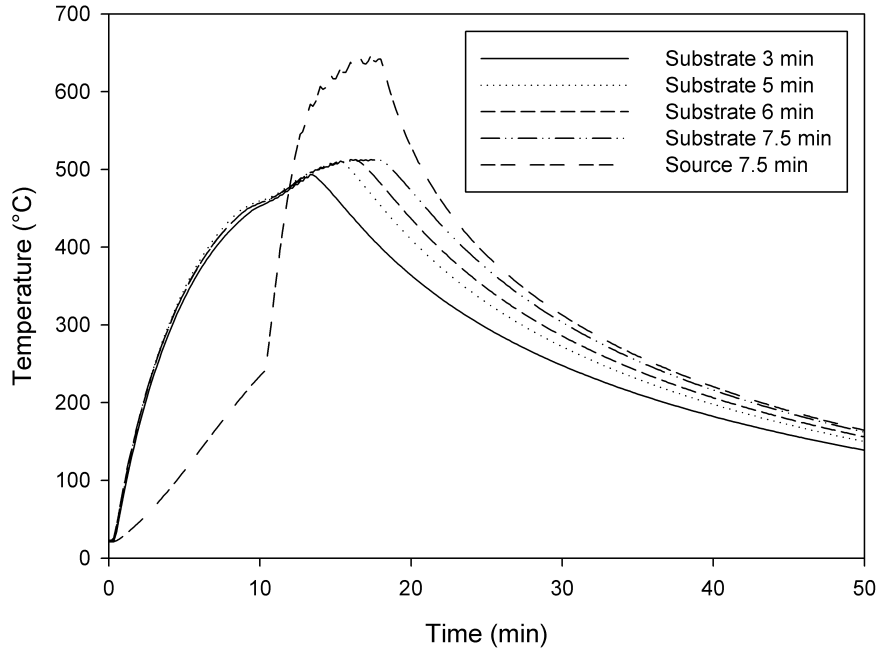

Figure 5-5: The substrate heating profiles for deposition runs with a range of deposition times. The source heating profile for the 7.5 min deposition is also shown.

was placed on top of the sample when it was mounted, in an attempt to try to ensure that the substrate and substrate block were at the same temperatures. A third thermocouple, within the chamber, showed the small block became 10 ℃ hotter than the main substrate block. However the uniformity of the material deposited on the substrate was found to be poor. The effect could be reproduced by simply stopping the light from illuminating the sample directly. It was therefore concluded that poor thermal contact was being made between the small graphite block and the substrate, as no heat was apparently being transferred.

Durham University use additional glass substrates resting on the back surface of the sample during their depositions [2]. A similar approach was attempted in this study. Two thin glass substrates were used as 'heat spreaders', and were rested on top of each other on the top surface of the sample. The uniformity of the deposited material was found to be better than that previously observed with the small graphite block in place.

One sample underwent a deposition with two stacked heat spreaders placed over one-half of the top surface of the sample. The material deposited on the bottom surface

[2]private communication with Y. Proskuryakov

corresponding to the uncovered half, had a better uniformity than the half with the two heat spreaders on top. However, deposition with higher substrate temperatures showed better uniformity was achieved with the presence of heat spreaders covering the full sample surface. This is believed to indicate that the heat spreaders cause the temperature of the sample to be higher and closer to the temperature of the substrate block. Subsequently, the two glass heat spreaders positioned on the back surface of the sample, were used in all other CSS depositions reported here.

5.7 Source material

The source material was not changed after every run, so the volume of the material decreased with each deposition. CdTe was deposited on the inside of the equipment in regions where the chamber is cooler than the graphite blocks. This means that more than just the amount of CdTe deposited on the sample is removed from the source material during each run.

The measurements of the height of the source material used here were not accurate enough to monitor the changes between runs. SEM images of source material which had been used in several depositions showed a porous structure. Energy dispersive X-ray (EDX) spectroscopy measurements of the same used source material indicated it had become Cd rich. In comparison EDX measurements showed new source material to be stoichiometric within a experimental uncertainties in atomic fraction of $\pm\,0.01$ when using the internal calibration.

The change in the weight of the source crucible for a given deposition against the thickness of the films deposited can be seen in figure 5-6. The results show a consistency in the amount of material lost from the crucible and thickness of the deposited films for a particular pressure with the different pressures affecting the transport of CdTe onto the substrate.

5.8 Deposition pressures

A range of deposition times and pressures were used to deposit CdTe on to 8 Tec 15 glass substrates. The samples were deposited to determine if a change in the stoichiometry of

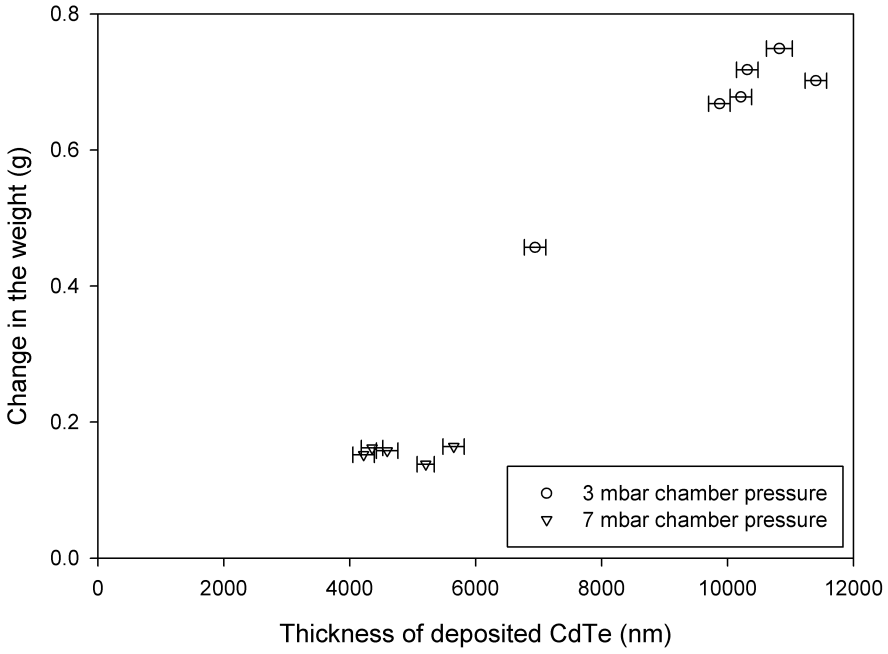

Figure 5-6: The thicknesses of deposited films measured by Rutherford backscattering spectroscopy against the change in the weight of the CdTe source material. The samples are the samples used in the CdS bilayer study in chapter 7.

the deposited material is seen with different deposition pressures. Monte Carlo simulations by Romeo *et al.* modelled the diffusion of Cd and Te_2 gases between the source and substrate, and suggested an excess of Te atoms reached the substrate in the diffusion limited process [13]. This was explained by the larger mass of the Te_2 molecule compared with the Cd atoms, resulting in more scattering of the Cd gas by the inert Ar atoms within the environment. The fraction of tellurium excess (Te_{ex}) was calculated using the equation 5-8 [13].

$$Te_{ex} = \frac{Te_{atsub} - Cd_{atsub}}{Te_{atsub}} \tag{5-8}$$

Where Te_{atsub} and Cd_{atsub} are the amount of Te and Cd respectively, which reaches the substrate.

The gas flow rates of the depositions were varied to allow the pressures measured within the chamber to vary from 0.02 to 50 mbar. The deposition parameters can be seen in table 5-1. The chamber reaches a pressure of 7 mbar with a gas flow of 2.0 l/min, with the normal restrictions in place between the chamber and the pump. Two approaches were used to increase the pressure within the chamber above 7 mbar. Firstly the flow of

gas was increased above the 2.0 l/min, which meant that the flow of gas was off the scale on the rotameter and was therefore adjusted using the value of the resulting pressure. Secondly further restrictions were put in place by adjusting a second valve positioned on the pipe connecting the chamber to the pump. This second valve was not adjusted in the standard method due to the lack of reproducibility in the restrictions imposed by this valve.

The deposition of CdTe directly onto Tec 15 glass results in a layer with poorer uniformity than corresponding material deposited on a CdS layer. This suggests that the CdS effects the nucleation of the CdTe deposited by CSS. The influence of the substrate has been observed by other groups, with a single zincblende phase of CdTe reported for material deposited on CdS, compared to a mixed phase of CdTe reported for material deposited directly onto the TCO [9].

The composition of the films deposited on TCO was determined by EDX measurements, using the internal calibration. Attention was placed on checking the absence of the main Si peak, see figure 5-7. This was in order to check the thickness of the CdTe being measured was large enough to prevent the Sn peaks from the TCO distorting the peaks from the Cd and Te. In this work, unused source material was measured and the measured atomic composition was found to be accurate to within ± 0.01 (Cd 0.507 and Te 0.493 atomic fraction), whilst measurements of HgTe and PbTe standard materials

Table 5-1: The deposition parameters for a 8 samples deposited under different pressures and the thickness of the deposited film.

deposition pressure (mbar)	**Ar Gas flow (l/min)**	**deposition time (min)**	**were additional restrictions used on the flow of gas to the pump**	**thickness of film measured by alpha step (μm)**	**change in the weight of the crucible (g)**
0.02	0	45	no	29	0.18
0.2	0.2	45	no	19	0.47
1	1.0	30	no	7.9	0.16
1	0.25	60	yes	20	0.38
10	< 2.0	60	no	6.0	0.11
10	0.65	60	yes	4.8	0.10
54	< 2.0	90	no	3.6	0.04
51	1.0	60	yes	2.0	0.03

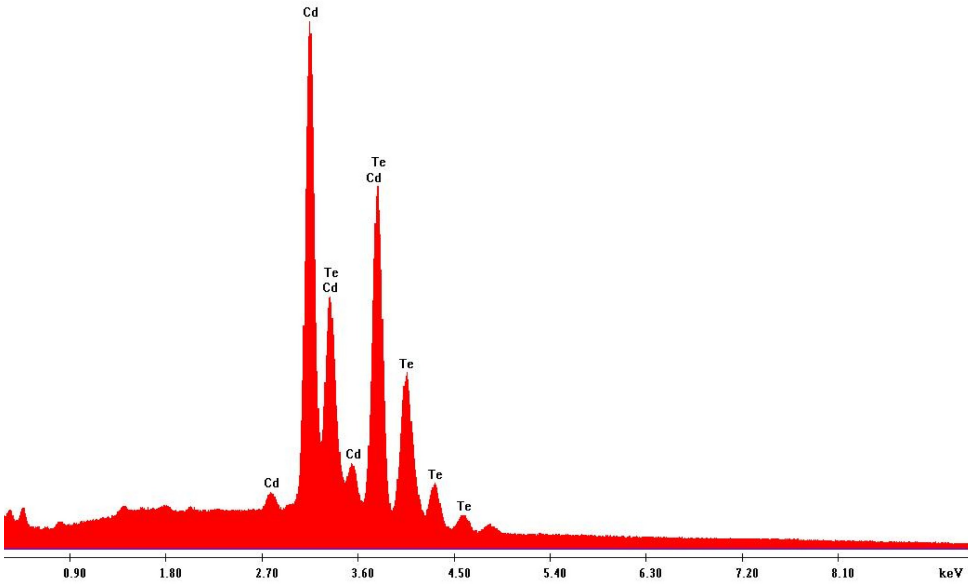

Figure 5-7: EDX spectrum collected for CdTe deposited on TCO by CSS at a pressure of 1 mbar.

were shown to be accurate within ± 0.04 of the atomic fraction. Based on the errors of these known materials an experimental uncertainty of ± 0.04 in the atomic fraction was used for the measurements of the materials with an unknown composition. It should be noted that this figure was obtained for bulk material with a smooth surface topography. Additional errors due to surface roughness and film thickness are not included in this error value, however the other sources of errors would affect these samples. To calculate the error in the tellurium excess the ± 0.04 atomic fraction error within each of the Cd and Te measured composition fractions are propogated through the excess calculation. The error in the tellurium excess values was calculated to be approximately ± 0.014 in the excess, which corresponds to a 15 to 25 % error in the tellurium excess values.

Work by Romeo *et al.* predicted an approximate 0.11 excess of tellurium at the substrate, for a 8 mm source substrate separation, in a 1 mbar argon environment [14]. The samples deposited here, however show a Te deficiency, see figure 5-8. The samples appear to show an increase in the fraction of tellurium within the samples with increasing pressure. This would agree with the theory suggested by Romeo *et al.*. The source material used during these depositions was also analysed with EDX. The top and bottom surface of the sintered material appeared to have a porous structure (see figure 5-9) and was tellurium deficient, 0.43 ± 0.04 atomic fraction of tellurium (this would equal -0.31 of tellurium excess). This allows the proposed theory by Romeo *et al.* to relate to these

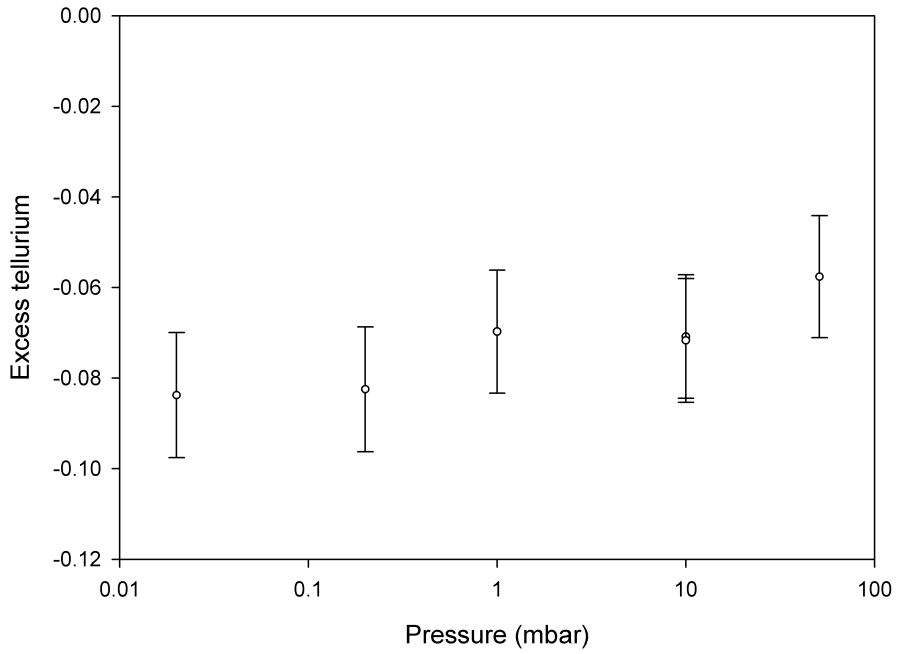

Figure 5-8: The excess tellurium for CdTe deposited on TCO by CSS with a range of deposition pressures. A ± 0.014 error in the excess was calculated.

samples, with the atomic fraction of tellurium included in the samples being greater then the amounts present in the source material. It was noted that changes in the layer thickness and surface topography would affect the errors reported in this result but no assessment of the size of these effects was determined.

Scanning electron microscopy (SEM) images of the top surface of the CdTe deposited on the TCO with different pressures were collected, see figure 5-10. The images indicate that with increasing pressure the features on the surface increase in size. Alpha step measurements showed the thickness of the films decreased with increasing deposition pressure, indicating a slower growth rate, see table 5-1. It can be deduced from these images that the features on the surface have larger facets with increasing pressure. The difference in the thickness of the deposited films needs to be considered as a possible explanation for the difference in the morphology. Also a possible explanation may be found through considering the slower growth rate of the material deposited with higher pressure. The deposition observed for the samples deposited at 50 mbar is in agreement with work by Major *et al.*, they observed the nucleation of CdTe deposited under higher pressure by an island mechanism [15].

The difference in the morphology was small for material deposited at the same pressure

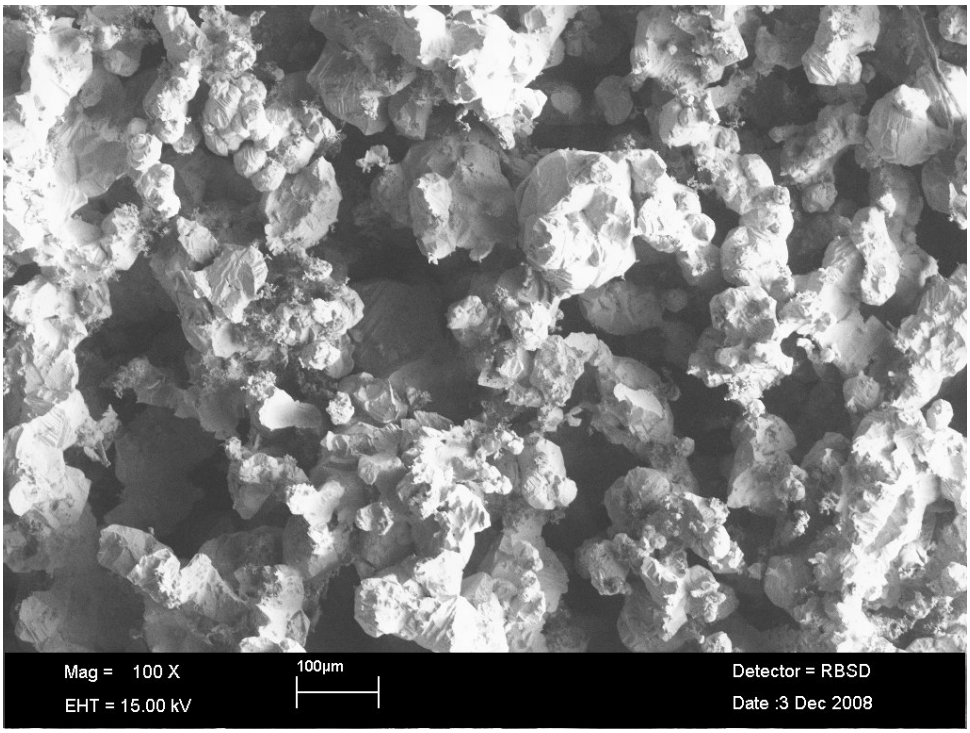

Figure 5-9: A SEM image of the top surface of sintered source material which has been used for several depositions. The porous structure of the material can be seen. Scale bar represents 100 µm.

with or without the additional restrictions on the flow of gas to the pump. The clearest difference can be seen for the material deposited under 50 mbar of pressure. The material deposited with the restriction to the flow (not shown) had a higher density of grains on the surface of the substrate compared to the material deposited with the higher gas flow rate (figure 5-10(d)). This may indicate that the nucleation of the CdTe is effected by the flow of the gas at high pressures.

The deposited material was also examined by XRD measurements, an example of the diffractograms can be seen in figure 5-11, and the texture coefficient was calculated for 11 peaks, see figure 5-12. The figure shows a decrease in the amount of (111) preferred orientation as the pressure increases from 0.02 to 1 mbar. Large amounts of preferred orientation in the films deposited under low pressures may be explained by considering the (111) planes grow fastest of all the planes in vapour growth experiments [16]. For a fast deposition rate this direction would dominate over slower directions. The errors displayed on the figure are the errors associated with the texture coefficient calculation for each sample. The limited number of samples does not demonstrate the possible variation in the coefficient values between different samples deposited under the same conditions.

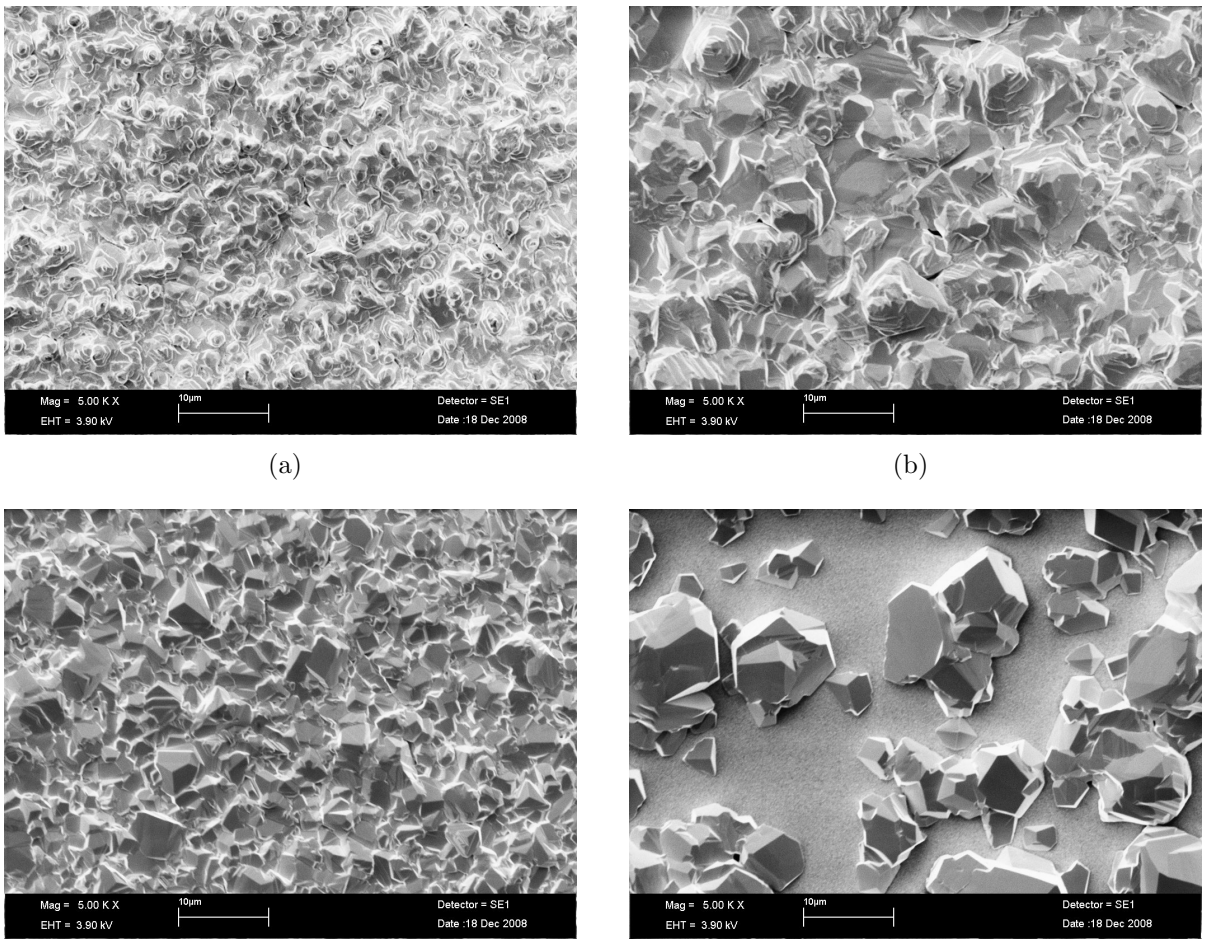

Figure 5-10: SEM images of CdTe deposited under different pressure: (a) 0.02 mbar of pressure, (b) 1 mbar pressure with additional restriction on the gas flow, (c) 10 mbar pressure with additional restriction on the gas flow and (d) 50 mbar pressure. Scale bar represents 10 µm.

Without knowing the expected variation in the values of the coefficient between comparative samples, it is unclear if the samples deposited with the restricted gas flow have a higher texture coefficient compared to the material deposited without the additional restrictions on the gas flow. There is currently no explanation of the possible variation between samples deposited with, and without, additional restrictions.

The lattice parameter was calculated from Taylor Nelson plots, see figure 5-13, and for the different samples had an average value of 0.6490 ± 0.0004 nm. The scatter within the data suggested that the lattice parameter is independent of the deposition pressure.

Linear regression fits to Williamson Hall plots of the XRD data suggests a decrease in the amount of strain within the material with increasing pressure, see figure 5-14.

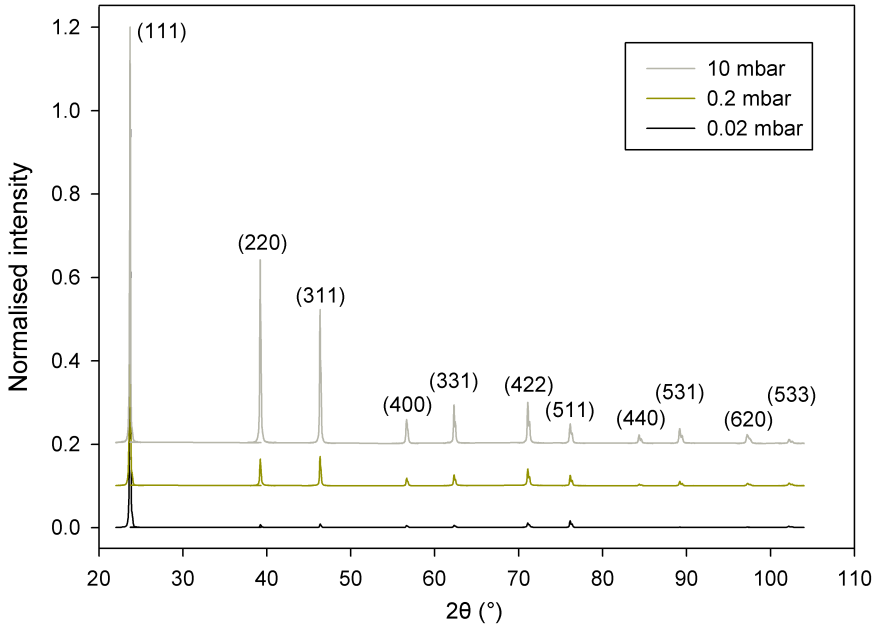

Figure 5-11: An example of CdTe diffractograms for material deposited under different pressures. The diffractograms have been normalised and offset for clarity.

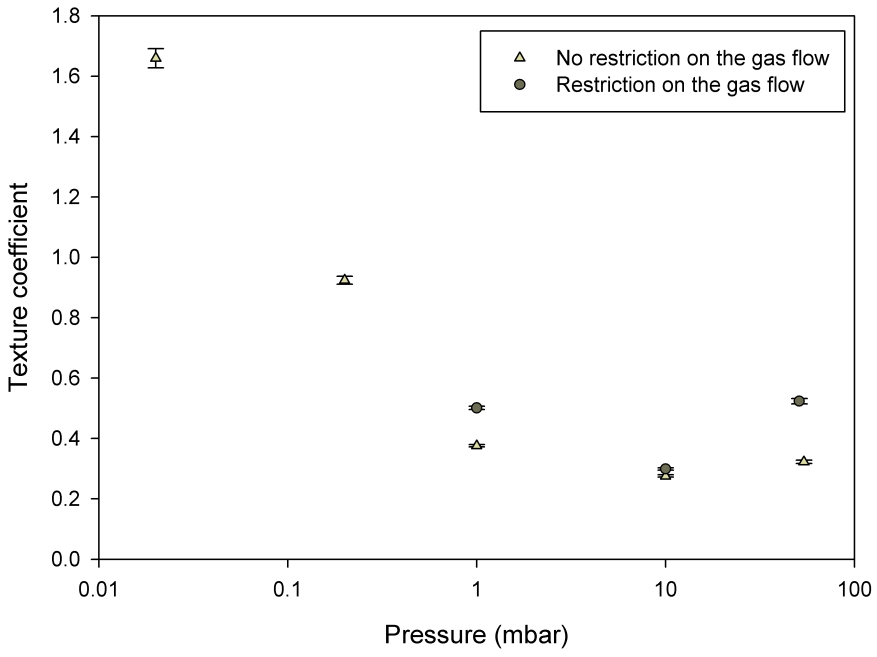

Figure 5-12: The variation in the texture coefficient for 11 peaks with different pressures. A value for the texture coefficient equal to 0 would mean the intensities have a random orientation and a value of 3.2 for 11 peaks would indicate the CdTe is perfectly oriented along one direction.

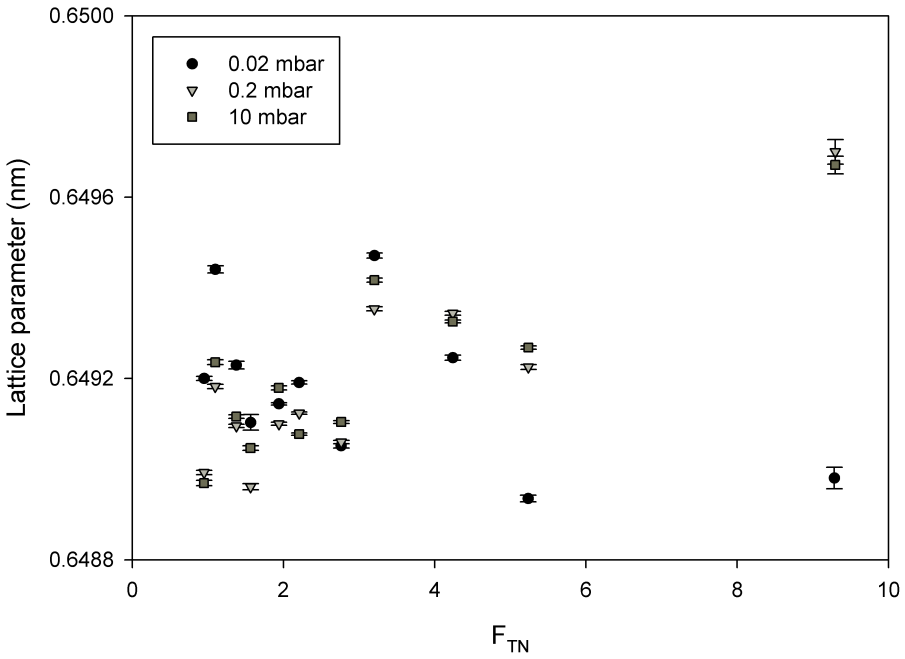

Figure 5-13: An example of a Taylor Nelson plot for CdTe material deposited under different pressures.

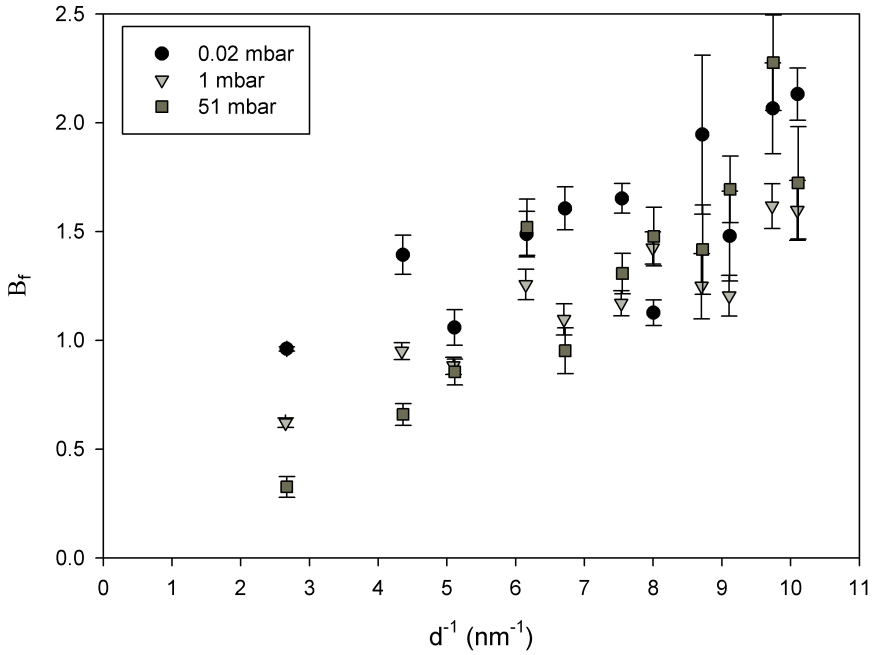

Figure 5-14: Williamson hall plot of three samples deposited under different pressures.

The linear fit to the data for the material deposited with 0.02 mbar suggest a non zero intercept which implies there is a crystallite size broadening contribution to the material. The Williamson Hall plots also allows for the presents of a possible {hkl} dependence and for it to change with different deposition pressures. The sample deposited with a pressure of 0.02 mbar appear to have less strain in the peaks with a d^{-1} value of 5.12 nm^{-1} for (311(crystallographic direction)), 8.02 nm^{-1} for (511) and 9.13 nm^{-1} for (531). The samples deposited with a pressure of 1 mbar do not seem to have an {hkl} variation, all of the peak values fit equally well to a linear regression fit. The material deposited at 51 mbar appears to have a different hkl dependence compared with the material deposited with a low pressure, an increase in the strain is seen in the peaks with a d^{-1} value equal to 6.17 nm^{-1} (400) and 9.76 nm^{-1} (620).

5.9 Substrate temperatures and environment compositions

A series of samples were deposited to demonstrate the effect of the substrate temperature and the composition of the environment on the deposited material. CdTe was deposited on CdS/TCO substrates. The average thickness of the CdS was 235 ± 20 nm. To show the effect of temperature four samples were deposited, with the controller for the substrate lamps adjusted so each run had a different set point temperature. The set point temperatures used were: 400, 500, 550 ℃ and a fourth run was carried out with no substrate lamp heating. For each change of the set point the two controllers were given an opportunity to 'test heat' the system, heating without any source material or substrate present, to enable them to 'learn' the best way to adjust the controllers.

For the samples deposited with the substrate set point of 400 and 500 ℃ the substrate lamps were heated for 10 minutes before the source lamps were turned on, see figure 5-15. An error occurred for the deposition with the set point equal to 550 ℃ causing the time between the substrate and source lamps being switched on to be 15 minutes. For the sample deposited without substrate heating the time was started when the source lamps were turned on. A maximum temperature of 490 ℃ was recorded by the substrate thermocouple for both the sample with a 400 ℃ set point and without any substrate heating. This shows a limitation of the equipment in terms of trying to achieve a substrate

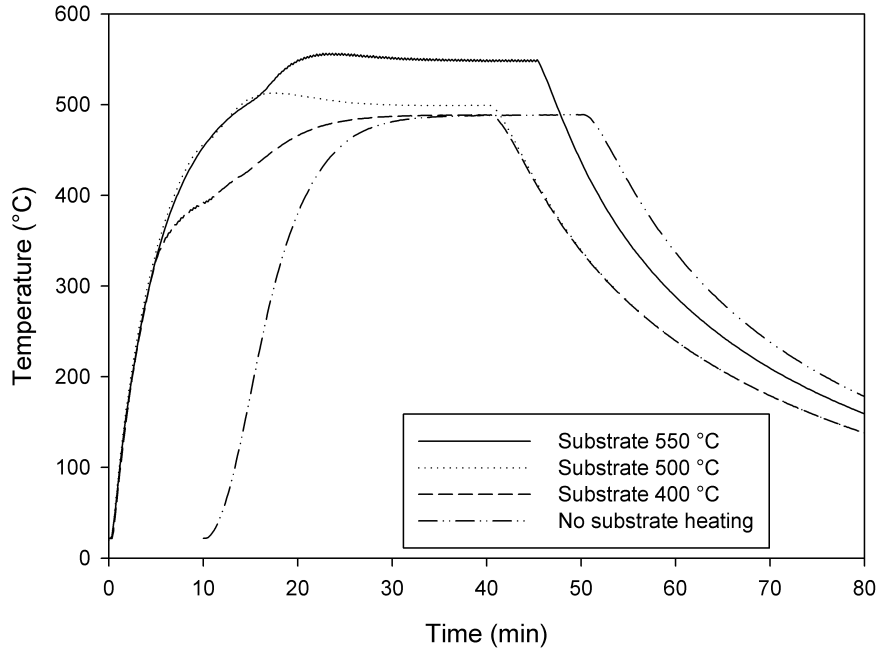

Figure 5-15: The temperature profiles for the thermocouple position within the substrate graphite block, for a range of controller set points.

temperature below 490 ℃ (for a source temperature 650 ℃ and for a 30 min deposition). Increasing the source substrate distance may provide a way of reducing the thermal coupling between the source and substrate, and hence increase the temperature difference between them.

SEM images of the deposited films (see figure 5-16) show the material deposited on the substrates at lower temperatures had smaller features. The difference in the samples which reached 490 ℃ and the sample heated at 500 ℃ is larger then would be expected if the temperatures were constant. However the temperatures of the substrates when the deposition is thought to have started were significantly different. The temperature of the substrate block when the source first reached 650 ℃; was 441 ℃ for the samples with no substrate heating, was 471 ℃ for the sample with the 400 ℃ set point and was 510 ℃ for the sample with the 500 ℃ set point. This suggests that the lower temperature of the substrate when the CdTe started to form caused the observed difference in the deposited material. The sample with the 550 ℃ substrate temperature (see figure 5-16(d)) does not appear to have larger features than the sample deposited at 500 ℃, but there appears to be facets with more well defined edges.

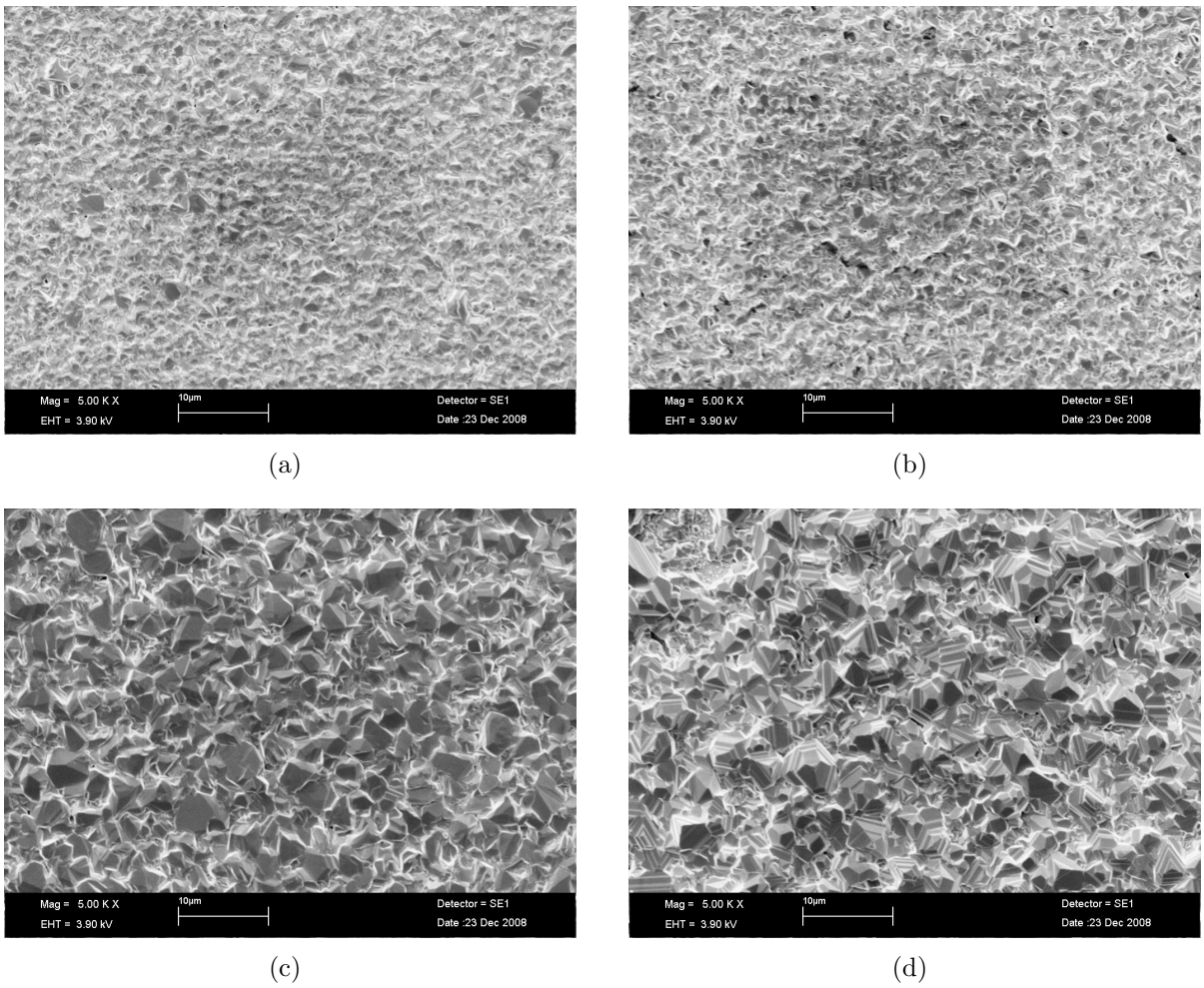

Figure 5-16: SEM images of the back surface of CdTe material deposited with different set point temperatures for the controller of the substrate lamps: (a) no substrate heating, (b) 400 ℃, (c) 500 ℃ and (d) 550 ℃. Scale bar represents 10 μm.

CdTe was also deposited in environments with different compositions and SEM images of the deposited films were taken. Argon and oxygen gas could be set to flow into the chamber either separately or at the same time. The deposition parameters of the samples can be seen in table 5-2 and SEM images of the surfaces can be seen in figure 5-17. The sample deposited in an oxygen environment appears to have smaller features on the surface compared to the sample deposited in an argon environment. The presence of oxygen within the chamber has been linked with an increase in the nucleation density of the CdTe [17]. This leads to a decrease in the grain size of the material which would be in agreement with what is observed here. The sample deposited with the mixed environment had facets with more pronounced geometric shapes. The sample deposited with Ar 1.8 and O_2 0.2 l/min was from the roughened TCO study discussed later, it is assumed the

Table 5-2: Deposition parameters for samples deposited in different environments.

Gas composition	**Pressure (mbar)**	**Deposition time (min)**	**SEM image figure 5-17**
O_2 0.3 l/min	0.2	14	(a)
Ar 0.3 l/min	0.2	14	(b)
O_2 0.3 l/min (no restriction)	0.3	30	(c)
Ar 1.8 and O_2 0.2 l/min	8	30	(d)

roughening of the TCO did not have an effect on the morphology of the sample due to the layer thickness and comparing it with other roughened samples.

5.10 CdTe deposited at Durham University

To allow a comparison of the CdTe deposited by the equipment developed in this work to that from another laboratory, Mohammed Alturkestani from Durham University deposited three samples of CdTe, on CdS deposited in the current work. The CdS was deposited by CBD with an approximate thickness of 147 nm. The Durham device fabrication procedure involved annealing the CdS in the CdTe chamber before the deposition. The CdS was annealed for 4 min at 400 ℃ in a hydrogen environment. The CSS deposition parameters used by Mohammed to deposit the CdTe were:

- a source temperature of 600 ℃,
- a substrate temperature of 500 to 530 ℃,
- source substrate spacing of 8 mm,
- 1.33 mbar pure oxygen environment (30 ml/min),
- deposition time of 6 min.

The Durham CSS deposition system includes a shutter between the source and substrate, this allows them to have more control over the start and finish point of the reaction.

The CdTe material was examined by XRD with a resolution of 0.005 ° 2θ and the reflections were fitted with single pseudo voigt functions. The texture coefficient was calculated and averaged to be 0.85 ± 0.1. Two of the samples had averaged lattice parameter

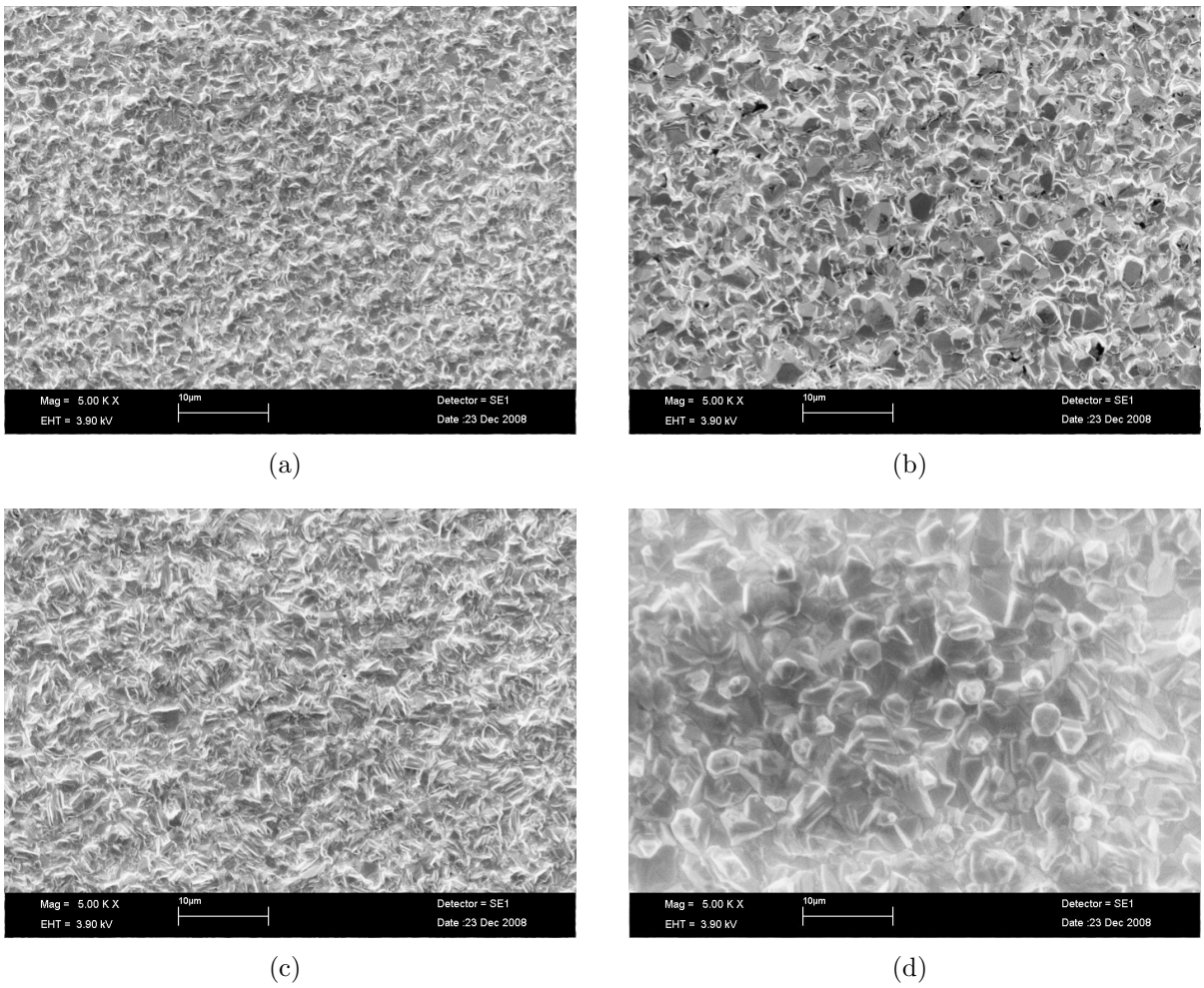

Figure 5-17: SEM images of the back surface of CdTe deposited with different environments; (a) 14.5 min deposition with 0.3 l/min oxygen, (b) 14.5 min deposition with 0.3 l/min argon, (c) 30 min deposition 0.3 mbar with oxygen and (d) 30 min deposition with 0.2 l/min oxygen and 1.8 l/min argon. Scale bar represents 10 μm.

0.6496 ± 0.0001 nm. The Williamson Hall plot of these two samples showed them to have a small amount of strain with a very small crystallite size contribution, see figure 5-18. A third sample labelled Durham 2 has a lattice parameter of 0.6493 ± 0.0001 nm. The Williamson Hall plot of the data for this sample indicates the material had a {hkl} dependence. The majority of the peaks showed the presence of a crystallite size contribution. While three peaks ((111), (511) and (531) (d^{-1} values of 2.5, 8.0 and 9.0)) had a similar amount of strain to the other two samples. SEM images of the surface of the Durham CdTe (see figure 5-19) showed continuous films without any geometrically shaped facets.

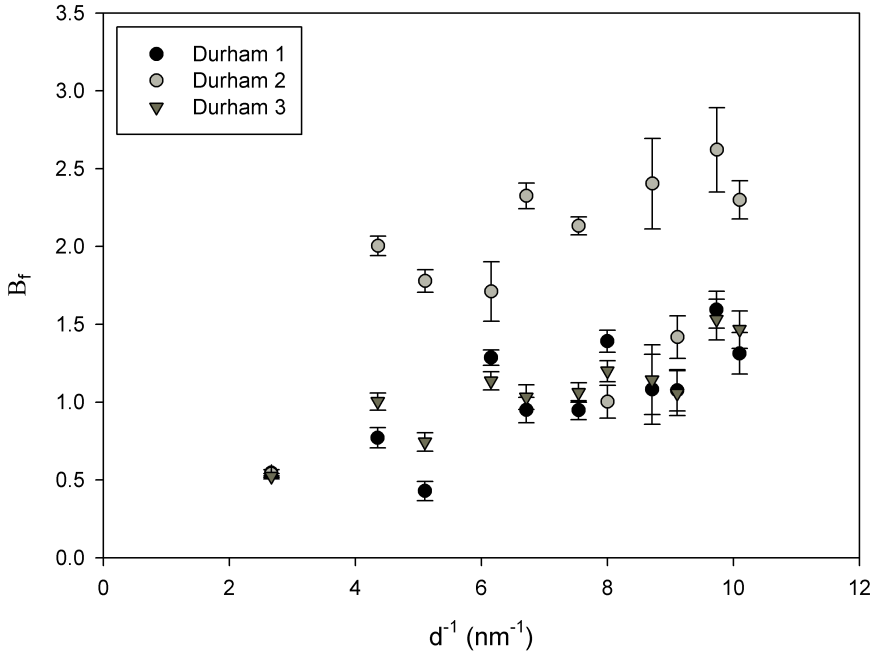

Figure 5-18: Williamson Hall plot of three samples of CdTe deposited at Durham University. The 2nd Durham sample appears to have a peak broadening component due to the finite crystallite size for 8 of the 11 peaks.

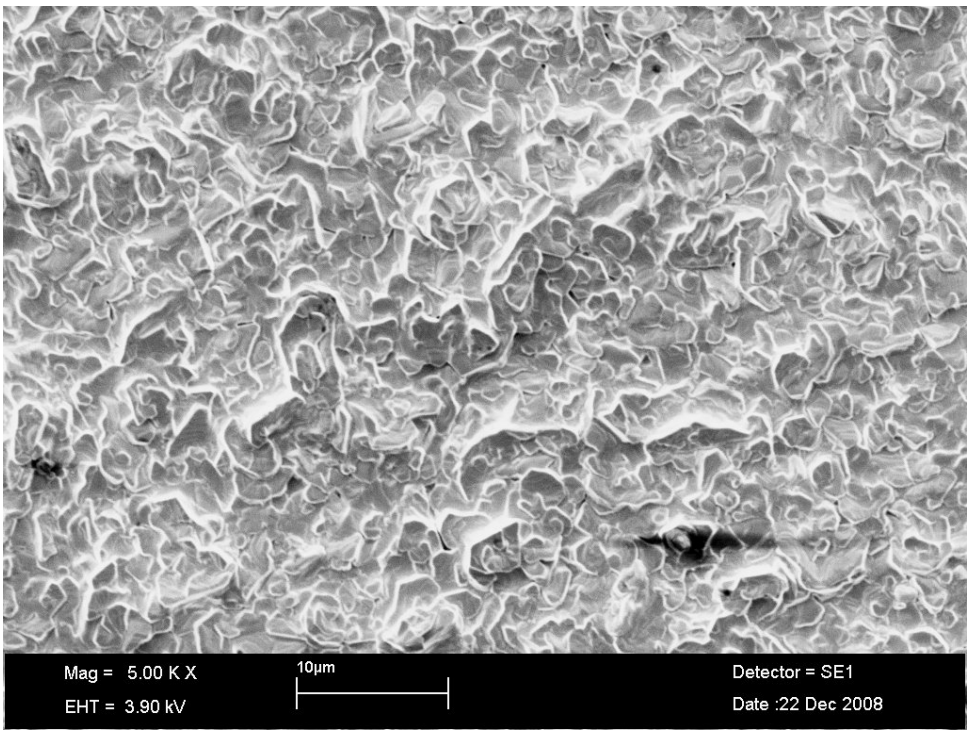

Figure 5-19: SEM image of the back surface of CdTe deposited by Durham. Scale bar represents 10 µm.

5.11 Conclusions

The CSS equipment constructed in this work was capable of achieving a 150 °C difference between the source and substrate block. It could also maintain this difference over a 30 min deposition run. This was partly attributed to the large mass of the graphite blocks used and the source substrate separation. The large mass of the blocks did mean a 10 minute warm up time was used, it would be possible to reduce this if required, by increasing the flux of the infra red light. The series of samples deposited with the adjusted deposition times indicated that no deposition occurred during the first 6 min. The deposition time quoted throughout this work includes this time and so typically deposition only consisted of 24 min of material being deposited. This is longer than some of the times reported by other groups (in the order of 10 min) this may be partially explained by considering the difference in the source and substrate separation (2 mm compared to the 8 mm used in this study) causing a lower deposition rate with the current equipment [18].

The variation of the deposition time showed that it was possible to control the deposition through adjusting the heating profile of the two graphite blocks. Both of the deposition mechanism expressions proposed by Cruz-Campa and Zubia suggest a reduction in the growth rate as the temperature difference between the source and substrate decreases. This would explain how the deposition is controlled by the temperature profiles with the deposition stopping quickly after heating due to the decreasing temperature difference.

The heat spreaders were found to improve the uniformity of the deposition. This is assumed to be due to a reduction in the temperature gradient across the sample, by increasing the temperature of the sample and causing it to be closer to the temperature of the graphite block it was in contact with.

The source material which had been used for several depositions was found to be Cd rich in composition. The new source material was stoichiometric within the accuracy of the measurement. This implies that at some point the source material underwent non congruent sublimation, to leave it Cd rich. Work by Guskov and Izotov presented parameters to calculate the partial pressures of Cd and Te_2 vapour for non congruent sublimation [4]. Their values were limited to the region of Cd and Te saturation in solid CdTe. The 0.57 atomic fraction of Cd found in the used source material, is outside the

region of saturated Cd in CdTe. The CdTe phase diagram indicates that for temperatures below the melting point of pure Cd (321 ℃) the composition of the material would exist in the form of a mixed solid phase of Cd and CdTe. Above the melting point, which corresponds to the temperatures of the source material during the sublimation process, the material would exist as a mixture of solid CdTe and a liquid phase. The ratio of the two phases in both cases could be determined using the Lever rule. A possible explanation for the source being Cd rich may be to consider the partial pressure of Cd gas is higher then that of Te_2 gas. This may cause the Te_2 gas to form more readily in a chamber with a partial pressure of Ar gas significantly higher than the vapour pressures of Cd or Te, causing the source material to become Cd rich.

The samples deposited under a range of pressures showed a variation in the amount of (111) preferred orientation between the samples. This is suggested to be due to a faster growth rate at the lower pressures and resulting in the fastest growth direction being more dominant over other crystallographic directions. The Williamson Hall plot of the data indicates the low pressure depositions have more strain present than the higher pressure depositions. This may again be accounted for by considering a faster growth rate allowing more structural defects to be incorporated in to the film, resulting in increase stress [19].

The influence of increasing the substrate temperature has been suggested to decrease the growth rate. This would imply the same deposition mechanism is dominant for the range of substrate temperatures evaluated here. The presence of oxygen in the deposition chamber is possibly indicated by the presence of smaller features on the surface of the samples. This may be linked with increase nucleation of CdTe grains consistent with what has been found by other research groups [17].

The CdTe deposited at Durham University enables a valid comparison, since the analysis of all the samples were carried out using the same equipment and procedures. The XRD analysis of the samples did not indicate the presence of a second phase in the reflections of the diffractograms. This may be due to several factors, assuming the second phase is due to the formation of a CdS_xTe_{1-x} alloy, annealing the CdS in a hydrogen atmosphere before the CdTe deposition could have a significant effect. Also the comparative thickness of the samples is unknown and this information may contribute towards an explanation. The lattice parameter of the material deposited at Durham is comparable

with the material deposited during this work. The texture coefficient calculated for the Durham samples (0.85 ± 0.1) was also comparable to the texture coefficient for the sample deposited at 0.2 mbar (0.92 ± 0.01) during the variable pressure series of samples. The difference between these samples is that the Durham samples were deposited on annealed CdS in an oxygen atmosphere and the pressure series samples were deposited on TCO in an argon environment.

References

[1] T. B. Massalski, *Binary Alloy Phase Diagram* (ASM International, 1990).

[2] J. H. Greenberg, Journal of Crystal Growth **161**, 1 (1996).

[3] J. H. Greenberg, V. N. Guskov, and V. B. Lazarev, Materials Research Bulletin **27**, 997 (1992).

[4] V. N. Guskov and Izotov, Inorganic Materials **44**, 1409 (2008).

[5] B. De Largy, A. Finch, and P. Gardner, Journal of Crystal Growth **61**, 194 (1983).

[6] R. F. Brebrick and A. J. Strauss, Journal of Physics and Chemistry of Solids **25**, 1441 (1964).

[7] S. N. Alamri, Physica Status Solidi A-Applied Research **200**, 352 (2003).

[8] J. L. Cruz-Campa and D. Zubia, Solar Energy Materials & Solar Cells **93**, 15 (2009).

[9] K. Mitchell, C. Eberspacher, F. Cohen, J. Avery, G. Duran, and W. Bottenberg, Solar Cells **23**, 49 (1988).

[10] H. Nagayoshi and K. Suzuki, in *IEEE Nuclear Science Symposium Conference Record* (2004), vol. 1-7, p. 4411.

[11] T. C. Anthony, A. L. Fahrenbruch, and R. H. Bube, Journal of Vacuum Science & Technology A-Vacuum Surfaces And Films **2**, 1296 (1984).

[12] T. Okamoto, Y. Harada, A. Yamada, and M. Konagai, Solar Energy Materials and Solar Cells **67**, 187 (2001).

[13] N. Romeo, R. Tedeschi, S. Pasquali, L. Ferrari, A. Bosio, V. Canevari, and R. Alfieri, in *16th European Photovoltaic Solar Energy Conference* (2000), vol. 1, p. 812.

[14] N. Romeo, R. Tedeschi, L. Ferrari, S. Pasquali, A. Bosio, and V. Canevari, Materials Chemistry and Physics **66**, 259 (2000).

[15] J. D. Major, Y. Y. Proskuryakov, K. Durose, and S. Green, Thin Solid Films **515**, 5828 (2007).

[16] G. Zoppi, K. Durose, S. J. C. Irvine, and V. Barrioz, Semiconductor Science and Technology **21**, 763 (2006).

[17] D. Rose, D. Levi, R. Matson, D. Albin, R. Dhere, and P. Sheldon, in *25th IEEE Photovoltaic Specialists Conference* (1996), p. 777.

[18] T. Chu, S. Chu, J. Britt, C. Ferekides, C. Wang, C. Wu, and H. Ullal, IEEE Electron Device Letter **13**, 303 (1992).

[19] M. Terheggen, H. Heinrich, G. Kostorz, D. Baetzner, A. Romeo, and A. N. Tiwari, Interface Science **12**, 259 (2004).

Chapter 6

Devices with CdS bilayers

6.1 Introduction

High efficiency devices have thin CdS layers to allow more long wavelength light through to the CdTe [1]. This thin layer can cause layer non-uniformity and any additional reduction in its thickness to cause a decrease in the shunt resistance. Annealing the CdS layers can be beneficial in terms of the layers' electrical properties. Jayakrishnan *et al.* found annealing in air at 500 ℃ reduced its resistivity [2]. This work also indicated that annealing in a nitrogen atmosphere decreased the resistivity further, this was attributed to oxygen desorption. Some of the reported results of annealing CdS may not all be beneficial. A decrease in the band gap of the annealed CdS has been reported [3]. A larger band gap has the benefit of allowing more light through the window layer to reach the CdTe. There are reports where the CdS was heated to higher temperatures, similar to the temperatures reached by the CdS on the substrate during the CdTe deposition in this work. Work by Hasoon *et al.* annealed CdS at 600 ℃ and observed an increased density of pinholes believed to be due to re evaporation of parts of the film [4]. Indeed the evaporation of CdS during the CSS deposition of CdTe has been observed during the present work with CdS depositing on the sample mount in the chamber.

CdS material can also be consumed by interdiffusion within the CdTe/CdS structure. Interdiffusion affects the lattice parameter and band gap of the materials and this will influence the performance of the devices. The lattice parameter of the CdS_xTe_{1-x} alloy is determined by Vergards law and linearly changes between that of CdTe and CdS. Work by Lane showed that for the CdS_xTe_{1-x} alloy the band gap was a minimum for x = 0.3 [5].

Therefore the formation of a $CdS_{0.3}Te_{0.7}$ alloy near the interface would decrease to the minimum the wavelength of the light absorbed in the CdTe layer within the device.

The desire is to have a CdS layer which has the improved electrical properties caused by an annealed layer while not suffering the increase in pinhole density during early stages of CSS deposition of CdTe. In principle this could be achieved by depositing a CdS bilayer consisting of a CdS double deposition with the initial film being annealed before the second deposition. In addition this could allow an annealed CdS layer to make up the majority of the overall layer and a second, possibly sacrificial film, of as-deposited material could be partially re evaporated and/or be consumed through interdiffusion into the CdTe. It is the suggestion of this work that a combination of the two types of material (as-deposited and anneal CdS) during the fabrication of the device may lead to a procedure which allows for more control over the overall CdS layer. This in turn may lead to an improvement in the device performance. Any improvement in the device would need to be substantial enough to warrant the extra cost of a more complex fabrication procedure.

In this chapter devices were fabricated which included CdS bilayers. The structure and electrical performance characteristics of these devices were then measured. Non destructive analysis techniques could be conducted during the production of, and on the completed devices. However to obtain more information about the CdS layer and the CdTe material close to the interface a destructive approach was undertaken. This involved initial mechanical polishing followed by successive etches of the whole sample to reduce the thickness of the CdTe.

6.2 IV consistency

To evaluate the reproducibility of the fabrication process, a series of samples were fabricated. The CdS layers were deposited for 15 minutes producing approximately 200 nm thick films. The CdTe was deposited by CSS and then the CdTe/CdS structures under went a $CdCl_2$ anneal for 30 minutes at 420 °C. A bromine:methanol etch was then carried out (25 ml methanol, 0.125 ml bromine). The samples were etched in groups and each group was submerged in the solution for a different length of time, see table 6-1. After the etches, gold contacts were evaporated onto the samples and IV measurements were

Table 6-1: Labels of samples etched for different lengths of time

Sample labels	**Time submerged in the etch solution (second)**
W1, W2, W3, W4	20
X1, X2, X3	10
Y1, Y2, Y3, Y4	10
Z1, Z2, Z3, Z4	5

carried out.

The term 'rollover' is used to describe the IV curve, for small values of current density close to the open circuit voltage, where the data deviates from a single diode response. Rollover occurs due to a rectifying back contact which creates the effect of a second diode at the back contact of the device [6]. The equivalent circuit diagram of a device with rollover can be seen in figure 6-1. The ECN software expression used in this work uses two diodes to model the response of a device with ohmic back contacts. This can also be more approximately modelled by a single diode. The model is not complicated enough to fit accurately samples with rollover, see figure 6-2. The model clearly deviates from the data for the sample with the rollover at the back contact.

The samples in this section which exhibited rollover were: W1, W2, W3, W4 and Z4. These samples had larger Chi squared values for the model fit than the other data. The properties of the back contact are dependent on the back surface etch. Samples W1, W2, W3 and W4 were all etched with the longest submergence time. The results show that

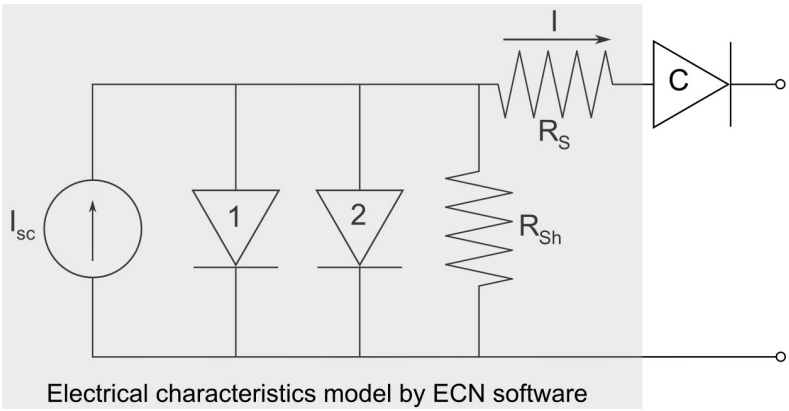

Figure 6-1: The equivalent circuit diagram of a device with a rectifying back contact. The rectifying contact here is represented by the additional diode, c.

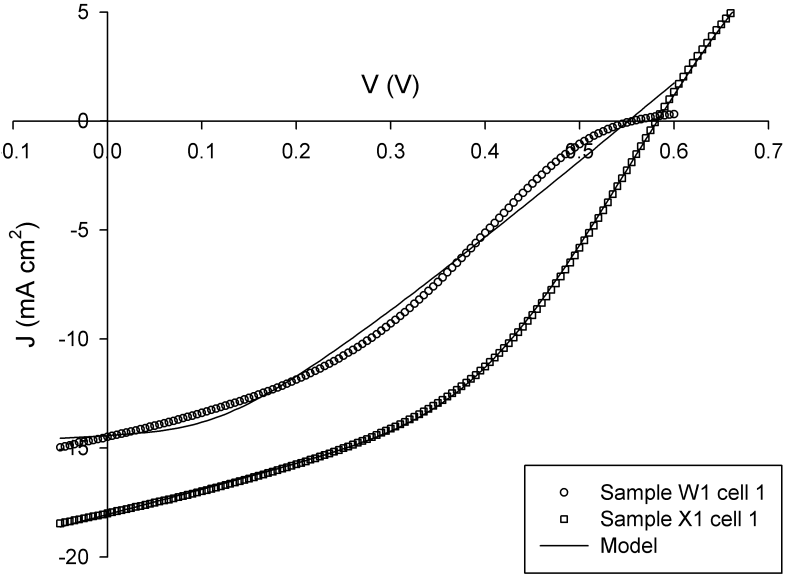

Figure 6-2: Examples of the fit of the model to the data for a sample with (W1) and without (X1) back contact rollover. The software calculated a Chi squared value for the fit of the model to the data, for sample X1 cell 1 a value of 0.093 was found and for sample W1 cell 1 a value of 0.4664.

long etch does not produce good back contacts. Sample Z4 display of rollover behaviour is an anomaly.

The figures of the IV parameters show the variation between samples which have undergone the same etch treatment, see figure 6-3 and 6-4, box plots can be seen in the appendix A.3. This shows the variation which can occur between samples over the multiple steps in the fabrication process. Each sample had six contacts on its back surface, some of the contact values overlap and so all six values can not be easily distinguished. Although some of the samples have a large variation between the six contacts on the same specimen, some samples have a good consistency across all six cells, sample X3 is the best example of this. The structural and composition measurements made in this work were generally made on the middle of the samples, and with no reference to a specific position relating to a cell's parameters. Therefore it is a requirement to have samples with as much consistency across the specimen as possible to be able to relate the IV parameters to the other measurements. The results of sample X3 and others demonstrate that it is possible to produce samples by the method used in this work with consistent electrical parameters across the whole specimen.

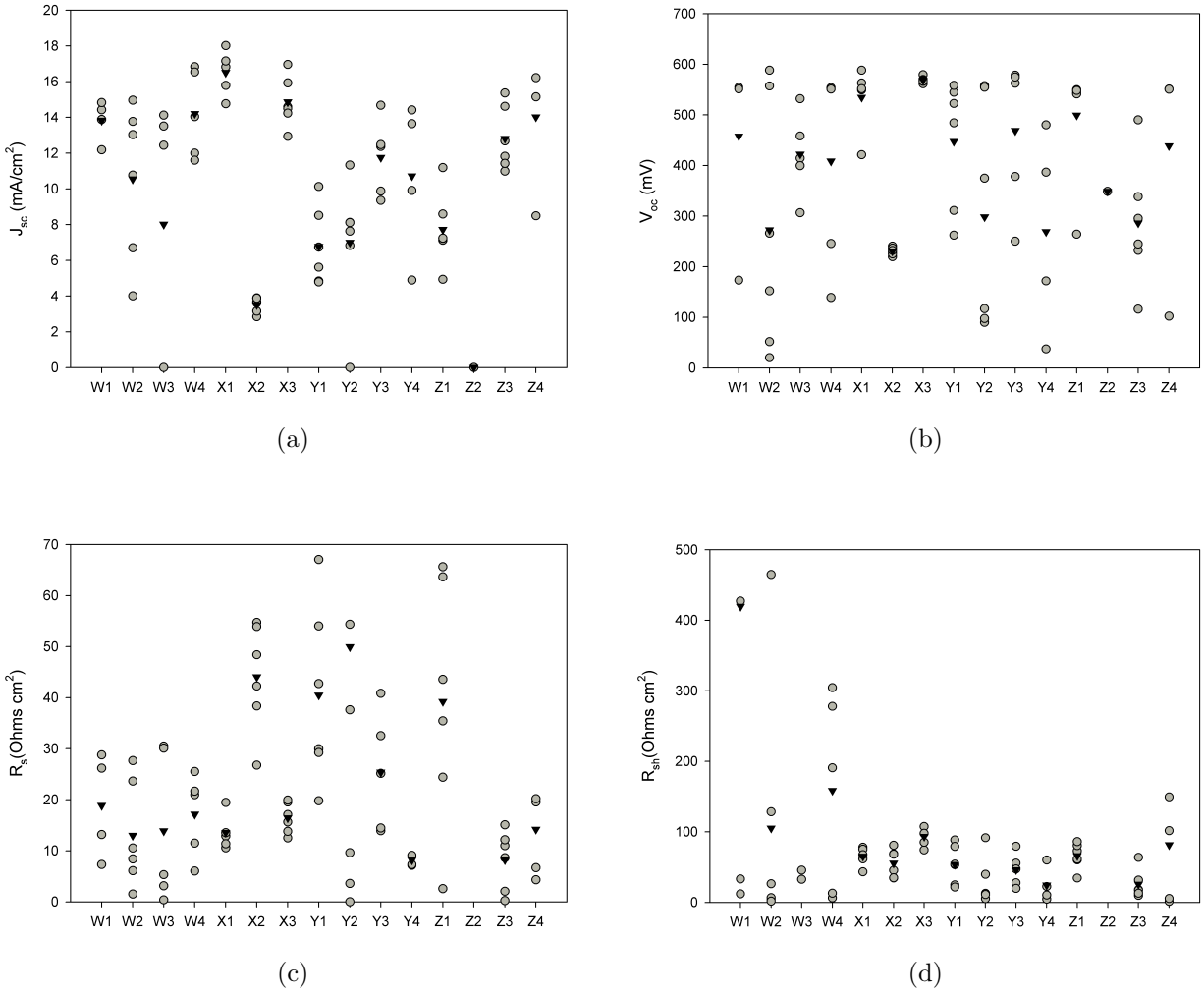

Figure 6-3: The figures show (a) the short circuit current density, (b) open circuit voltage, (c) series resistance and (d) shunt resistance are displayed for each sample to show the spread of the values across the different samples. The triangles symbols show the average of the cells.

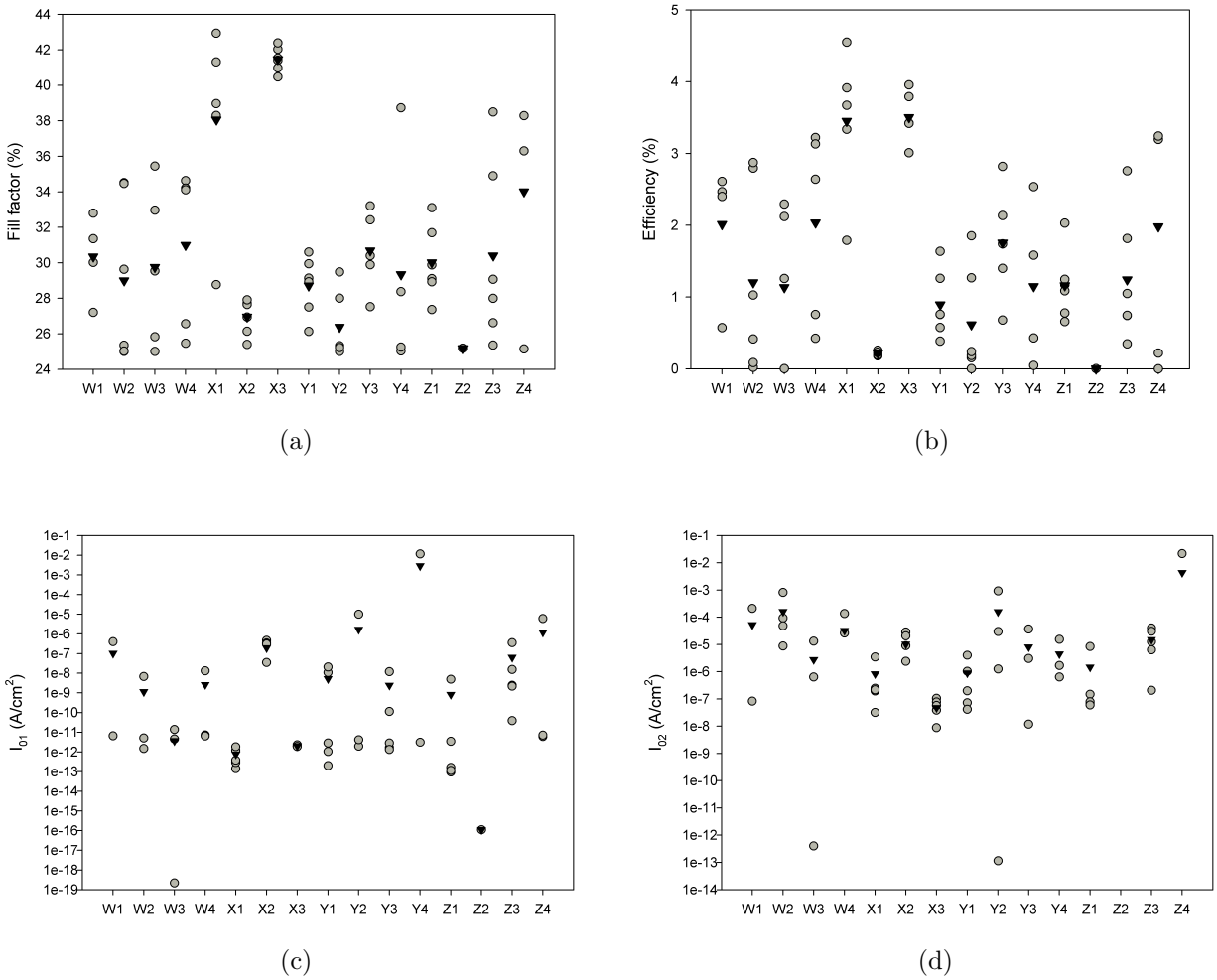

Figure 6-4: The figures show (a) the fill factor, (b) efficiency, (c) 1^{st} diode saturation current density and (d) 2^{nd} diode saturation current density are displayed for each sample to show the spread of the values across the different samples. The triangles symbols show the average of the cells.

A low series resistance is beneficial for device performance since it is linked with a device having a higher short circuit current density. It is possible to see within the results a relationship between the samples with a low series resistance and the high short circuit current density. The open circuit voltage has a distinct upper limit of approximately 600 mV. This is lower than the value of 845 mV reported for some of the highest efficiency CdTe/CdS cells [1]. The I_{02} diode parameters being a few orders of magnitude larger then the I_{01} parameters indicate the current recombination process was largest within in the depletion region of the device.

6.3 Sample fabrication

To combine annealed and as-deposited CdS requires two deposition stages to form the overall CdS bilayer. For simplicity either one or two depositions of CdS were used to form the overall CdS layers for each sample in this work. Two types of anneals were carried out on single deposited CdS layers during this section. Firstly an air annealing process where the sample was heated to 420 ℃ in atmosphere for 30 min. Secondly a cadmium chloride anneal where the sample was dipped in a saturated solution of methonal:$CdCl_2$ for 2 min, then dried and heated in the same way as the air annealed samples. Using these two treatments along with leaving the samples as-deposited enabled six variations of the overall CdS layer to be fabricated, see table 6-2.

The same deposition parameters were used for all of the CdS depositions. This meant that the samples which had two CdS depositions had an overall CdS layer which was approximately twice as thick as the single deposited layers. Work by Oladeji showed for multiple chemical bath depositions of CdS, the thickness of subsequent CdS depositions was 100% to 120% the thickness of the original film, for the same deposition parameters [7].

The CdTe deposited on these CdS layers were deposited under the same condition with the exception of two deposition pressures being used. The two gas pressures used were 3 and 7 mbar. These pressures were chosen because they correspond to the extreme values of the argon gas flow gauge. The pressure variations would allow the possible effect of the deposition rate to be investigated.

A $CdCl_2$ treatment was carried out following CdTe deposition and before the back sur-

Table 6-2: The table gives information about the different deposition parameters for the CdS and CdTe layers for each sample and the corresponding sample name. There was only one sample for each of the combinations with the exception of the single as-deposited CdS with CdTe deposited under 7 mbar, here there was no sample deposited.

Sample labels	**CdTe deposition pressures**	
Description of the overall CdS layer	**3 mbar**	**7 mbar**
Single as-deposited layer	A3	-
As-deposited layer on top of an as-deposited layer	AA3	AA7
Single air annealed layer	B3	B7
As-deposited layer on top of an air annealed layer	BA3	BA7
Single $CdCl_2$ annealed layer	C3	C7
As-deposited CdS on top of a $CdCl_2$ annealed layer	CA3	CA7

face was prepared for the deposition of the back contacts. A back surface bromine:methanol etch was followed by the evaporation of the gold contacts. An area on each sample was then prepared as the front contact.

6.4 Initial measurements

XRD measurements of the CdS layers before the CdTe deposition showed a variation between the samples in the position of the reflection at approximately 26.5 ° 2θ. Due to the thin nature of the CdS layers the intensity of its diffractogram peaks are small compared to the SnO_2 peaks of the Tec 15 glass. No single reflection from the diffractogram can be attributed to resulting from just the CdS layer, see figure 6-5. The reflection at 2θ approximately equal to 26.5 ° can be assigned to a combination of the SnO_2 and the CdS materials.

Diffractograms comparing annealed and as-deposited CdS on glass can be seen in figure 6-6. The CdS annealed samples have the diffraction reflections associated with a wurtzite structure, as would be expected [8]. The central peaks were fitted at 2θ equal to 26.52 ° for $CdCl_2$ annealed and 26.54 ° for air annealed. The diffraction reflection of the as-deposited CdS (fitted at 26.76 °) resulted from a structure with a different d-spacing to the annealed samples. This change in the d-spacing could be associated with a possible change in the structure from wurtzite to zincblende. However using a database the peak position for zincblende CdS (ICCD card 1-647) was found to be approximately 26.51 °,

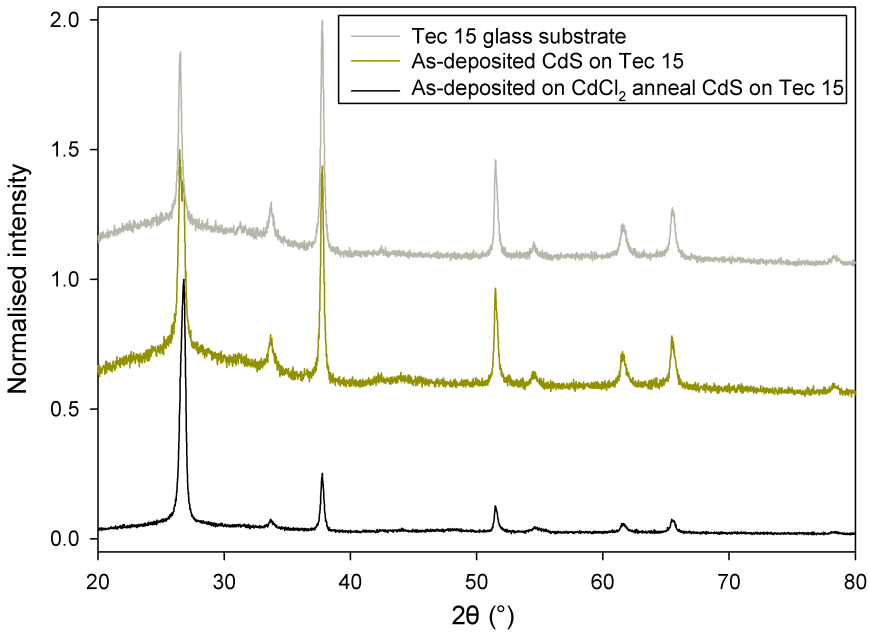

Figure 6-5: XRD of Tec 15 TCO glass substrate with and without CdS deposited on top

whilst for the wurtzite structure (ICDD card 1-780) the position was approximately 26.59 °. With only one peak it is difficult to identify with certainty the phase of the material. The higher 2θ position may indicate the presents of uniform strain within the CdS which changes the d-spacing from what would be expected for either structure.

The coherence length of the CdS in these films was estimated using Scherrer formula. The as-deposited CdS had a crystallite size of 7.1 ± 0.7 nm while the air annealed had 9.4 ± 1.3 nm crystallites and the $CdCl_2$ annealed had the largest crystallites of 24.6 ± 8.1 nm.

The XRD reflections for the different CdS layers on the Tec 15 substrates in the 2θ region of 25.5 to 27.5 ° can be seen in figure 6-7. The reflection for a single as-deposited CdS layer on Tec 15 glass were fitted with two peaks, see figure 6-8(a). These peaks were assigned to the Tec 15 (26.49 ± 0.01 °) and as-deposited material (26.81 ± 0.01 °). These fits were 'stable' ie. the refining algorithm produced a good fit with two peaks and the position of the peaks after the refinement was always in the same place. In contrast the fits for the reflections for the single annealed CdS layers on Tec 15 glass were not 'stable' fits, since the reflections could be fitted adequately with only one peak. However fitting with one peak was not a physically realistic solution since a contribution from both the CdS and Tec 15 needed to be included in the solution. Also neither individual material

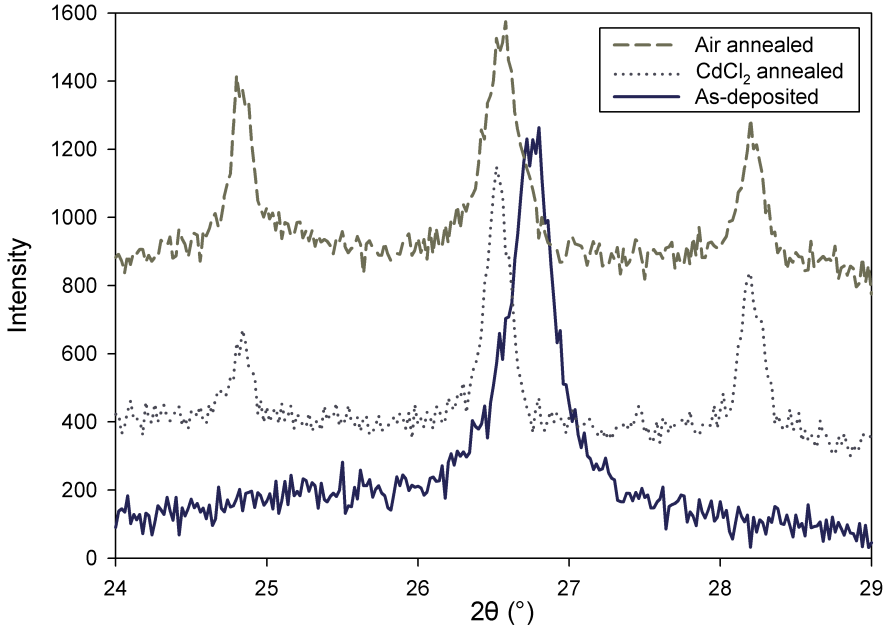

Figure 6-6: X-ray diffractograms of CdS deposited on glass which have undergone different treatments. The diffractograms have been offset from each other for clarity. The $CdCl_2$ and air annealed CdS have three peaks which would be expected for a hexagonal structure.

peak had a position which corresponded to the position of the reflection maxima. The result was that these reflections were fitted by restraining the position of the peaks in the refinement to the positions found from fitting the individual layers of each material. For the reflections from samples with a single annealed CdS layer on Tec 15 glass two peaks were fitted, one was assigned for Tec 15 SnO_2 ($26.49 \pm 0.01\,°$) and one for the annealed CdS ($26.58 \pm 0.01\,°$). It was noted that unlike the CdS annealed on the glass no adjacent peaks associated with a wurtzite phase were observed which may be due to their small intensity. Similar to the single as-deposited layers the double as-deposited layer were fitted with two peaks. For the films containing as-deposited and annealed CdS three peaks were used to fit the data, see figure 6-8(b). These fits were again not 'stable', and so the peak positions were restrained. A table of the peak positions and relative intensities of the fitted peaks is given in table 6-3.

It was assumed that depositing CdS on CdS which had been annealed at 420 ℃ would not change the structure of the annealed CdS. Using this assumption these fits would imply that the CdS grown on top of the annealed CdS did not have the same d-spacing as the underlying CdS. Thus the overall CdS layer created by two CdS depositions consisted

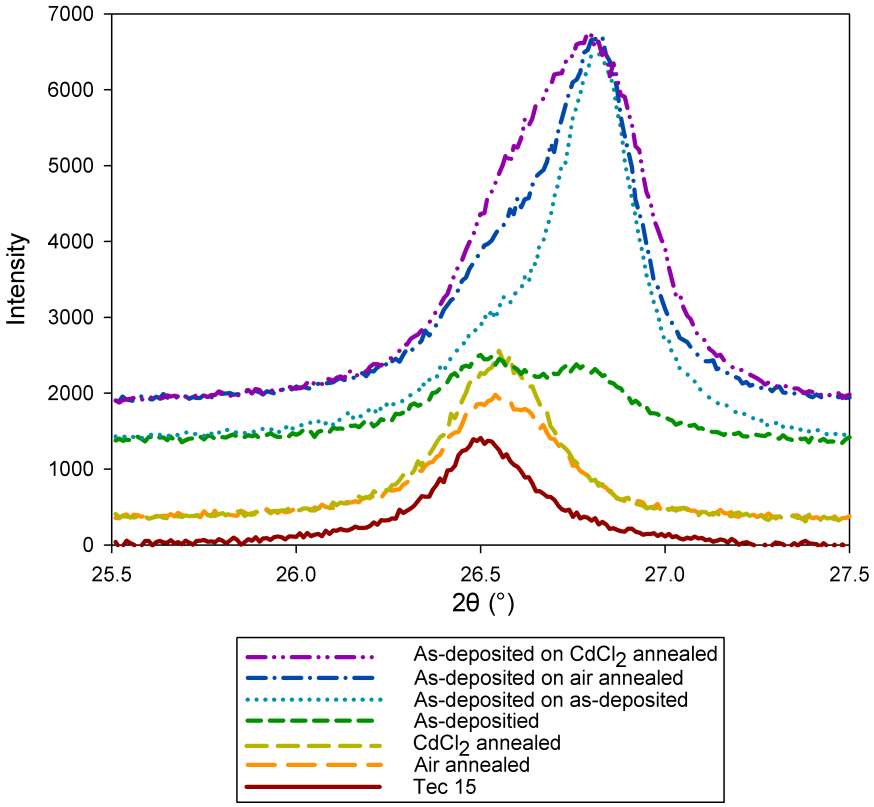

Figure 6-7: Diffractograms of the CdS layers in the 2θ region of 25.5 to 27.5 °. The reflections are for the overall CdS layers which have undergone different treatments and these can be compared with the reflection of a plain Tec 15 glass substrate. The diffractograms have been offset from each other for clarity.

Table 6-3: Displays the 2θ position and the percentage intensity of the fitted peaks for each of the reflections displayed in figure 6-7.

	Peak 1		**Peak 2**		**Peak 3**	
Description of the overall CdS layer	**2θ**	**intensity (%)**	**2θ**	**intensity (%)**	**2θ**	**intensity (%)**
Tec 15 glass	26.49	100	-	-	-	-
Single as-deposited layer	26.49	100	26.80	71	-	-
Single air annealed layer	26.48	86	26.57	100	-	-
Single $CdCl_2$ annealed layer	26.49	100	26.57	66	-	-
As-deposited layer on top of an as-deposited layer	26.50	25	26.80	100	-	-
As-deposited layer on top of an air annealed layer	26.49	12	26.59	44	26.80	100
As-deposited layer on top of a $CdCl_2$ annealed layer	26.48	7	26.59	73	26.81	100

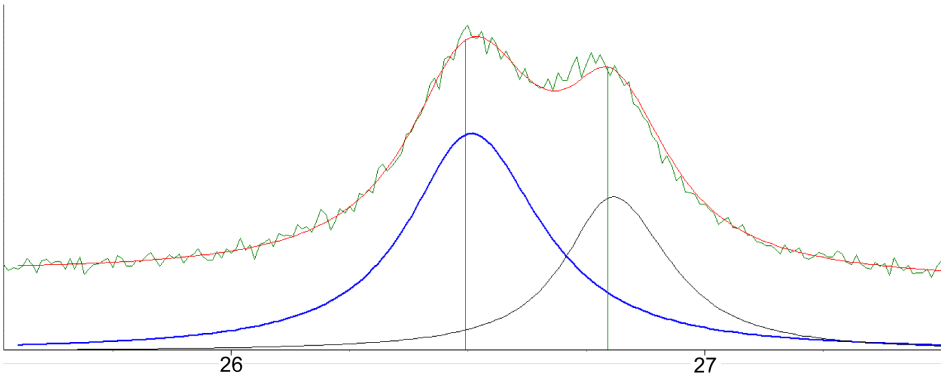

(a)

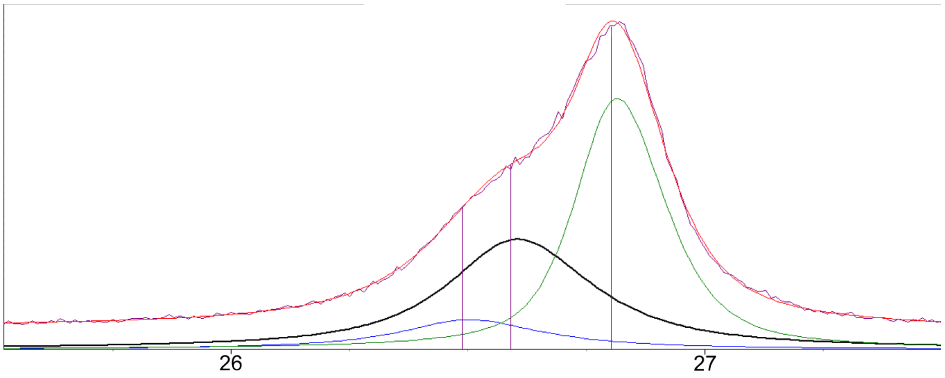

(b)

Figure 6-8: Examples of fits for CdS/Tec15 XRD reflections with multiple peaks fitted for each of the materials present, in the 2θ range 25.5 to 27.5°. The smooth top line in each image is the fit to the data. The top image (a) is for as-deposited CdS on Tec 15 glass with the lower angle peak being the Tec 15 peak. The bottom image (b) is for as-deposited CdS on air annealed CdS on Tec 15 glass.

of two forms of CdS.

No significant variation could be seen in the SEM images of the top surface of the CdTe deposited on different substrates (see figure 6-9). This could be explained by any possible effect of the substrate on the CdTe morphology not being transmitted through the thick CdTe layer. A suggested difference between the CdTe deposited under the two different pressures may be that at the higher pressure there appears to be more smaller grains present between the larger grains.

Thickness values for the CdTe were determined by RBS measurements, the calculation assumed stoichiometric CdTe, see figure 6-10. The thickness of the tin in the Tec 15 glass was measured separately, initially, and then fixed as a constant in later fits. The model structure used for the samples consisted of CdTe, on CdS, on SnO_2 glass. The measurements were not very sensitive to the thickness of the CdS. The errors assigned

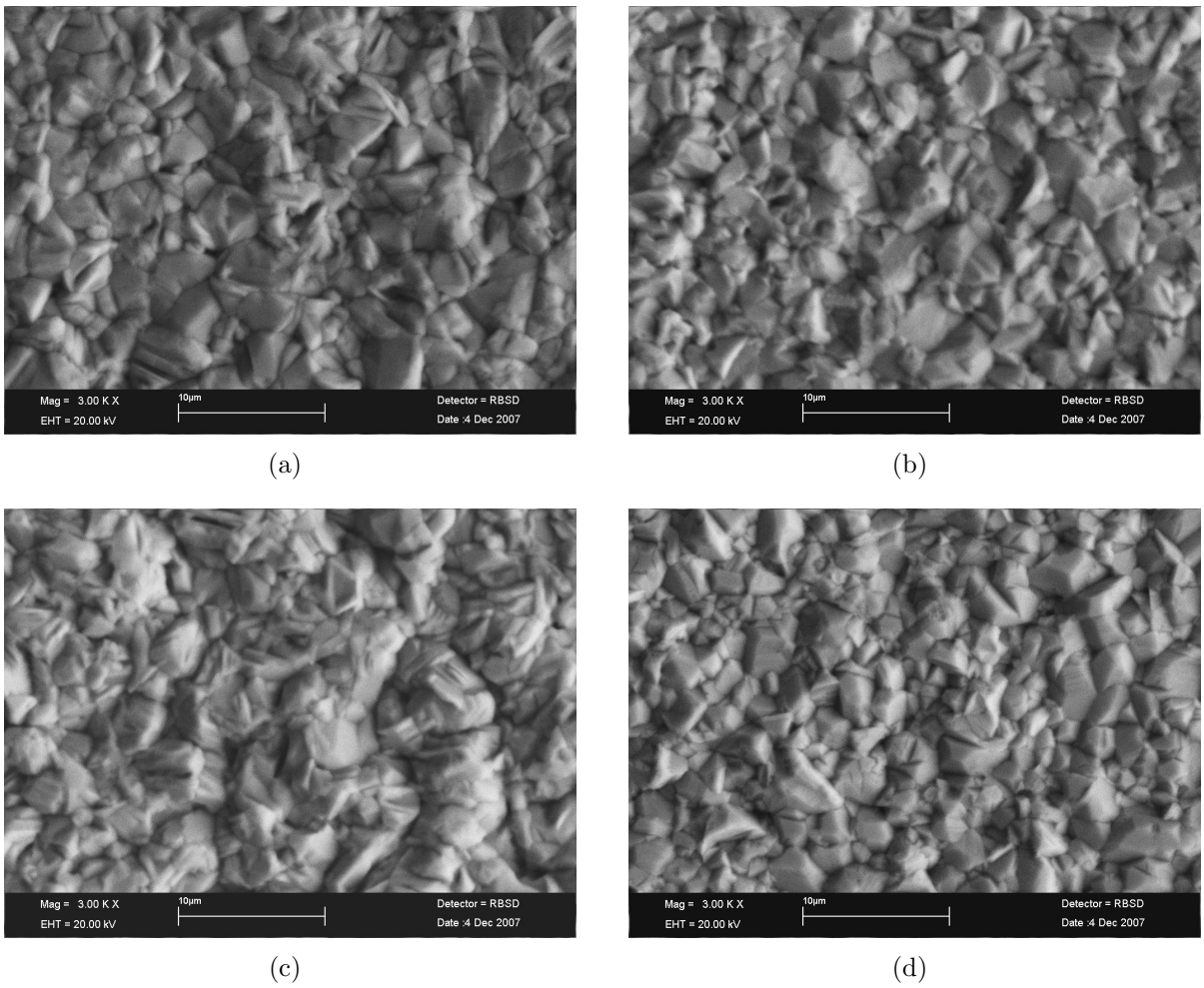

Figure 6-9: SEM images of annealed CdTe samples; (a) B3, (b) B7, (c) BA3 and (d) BA7, the images have a 3000 magnification with the bottom bar equal to 10 µm in all of the images. The top row of images are for samples with a single air annealed layer of CdS, the bottom row samples have as deposited CdS on top of air annealed CdS.

to the thickness of the CdS were between 50 and 100 % of the layer thickness. The gradient of the back edge of the peak was affected by the roughness of the substrate and the amount of interdiffusion between the layers. Neither of these affects could be isolated and therefore were not determined.

The measurements show the large difference between samples in the thickness of the CdTe after the $CdCl_2$ anneal, see figure 6-11. The samples with an initial thickness around 10 µm were all deposited under 3 mbar of pressure. The five samples deposited at 7 mbar all have a similar thickness around 5 µm. This agrees with the theory of a faster growth rate at lower pressures. The thickness of the A3 sample is an anomalous result as the CdTe layer seemed very thin compared with other samples deposited under 3 mbar

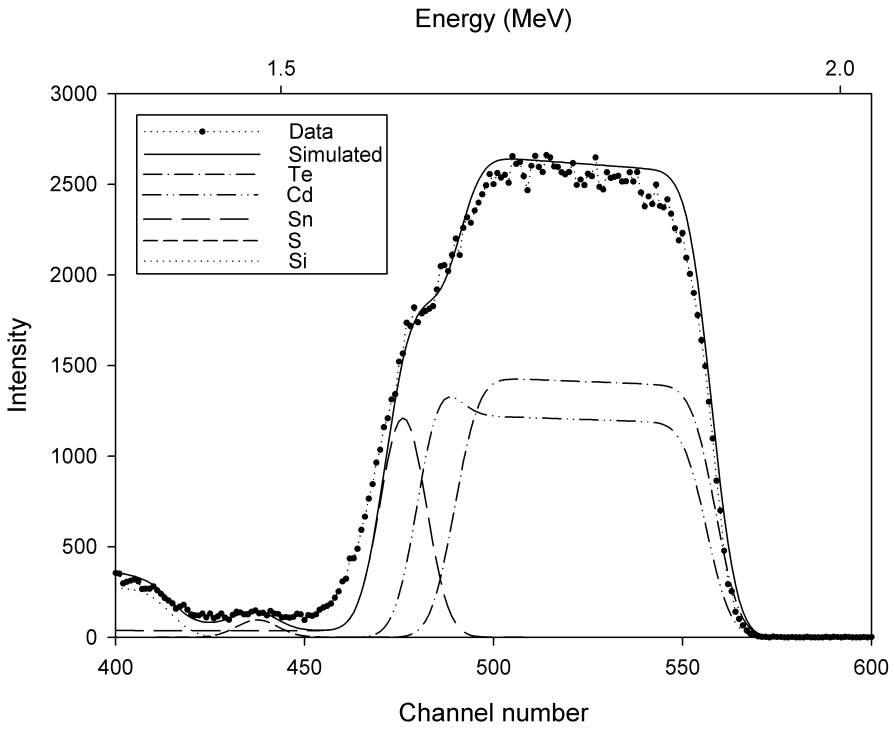

Figure 6-10: Sample AA7 after the mechanical polishing treatment. This sample has a CdS bilayer and so the CdS layer influence can be possibly seen in the size of the shoulder on the back edge (low energy side) of the peak.

of pressure.

The change in the thickness of the CdTe between chemical etches varied with different etches and different samples. This was a result of different lengths of time being used for the chemical etches of the different samples, to try and remove more CdTe from the thicker samples.

The IV characteristics of the six cells for each sample provided a way of checking the consistency of the measurements across each sample, see figure 6-12 and 6-13, box plots can be seen in the appendix A.3. Five of the eleven samples had a good response from all six cells. The highest efficiency cell from this sample set was sample CA3 with an efficiency of 5.7 %. The samples had non isolated contacts. This means that all the efficiencies in this work are therefore upper estimates. The results show that the samples deposited under 3 mbar of pressure perform better than those deposited under 7 mbar of pressure.

For IV measurements for this set of samples only B3 and B7 displayed rollover. This would lead to the shunt resistance and open circuit voltage values of these two samples not being very accurate. The V_{oc} for all the samples except A3 is higher then that observed

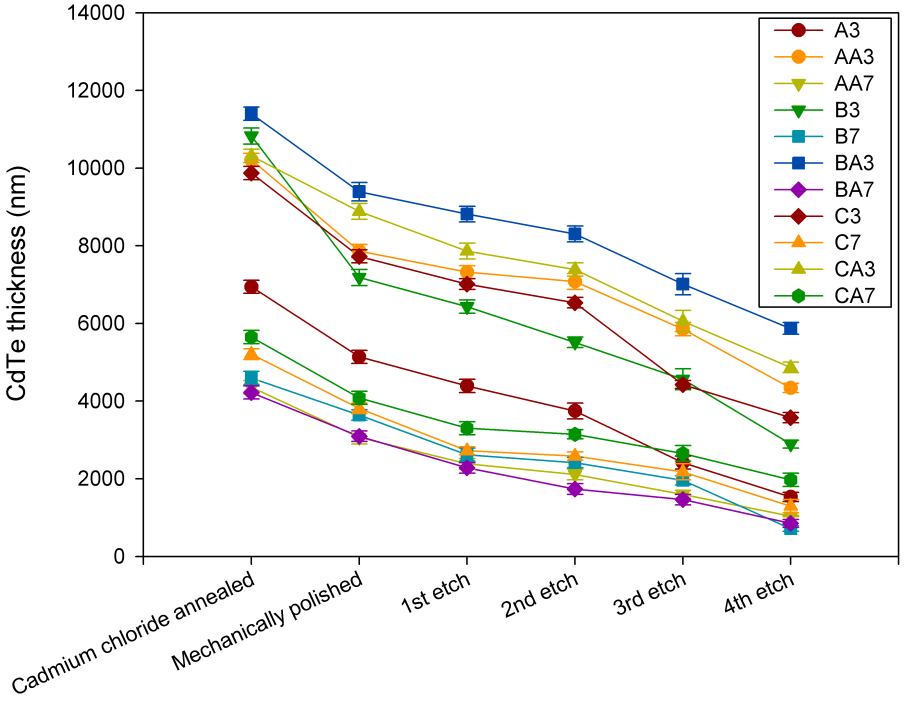

Figure 6-11: RBS CdTe thickness measurements for CdTe/CdS samples after successive treatments.

for the 15 samples with just an as-deposited layer of CdS (see 6.2). The highest open circuit voltage was observed for the samples with a single $CdCl_2$ annealed CdS layer. This may indicate that the changes observed in the V_{oc} may be very dependent on the quality of the CdS material. The thickness of the CdS layer is a relatively small percentage of the overall device thickness. However doubling the thickness of the CdS layer does not appear to have an adverse effect on the series resistance. The higher efficiencies of the samples with the CdTe deposited under a 3 mabr compared to 7 mbar may be linked to the higher shunt resistance of these samples. This may be associated with a change in the thickness of the CdTe under the two pressures. No distinct improvement in the efficiency of the device due to a CdS bilayer can be seen. Comparing the efficiencies of devices which include the same annealed CdS layer the addition of the extra as-deposited CdS does not seem to have much effect. The I_{02} parameters for the samples which included a $CdCl_2$ annealed CdS layers suggest less current recombination occurred in the depletion region for the samples without the bilayer CdS structure. The results suggest that the annealed CdS material has better electrical properties then the as-deposited material.

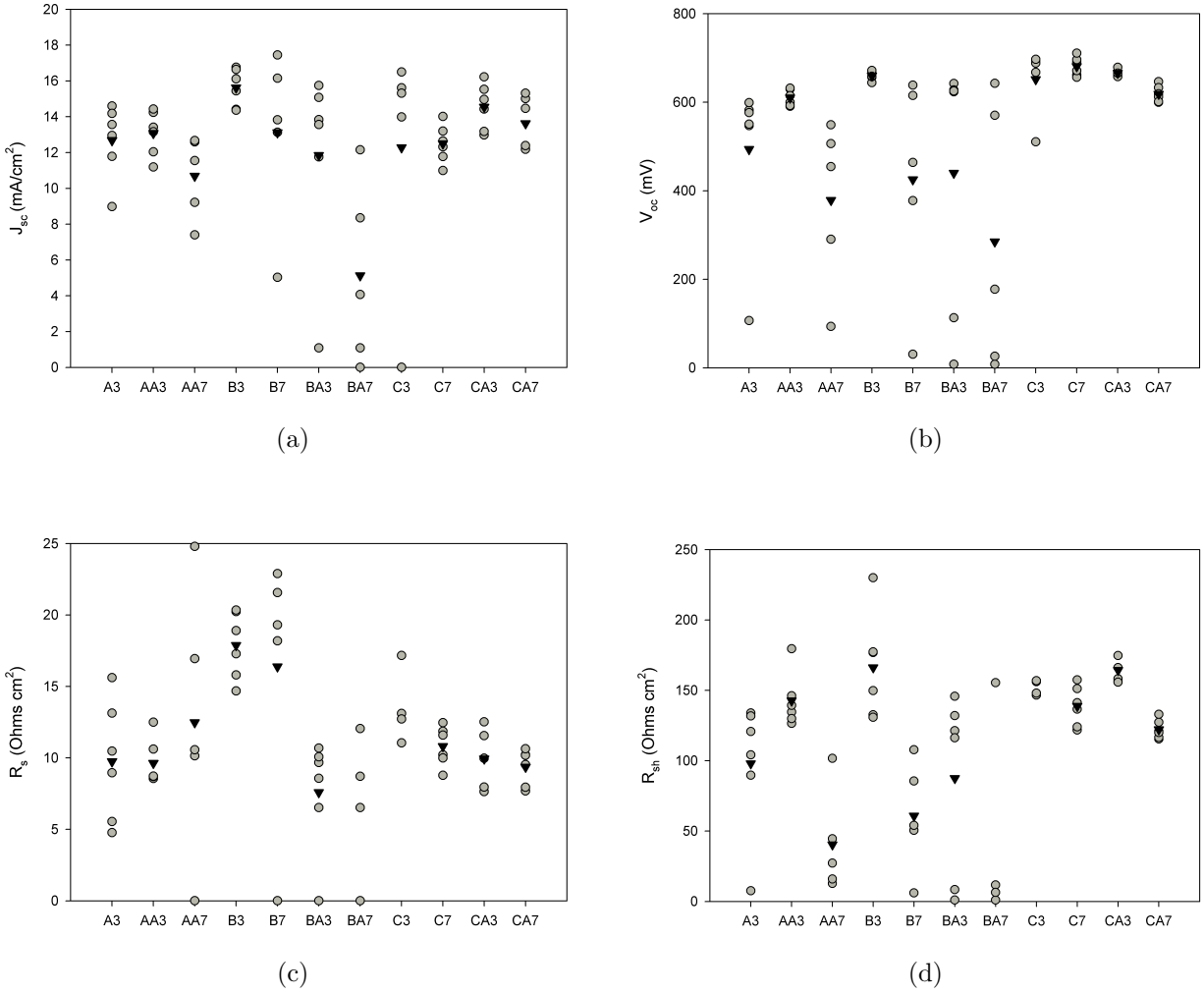

Figure 6-12: The figures show (a) the short circuit current density, (b) open circuit voltage, (c) series resistance and (d) shunt resistance are displayed for each CdS bilayer sample to show the spread of the values across the different samples. The triangles symbols show the average of the cells. The samples with CdTe deposited under 3 mbar show a better performance than the cells deposited under 7 mbar.

Therefore the samples with $CdCl_2$ annealed CdS may indicate that either; not all of the as-deposited CdS present within the bilayers devices was consumed during the fabrication or that any alloy formed did not improve the recombination current.

The spectral responses for the samples fabricated with only one CdS deposition had a higher response below 500 nm than the other samples, see figure 6-14. This indicates that the reduced thickness of the CdS allowed more of the light to reach the CdTe layer which would otherwise be absorbed by the CdS. Alternatively for the thicker double deposited CdS layers, light with high energies below 500 nm was absorbed within the CdS layer away from the interface and did not contribute towards the current. All of the samples

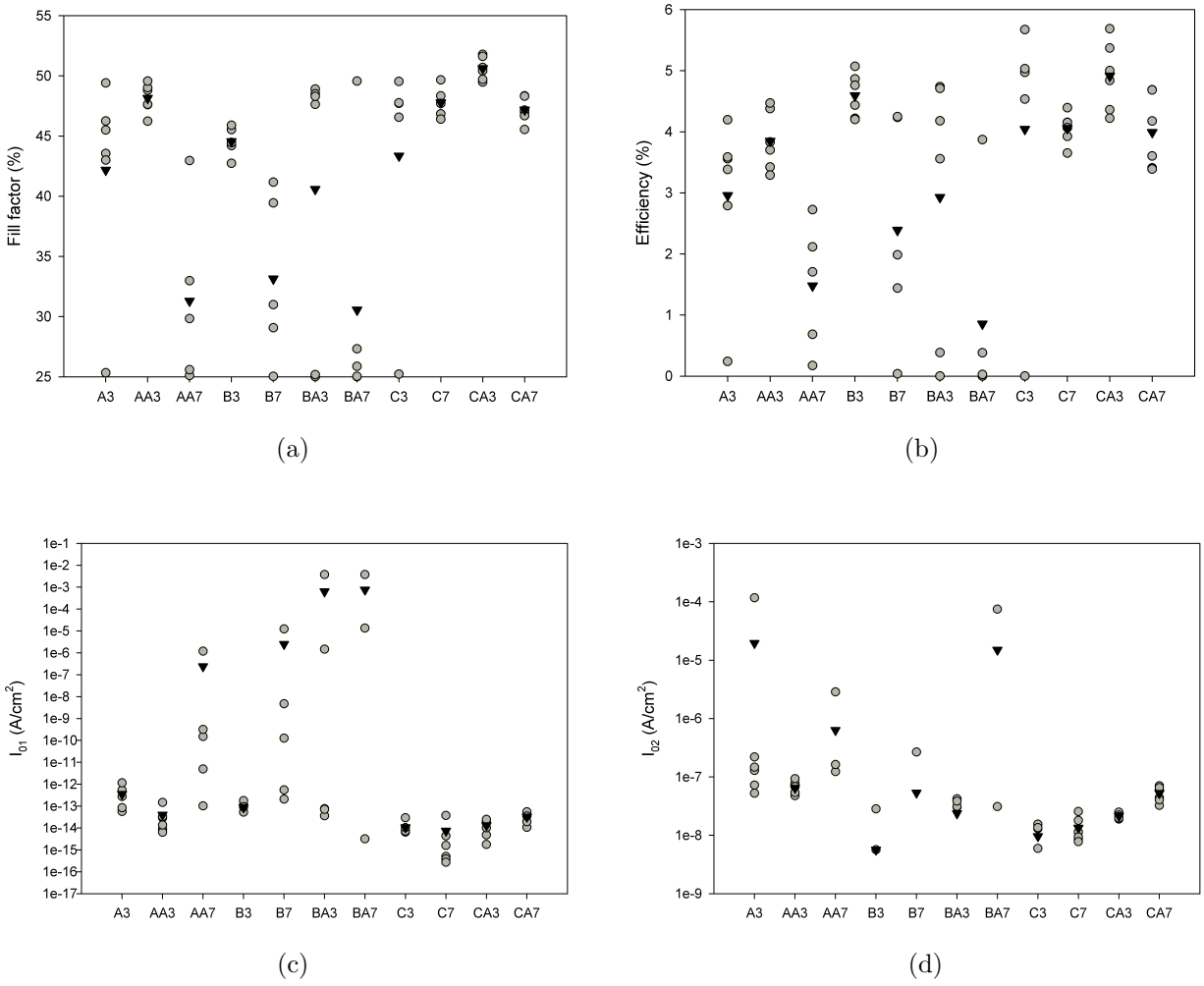

Figure 6-13: The figures show (a) the fill factor, (b) efficiency, (c) 1^{st} diode saturation current density and (d) 2^{nd} diode saturation current density are displayed for each CdS bilayer sample to show the spread of the values across the different samples. The triangles symbols show the average of the cells. The samples with CdTe deposited under 3 mbar show a better performance than the cells deposited under 7 mbar.

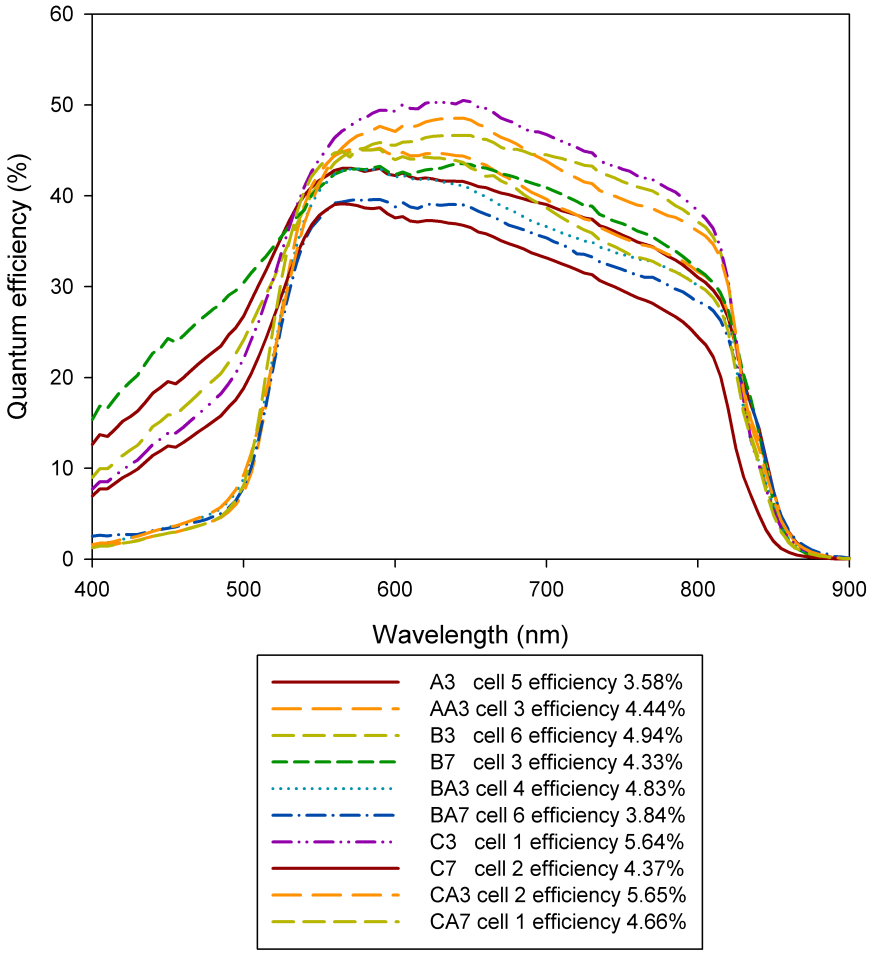

Figure 6-14: The typical spectral response from each of the etched samples. No spectral response for sample AA7 was measured due to the poor quality of the sample.

except A3 have a shift in the longer wavelength absorption edge to longer wavelength. The absorption edge should correspond to the bandgap of CdTe which would mean light is not absorbed above approximately 850 nm. The increase in light absorption above this wavelength may correspond to the interdiffusion of sulphur into the CdTe. The similar shift in the majority of samples is irrespective of the different CdS treatments.

6.5 Depth profiling measurements

A chemical etch was selected as the preferred way of destructively removing material from the samples as it was believed it would be the more reproducible procedure compared to mechanical polishing. However the gold back contacts on the devices could not easily be

removed with a chemical etch. The devices were therefore initially mechanically polished by hand to remove the contacts.

A PoliFloc 4 polishing pad was loaded on to a mechanical polishing wheel and a Dia Duo 1 μm diamond suspension lubricant was used. The samples were held against the polishing pad with as uniform a pressure as possible. They were polished till the obvious signs of the gold contacts had disappeared.

RBS and XRD measurements were taken after the mechanical polishing. The samples were then successively etched and measured to obtain information as the amount of CdTe material was removed.

The highest intensity Tec 15 reflections were observed in samples where the CdTe thickness was ~5.5 μm or thinner. This shows that for these samples the CdTe reflections were resulting from measurements which penetrated through the whole CdTe layer. Small contributions to the reflections which were suspected to be due to CdS were only observed when the thickness of the CdTe was of the order of a few hundred nanometers. Other small peaks were observed only after the annealing treatments and these may be due to a cadmium oxide forming.

During the XRD measurements the X-ray source tube in the equipment deteriorated over a period of two months and was replaced. The reflections from the silicon standard measured throughout this time were all shifted by a similar amount, from their normal positions. The reflections of the measured samples in this period would also have been shifted and therefore correspond to an incorrect d-spacing. The magnitude of the shift in the reflections measured during this time was calculated to be $0.098 \pm 0.015\,^{\circ}$. This was use as a correction value and was added to all the fitted reflection positions measured during this time.

The texture coefficient for the seven CdTe peaks observed in the XRD 2θ range $20\,^{\circ}$ to $80\,^{\circ}$ was calculated from the set of measurements (see figure 6-15). The results show two distinctive groups within the samples. These groups do not correlate with the thickness of the CdTe layer. All four of the samples with the lower texture coefficient only had one deposition of CdS. The exception to this was sample C7 which has the higher texture coefficient indicating the higher degree of preferred orientation.

The errors in the texture coefficient were calculated using the standard deviation of the intensities. Although some of the high angle peaks in the highly ordered material

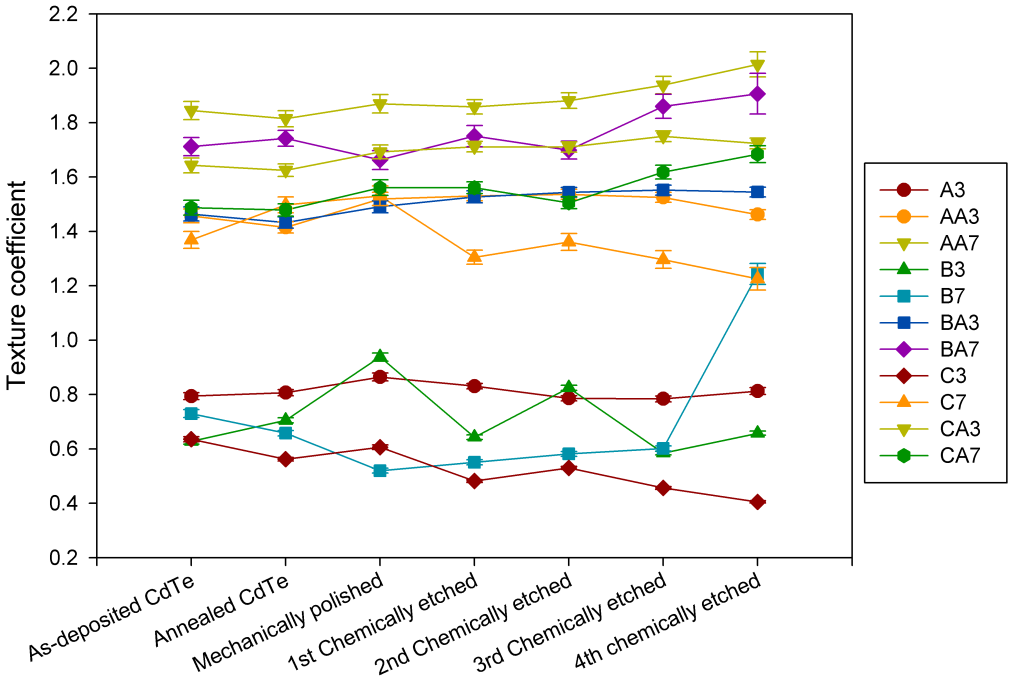

Figure 6-15: The texture coefficient for the XRD measurements as the CdTe is removed through successive etches. For seven peaks if there was perfect orientation along one direction the texture coefficient would be 2.4, while for completely random orientation of the peaks the value would be 0.

had very low intensity and therefore had large percentage errors, the small intensity of these peaks meant that the errors assigned did not over influence the overall errors of the texture coefficient.

There seems to be little variation in the lattice parameter as the samples were etched, see figure 6-16. The small variation in the lattice parameters implies that the destructive treatments of the samples did not change the d spacing of the samples. Any change in the d-spacing would have to affect a reasonable portion of the sample since shallow surface effects could be lost due to the weighting of the bulk material. The small decrease in the lattice parameter after the mechanical polishing could possibly relate to a change in strain in the surface region of the CdTe effecting the XRD measurement. However the time period over which the XRD source tube deteriorated corresponds to the time when all of the mechanically polished measurements and a few other measurements were made. Although a correction was applied to the fitted peak positions, an increase in the error of the position due to the correction, which was not considered, may cause the

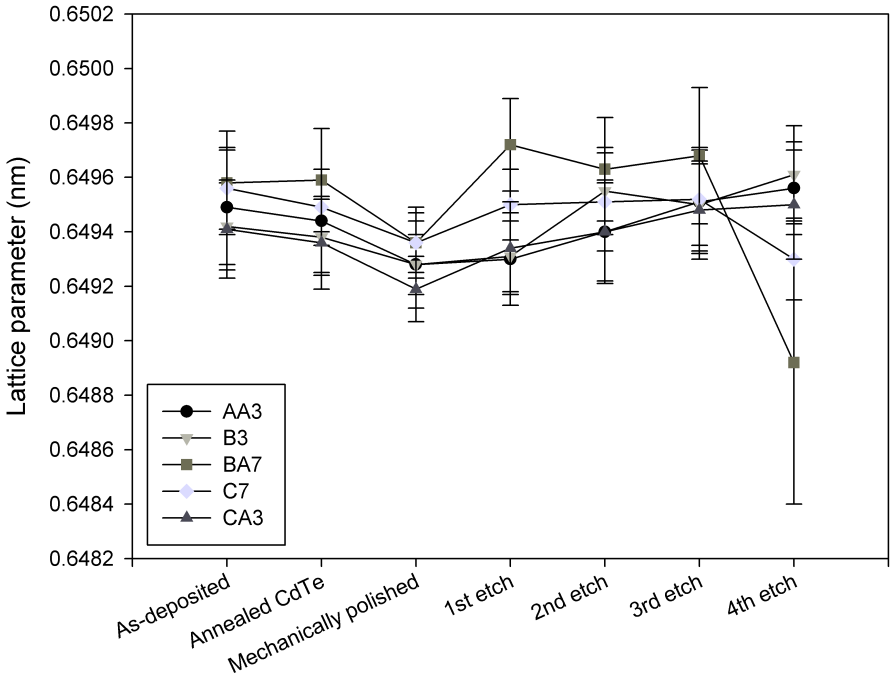

Figure 6-16: A plot of the lattice parameter obtained through Taylor Nelson plots against the treatments of the samples. Note that all the mechanically polished samples along with some annealed and 1st etched samples had the peak position corrected due to the deterioration of the X-ray source tube.

lattice parameter to agree with adjacent treatment results. The greatest variation in the lattice parameter for the 4th etched samples occurred in samples C7 and BA7. This was attributed to the fact that these samples were some of the thinnest samples and so the CdTe close to the interface could be affected by strain or non stoichiometric composition.

For Williamson Hall measurements the size of the grains in CdTe can often be larger than the 0.1 μm upper limit, on the size of the crystallites which have a detectable effect on the broadening of the peaks ([9] Page 283). It would therefore be expected that any size contribution to the broadening would arise from only the smaller grains in the samples and grains with structural defects. Strain broadening contribution can arise from a gradient in the composition [10] and so may be a way of indicating different gradients in the compositions of the samples due to different amounts of interdiffusion.

In the samples in this work the integral breadth varies with inverse d indicating the presence of a strain component in the broadening, see figure 6-17. There also appears to be some {hkl} dependence on the integral breadth which may have some dependence on

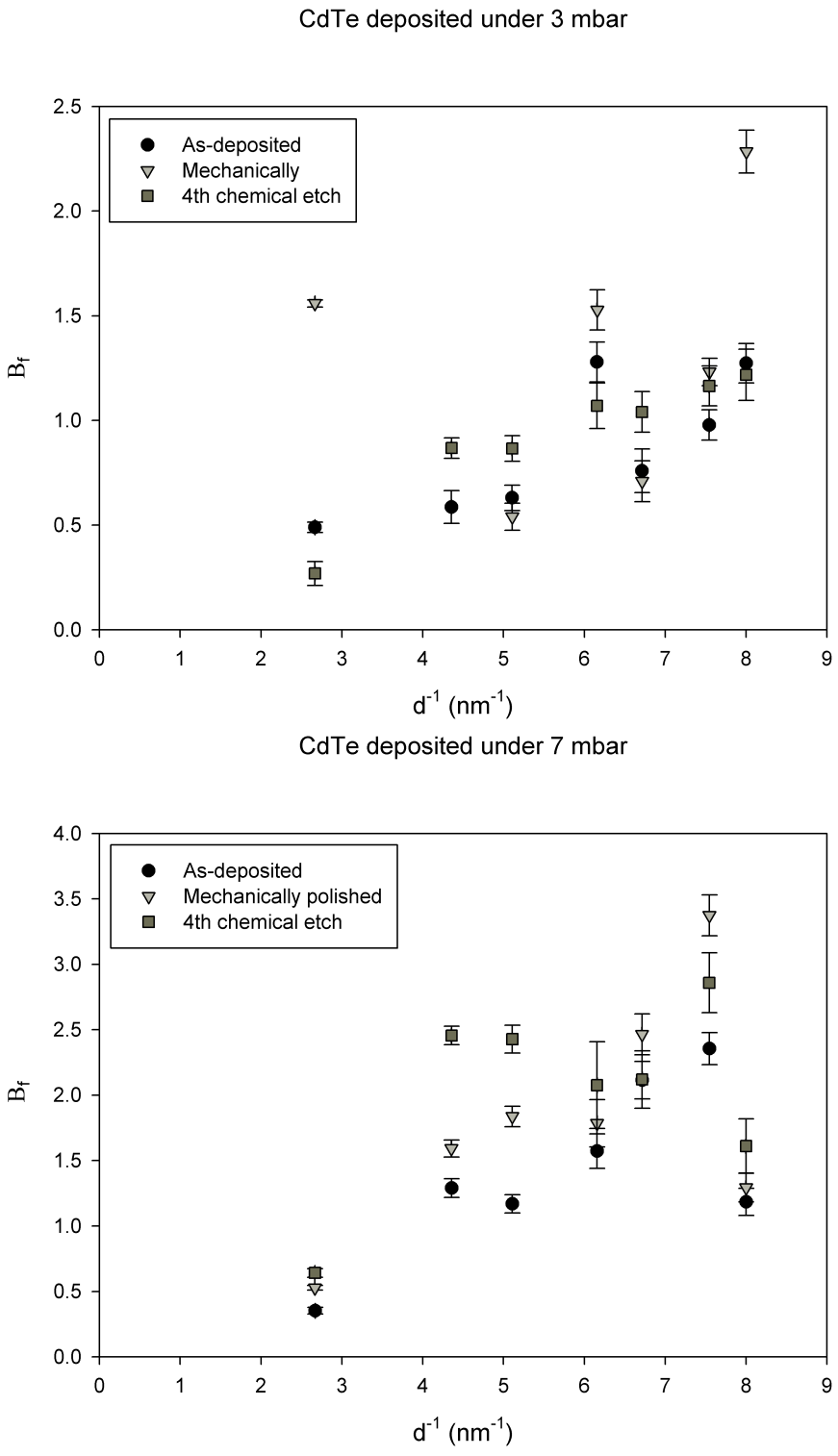

Figure 6-17: Examples of the Williamson Hall plot for two samples with $CdCl_2$ annealed CdS layers. They illustrate the pattern of the samples where CdTe deposited with 3 mbar of pressure have a different strain for the peak at approximately a d^{-1} of 6 nm^{-1} (400). While the peaks at d^{-1} approximately equal to 8 nm^{-1} (511) for samples deposited with 7 mbar of pressure also have a different strain

the CdTe deposition parameters. The Miller indices of the seven CdTe peaks examined here were: (111), (220), (311), (400), (331), (422) and (511). The angle between the (400) and the (511) is 15.79°. There is a large angle between these directions and the (111) direction (54.74° and 38.94° respectively). The difference in the strain for these two directions may indicate a slightly different crystal orientation for the two deposition pressures but both with an overall preferred (111) orientation.

Some examples of the gradient of the regression fits for the Williamson Hall plots can be seen in figure 6-18. The majority of the samples showed little variation similar to sample CA3. However three of the samples showed an increase in the gradient as the sample got thinner. The increase in the gradient of sample BA7 may show an increase in the strain caused by a gradient in the composition or structural defects since the intercept remained small. The values used in figure 6-18 are regressions which included all seven reflections. For samples AA7, B7 and C7 the inverse integral breadth for the first (111) peak is small and if this peak was excluded the resulting regressions would have small gradients but large intercepts, see figure 6-17 C7 4th chemical etch. This may imply that

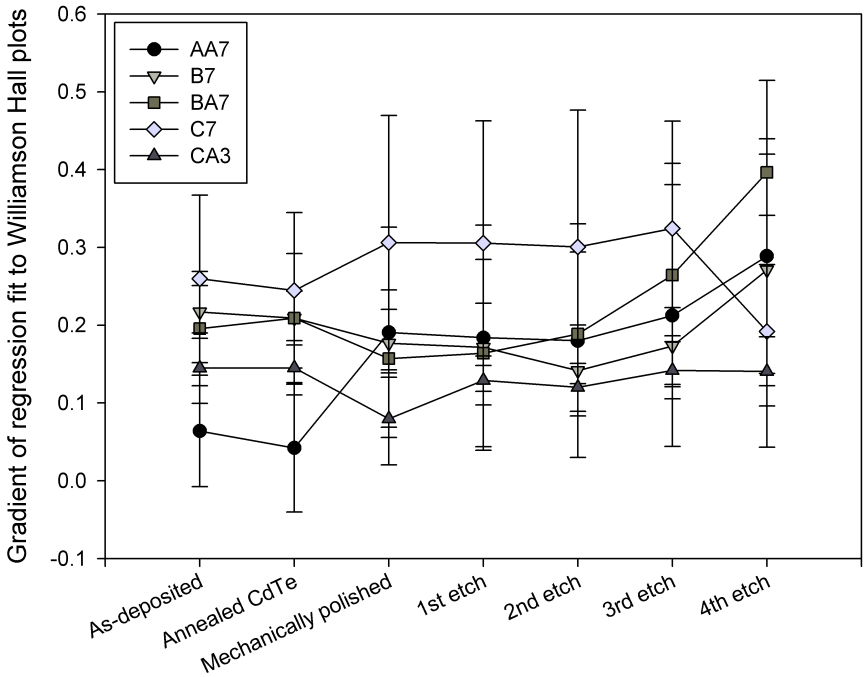

Figure 6-18: The gradient of Williamson Hall plots after different treatments. The majority of the samples had little variation in the gradient, similar to the results of sample CA3.

strain in these samples is mainly due to grain size rather than compositional changes. The asymmetry due to the measurement is largest at low angles and decreases with increasing angle. This may cause an increased error in the integral breadth calculated for the first reflection.

6.6 Thinned CdTe measurements

After the fourth etch the samples had XRD measurements taken at the normal angular step size of 0.02 ° which were discussed in the previous section. They also had measurements made at a smaller angular step size of 0.005 °. This increased the number of data points per reflection and enabled the reflection shape to be examined. Also the number of CdTe reflections was increase from 7 to 11. These reflections were fitted with Pseudo Voigt peak shape functions.

When the higher resolution data was analysed only four of the samples had two phases fitted to their reflections. The rest of the samples were fitted with only one phase, here still referred to as the first phase, see figure 6-19. The second phase seems to have a distinctly different lattice parameter from the first. The notable exception is sample BA7 which had a high degree of preferred orientation for the (111) reflection. This caused the other reflections to have very low intensity and consequently not to produce a 'stable' fit when using the two peaks. The reflections were therefore fitted with only one peak. The lattice parameters suggest that although it is not possible to fit two phases to the data the presence of a second phase in sample BA7 should not be discounted. Comparing the CdTe thickness with the lattice parameter results shows that samples; A3, AA7, B7, BA7, C7 and CA7 have the thinnest CdTe layers, with thickness less than 2 μm. This may indicate that this second phase is only present close to the interface.

6.7 Ellipsometry

Tec 15 glass substrate was used to provide the TCO layer in this study. Work by Von Rottkay and Rubin produced an optical model for Tec 15 glass [11]. An optical model based on their work provided a good match for experimental data, which allowed subsequent layers on top of the Tec 15 layer to be fitted with confidence. A good fit for

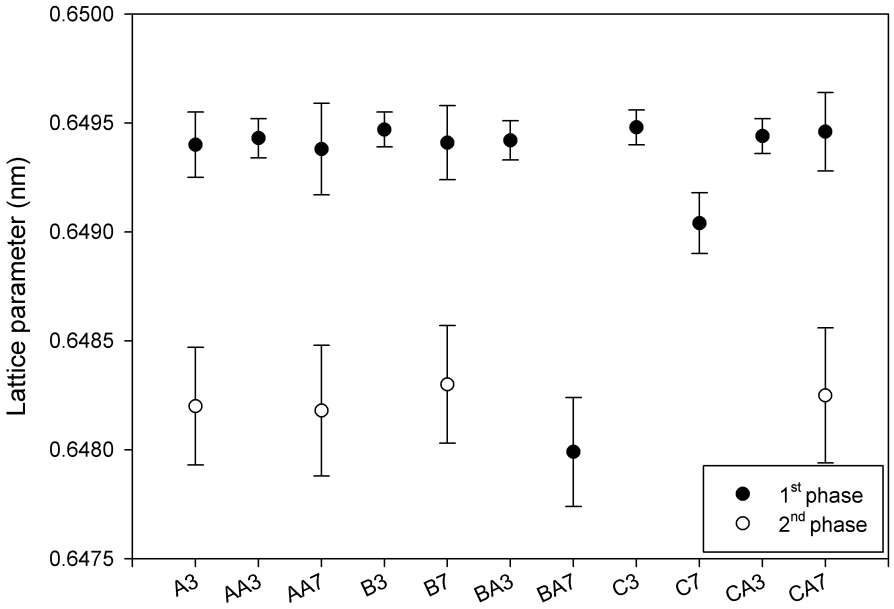

Figure 6-19: The lattice parameter determined from Taylor Nelson plots for the XRD measurements with the higher resolution.

Tec 15 over the whole wavelength range was achieved using a 5 layer model on a Cauchy substrate. The resulting fit gave an MSE of 6.62 (see figure 6-20 and details are given in appendix A.2).

CdTe films were deposited on silica substrates to allow an optical model to be created. The surface roughness of the as-deposited CdTe scattered the polarised light and could prevent an ellipsometry measurement from being made. To reduce the surface roughness the top surface of the CdTe was etched with a bromine:methanol solution. The etched samples had a surface smooth enough that the light could reflect off of the surface and measurements could be taken. The optical properties were fitted over the whole wavelength range with a Cody Lorentz and four Lorentz oscillators, see figure 6-21. The optical model created for CdTe in this study used values published in the literature as a guide for the size and location of the oscillators [12, 13]. To fit the CdTe films deposited on the silica substrates, an EMA layer was introduced between the CdTe and silica substrates. This combined the optical properties of CdTe with those of void material (see figure 6-22 and details are given in appendix A.2). This EMA layer may be linked with poor uniformity of the initial layer forming on the silica surface.

Annealed CdS films deposited on the silica substrates demonstrated the change in

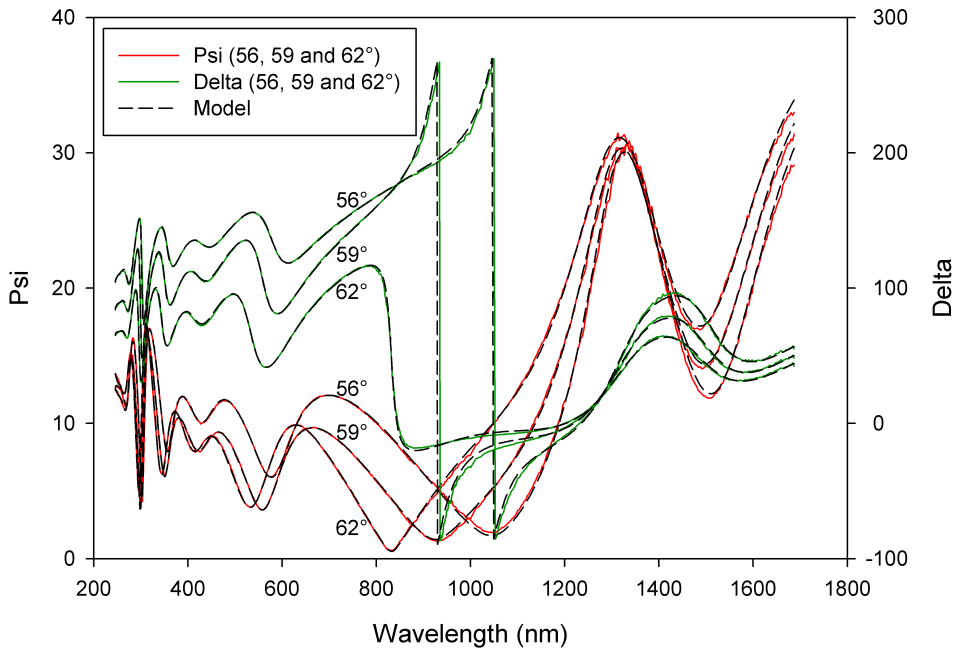

(a)

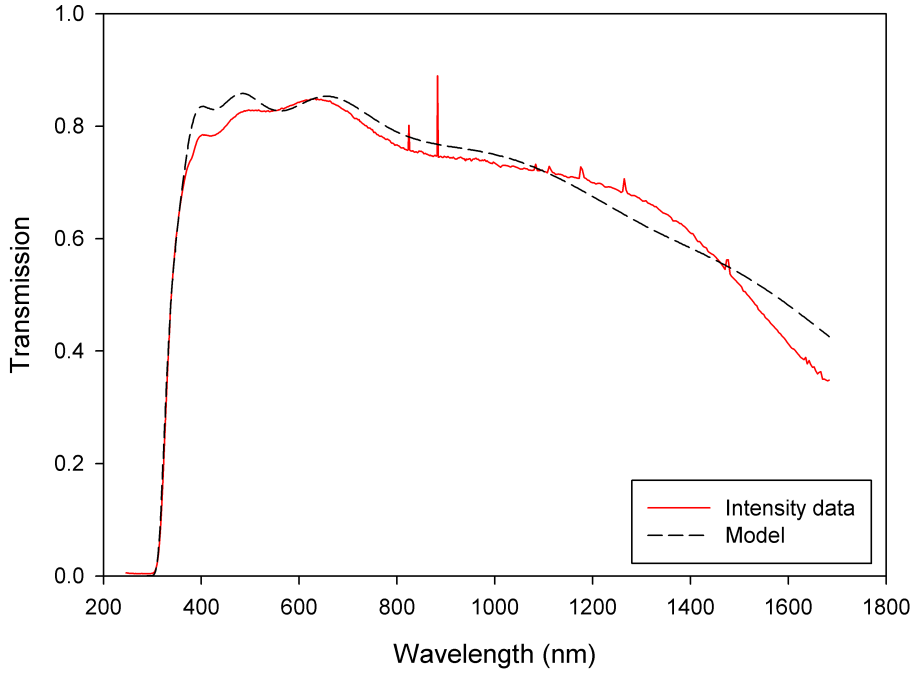

(b)

Figure 6-20: Ellipsometric data along with the model for the Tec 15 glass. These figures shows data measured in (a) reflection and (b) transmission modes. The model fitted the data with an MSE of 6.62.

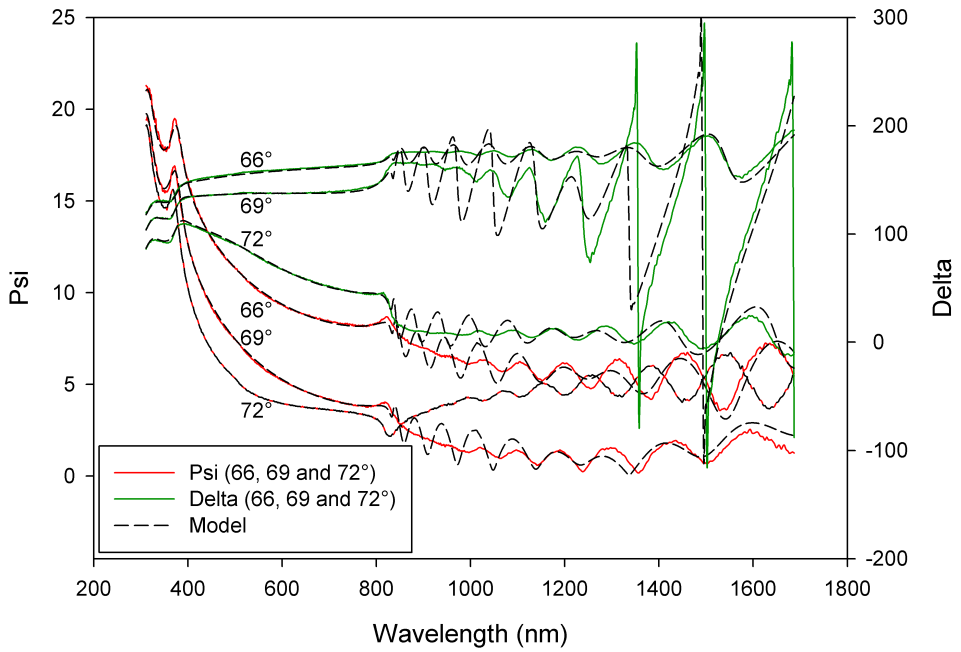

(a)

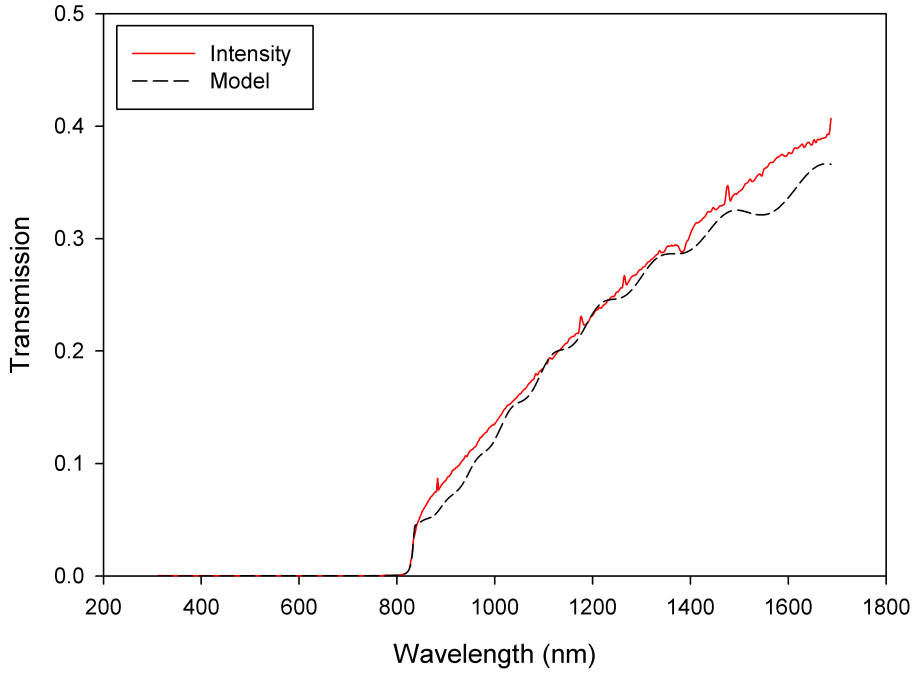

(b)

Figure 6-21: Ellipsometric data for CdTe deposited on a silica substrate. The figures show the data measured in (a) reflectance and (b) transmission modes. The model fitted to the data with an MSE of 11.38.

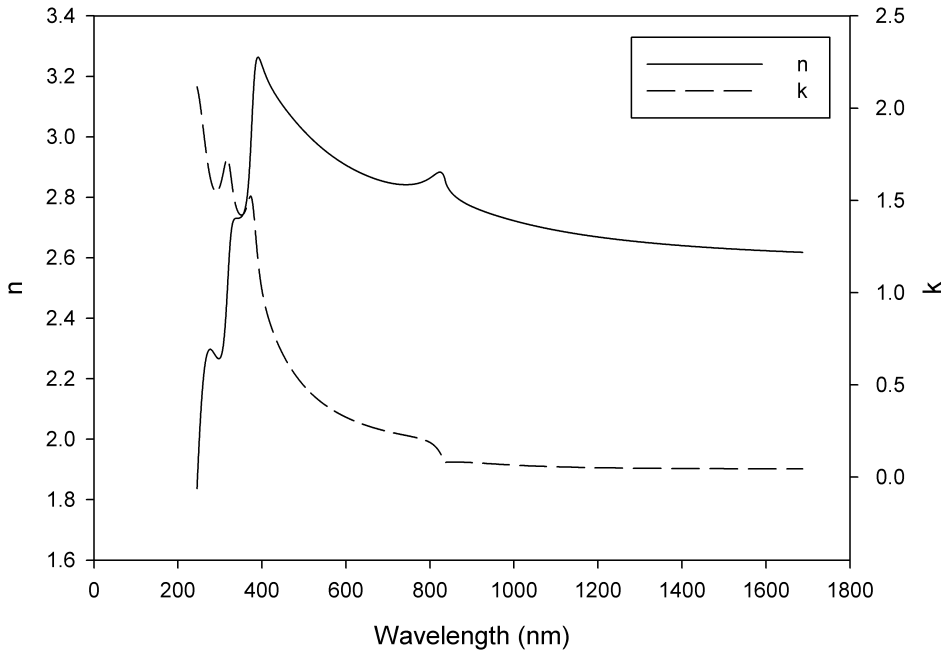

Figure 6-22: Optical constants found for etched CdTe on a silica substrate).

the optical properties of CdS as a result of the annealing process, see figure 6-23. The change in the properties indicated a decrease in the bandgap of the annealed material. The bandgap values calculated from linear extrapolations using the absorption coefficient were $2.515 \pm 0.001\,\text{eV}$ for as-deposited material and $2.420 \pm 0.001\,\text{eV}$ for annealed CdS material. To model the CdS bilayer samples, the optical models for the single layers where stacked on top of each other. EMA layers combining the properties of the layers above and below, were added between different single layers. This improved the quality of the fit, and could possibly simulate the non uniformity of the film thicknesses.

The etched CdS bilayer samples were measured by ellipsometry. The smooth top surface of the samples enabled good quality data to be collected. The samples were modelled by combining the optical properties of the individual layers. An example of the data can be seen in figure 6-24.

The results of the fits can be seen in table 6-4. The ellipsometry analysis of the etched samples was difficult due to the complexity of the sample structures and the limited information. To fit the data only the optical constants of the CdTe, the thicknesses of the EMA and oscillator layers which represented components of the CdS layers, were allowed to vary. The CdTe material being on top of the sample meant that the properties of this

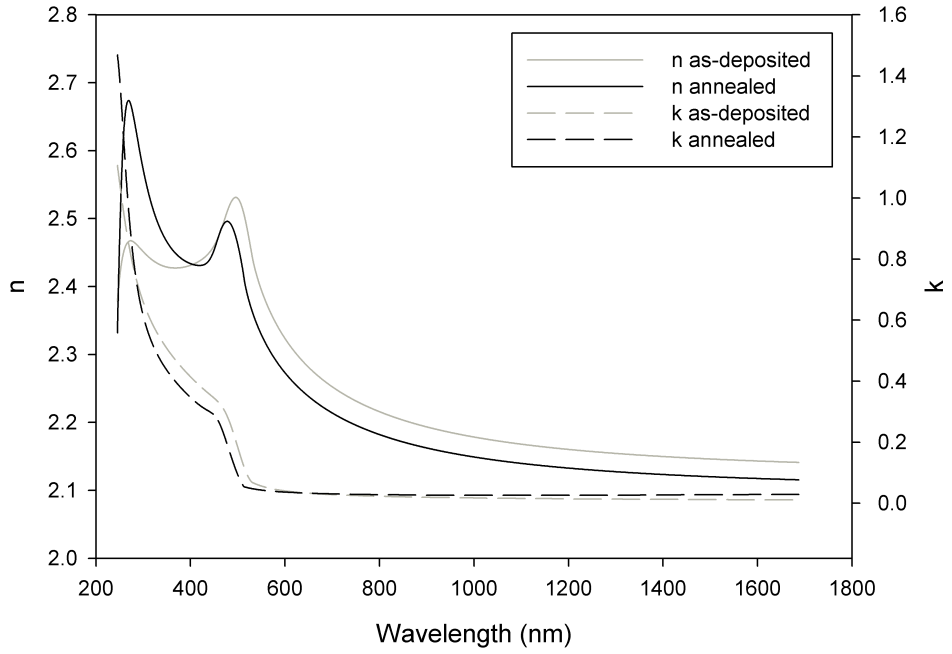

Figure 6-23: The optical constants for annealed and as-deposited CdS films.

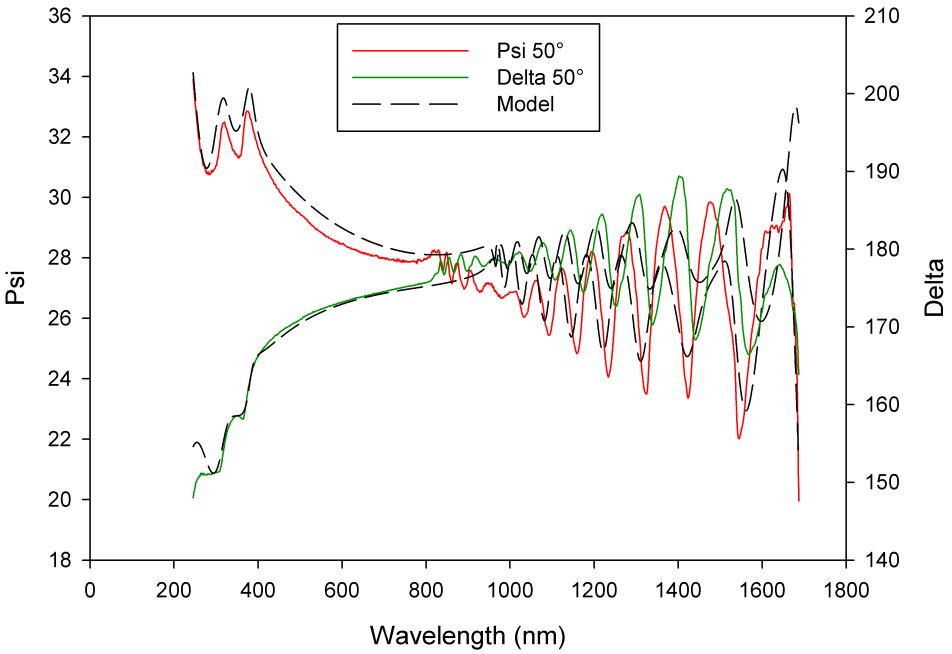

Figure 6-24: The ellipsometry parameters and corresponding model for sample B3 after the 4th etch (structure of CdTe/CdS/Tec 15) for one of the three measurement angles (50, 55 and 60 °)

Table 6-4: Layer thicknesses of the CdS bilayers determined by ellipsometry analysis. Four of the samples could not be modelled accurately (shaded samples).

Sample name	**MSE**	**Total thickness of CdS layers**	**EMA layer thickness**	**CdTe layer thickness**
A3	36	257.8 ± 260.0	22.9 ± 153.8	1768.6 ± 10.4
AA3	49	291.9 ± 150.5	328.6 ± 13.3	3887.6 ± 13.3
AA7	42	466.9 ± 65.3	150.6 ± 15.1	780.1 ± 2.7
B3	44	221.9 ± 17.0	48.3 ± 27.8	2668.8 ± 14.7
B7	35	222.0 ± 4.9	92.2 ± 2.4	663.1 ± 3.6
BA3	77	256.1	514.6	4534.2
BA7	54	414.3	207.6	881.0
C3	27	26.8 ± 21.6	252.6 ± 18.0	3497.5 ± 9.3
C7	50	134.6 ± 7.0	228.1 ± 13.8	1229.6 ± 6.6
CA3	88	443.6	677.8	4229.4
CA7	42	466.9	150.6	780.1

layer of material contributed to the data over the whole wavelength range. Layers below the CdTe only contributed to data in regions were the CdTe was transparent, below its bandgap. During this analysis the four samples with CdS bilayers, which included an annealed CdS layer, could not be accurately modelled. This could demonstrate that these sample structures can not be approximated by simply stacking the properties of the corresponding individual layers on top of each other. Alternatively it may indicate that not enough information about the CdS layers was contained within the data to allow the structure of the two layers to be discriminated. The as-deposited CdS bilayers samples could be modelled and this may be explained by considering these as simpler structures, with both layers having the same optical properties.

6.8 Conclusions

A series of samples demonstrated the fabrication process used in this study was capable of producing samples with consistent electrical properties across all six cells on a sample. The results also indicated that the V_{oc} was limited to 600 mV for all of these devices, which included as-deposited CdS. The measurements showed the recombination current in the depletion region was larger then the recombinations in the quasi neutral region.

As-deposited and annealed CdS were shown to have different d-spacings for the XRD

peak at approximately 26.5° 2θ. These two d-spacings were both observed in the CdS bilayers. This shows these structures contained, as desired, both forms of the CdS. The CdTe was deposited under two different pressures which resulted in two different thicknesses being deposited. This indicates that at least the material deposited under the higher pressure was deposited by a diffusion limited deposition mechanism.

No change in the morphology of the back surface of the CdTe was seen presumably due to the thickness of the CdTe. This result, in conjunction with the consistency of the lattice parameter through the early stages of the destructive treatments, indicates little influence of the substrate on the CdTe material near the back surface. The substrates influence was observed in the difference in the amount of (111) preferred orientation observed in the texture coefficient. Two distinct groups of preferred orientation were observed and with the exception of sample C7, the higher degree of preferred orientation occurred in samples with a CdS bilayer. Assuming that the difference in the preferred orientation was due to the substrate, the observation that the single as-deposited layer in A3 had the lower texture coefficient implies that the difference was not due to the difference between the annealed and as-deposited CdS substrates. One possible explanation is that the CdS grown on CdS has less stress induced in the top film. This reduction of the stress in the top region of the CdS substrate may effect the initial growth orientation within the CdTe film. This assumption is based upon any initial difference in the CdTe growth orientation being continued throughout the whole CdTe film. This explanation could also possibly explain the anomaly of sample C7, assuming a large difference in the effectiveness of the $CdCl_2$ anneal between C7 and C3. If C7 had reduced stress similar to the top of the CdS bilayer, where as C3 may not have under gone a similar reduction in stress within the film. The Williamson Hall plots indicate that as well as there being a difference in the thickness of CdTe deposited at different pressure there might also be a variation in the {hkl} dependence on the strain within the film.

For the spectral response measurements the similar long wavelength absorption edge showed little difference between the samples. This suggested the different treatments had little effect on the devices photoelectric response. The IV parameters show the samples deposited under 3 mbar performed better than those deposited under 7 mbar. The difference in the thickness may mean the fabrication process used in this work was better optimised for the thicker (~11 μm) CdTe. The device fabricated with an annealed

CdS layer showed an increase in the V_{oc} compared to the device with just as-deposited CdS. This showed that the quality of the CdS was contributing toward the maximum limit of the V_{oc} in section 6.2. The I_{02} results of the four samples which included the $CdCl_2$ annealed CdS layers indicated the bilayer samples had higher recombination rate in the depletion region then the single CdS layer samples. It is assumed here that the depletion region is in the vicinity of the interface between the materials. The improvement in I_{02} for the single CdS layered samples is assumed to be due to an improvement in the quality of the CdS due to fewer defects and an increased grain size. The bilayers were expected to form the CdS_xTe_{1-x} alloy more readily than the single CdS layers, and this would improve the electrical properties of the interface. The I_{02} parameters for the C3, C7 CA3 and CA7 samples suggest that bilayers were detrimental to the performance of the devices they were incorporated into.

The similar efficiencies of the individually annealed CdS layers and their corresponding bilayers could suggest the additional layer on the substrate has no beneficial effect on the performance of the device. The texture coefficient analysis clearly indicated a difference in the degree of preferred orientation between the CdTe deposited on the bilayers and CdTe deposited on the single layers, irrespective of the CdTe deposition pressure. This showed that the presence of a bilayer structure does effect the CdTe deposited on top of it. The present study has failed to indicate an advantage to including CdS bilayers into the devices. This may partially be attributed to the large thickness of the as-deposited CdS layer within the bilayer structure, with it being too thick to be significantly consumed through the fabrication process, and so any benefit of additional consumption is suppressed through the presence of additional as-deposited CdS material.

References

[1] X. Wu, J. C. Keane, R. G. Dhere, C. DeHart, D. S. Albin, A. Duda, T. A. Gessert, S. Asher, D. H. Levi, and P. Sheldon, in *17th European Photovoltaic Solar Energy Conference* (2001).

[2] R. Jayakrishnan, S. Kumar, and R. Pandey, Semiconductor Science and Technology **9**, 97 (1994).

[3] C. Guillen, M. A. Martinez, and J. Herrero, Thin Solid Films **335**, 37 (1998).

[4] F. Hasoon, M. Al-Jassim, A. Swartlander, P. Sheldon, A. Al-Douri, and A. Ainajjar, in *26th IEEE Photovoltaic Specialists Conference* (1997), p. 543.

[5] D. W. Lane, Solar Energy Materials and Solar Cells **90**, 1169 (2006).

[6] S. H. Demtsu and J. R. Sites, Thin Solid Films **510**, 320 (2006).

[7] I. O. Oladeji, L. Chow, J. R. Liu, W. K. Chu, A. N. P. Bustamante, C. Fredricksen, and A. F. Schulte, Thin Solid Films **359**, 154 (2000).

[8] R. RamirezBon, N. C. SandovalInda, F. J. EspinozaBeltran, M. SoteloLerma, O. ZelayaAngel, and C. Falcony, Journal of Physics-Condensed Matter **9**, 10051 (1997).

[9] B. Cullity, *Element of x-ray diffraction* (Addison-Wesley Publishing Company, Inc., 1978), 2nd ed.

[10] J. Langford, in *Accuracy in Powder Diffraction II* (1992), p. 110.

[11] K. VonRottkay and M. Rubin, Mater. Res. Soc. Symp. Proc. **426**, 449 (1996).

[12] S. Adachi, T. Kimura, and N. Suzuki, Journal Of Applied Physics **74**, 3435 (1993).

[13] J. Chen, J. Li, D. Sainju, K. D. Wells, N. J. Podraza, and R. W. Collins, Conference Record of The 2006 IEEE 4th World Conference on Photovoltaic Energy Conversion **1**, 475 (2006).

Chapter 7

The effect of surface roughness

7.1 Introduction

CdTe grown by low temperature processes such as electrodeposition is known to undergo recrystallisation during a $CdCl_2$ annealing process. However, CdTe deposited by CSS has been shown not to undergo recrystallisation during a $CdCl_2$ anneal [1]. Hence the as-deposited structure of the CdTe may have a stronger influence on the density of the grain boundaries within a completed device. The $CdCl_2$ treatment is important for the electrical properties of the material and it causes the structure to change by a recovery process involving a reduction in the number of structural defects [1]. Grain boundaries have been linked with carrier recombination processes, although the passivation of some of the effects of boundaries by $CdCl_2$ treatment has been reported [2]. It has been suggested that there is limited scope for increases in the efficiency of devices through increasing the grains size beyond what is commonly reported in the literature [3].

When examining the CdTe deposited earlier in this work, lines of larger grain growth could be seen in the deposited CdTe (see figure 7-1). These lines of increased grain size appeared to be due to scratches on the layers deposited before the CdTe, presumably due to a change in the nucleation of the CdTe in these locations. In this study polishing the transparent conducting oxide (TCO) substrate, was used to increase the density of scratches to investigate if an increase in grain size of the CdTe could be observed.

It has been shown that CdS deposited on roughened Indium Tin Oxide (ITO) had a similar morphology to the underlying ITO layer [4]. The CdS layer in their study was up to 70 nm thick and the ITO was roughened with an HCl etch with a roughness up

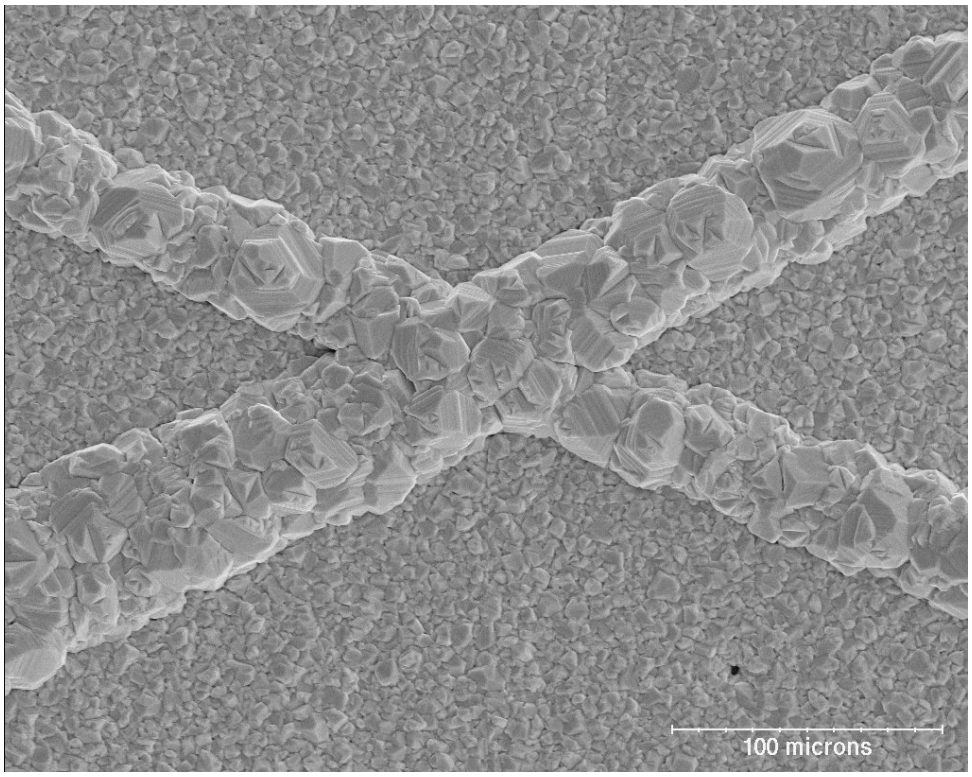

Figure 7-1: In early work lines of increased CdTe grain growth were seen on the back surface of deposited CdTe. It was suggested that this increased grain growth could be the result of unintentional scratches on the substrate. The scale bar indicates 100 μm.

to 45 nm. Work by Oliva *et al.* [5] showed that the substrate influences the roughness of a CdS layer grown on top by chemical bath deposition. Their work suggested the roughness of CdS grown on non-roughened ITO was constant for different deposition times and similar to the roughness of the original ITO. In the present work we tested whether scratches on the TCO surface could be transferred through to the surface of the CdS, and what effect they would have on the CdTe deposited on top.

7.2 Preliminary results

To test the hypothesis that scratches on the TCO surface cause an increase in grain growth some Pilkington Tec 15 substrates were hand-polished with several different types of SiC paper. The substrates were polished with a pressure spread as evenly as possible across the sample while water was used as a lubricant. For the initial test three different SiC papers were used, the grain sizes of the papers were: 5, 8 and 15 μm. After the TCOs had been polished CdTe was deposited directly onto the sample surfaces, with a deposition

time of 25 min, after the substrate lamps had warmed up for 10 min.

Scanning electron microscopy (SEM) images of the deposited material showed that the CdTe did not uniformly cover the TCO. Dark lines could be seen across the image on some of the samples believed to be due to deep scratches, where less material seems to have been deposited. These larger scratches were more apparent for the samples polished with SiC paper with the two larger grain sizes.

For the samples polished with the 5 µm grain size SiC paper the nucleation of the growth can be seen to be affected by the substrate, see figure 7-2. The SEM image shows some CdTe grains growing in lines which are believed to correspond to the scratches on the surface of the TCO.

The deposited CdTe was analysed by XRD (20° to 80° 2θ) and the results showed very little variation between the deposited materials. The average texture coefficient was calculated to be 0.27 ± 0.03 with the preferred orientation along the (111) direction (for a random orientation it would equal 0, for 7 peaks perfectly aligned along one orientation it would equal 2.4). The average lattice parameter was calculated to be 0.6493 ± 0.0017 nm. While the Williamson Hall plots showed a possible {hkl} dependence with the (400) and

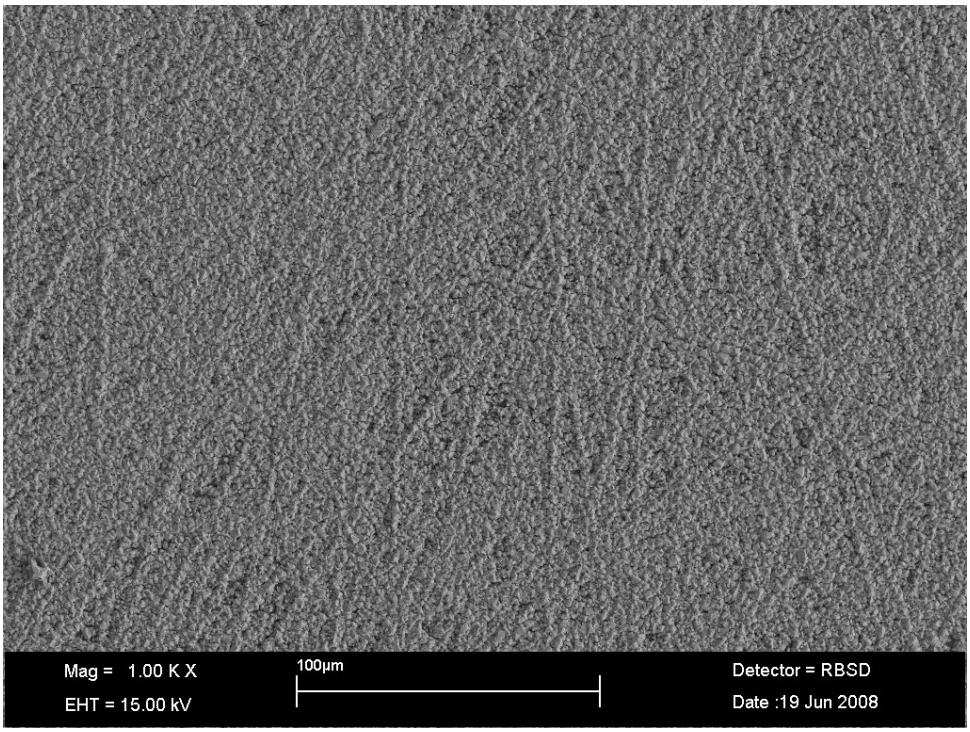

Figure 7-2: SEM image of CdTe deposited directly on a TCO substrate, which had been hand polished using 5 µm grain size SiC paper. CdTe growth along scratches on the TCO layer can be seen from the image. The scale bar in the image represents 100 µm.

(511) directions showing different amounts of strain (see figure 7-3).

The preliminary results confirm that roughening the substrate can effect the material deposited on top. The polishing procedure used in this section was not very reproducible and so further investigation using a more automated procedure which is discussed below.

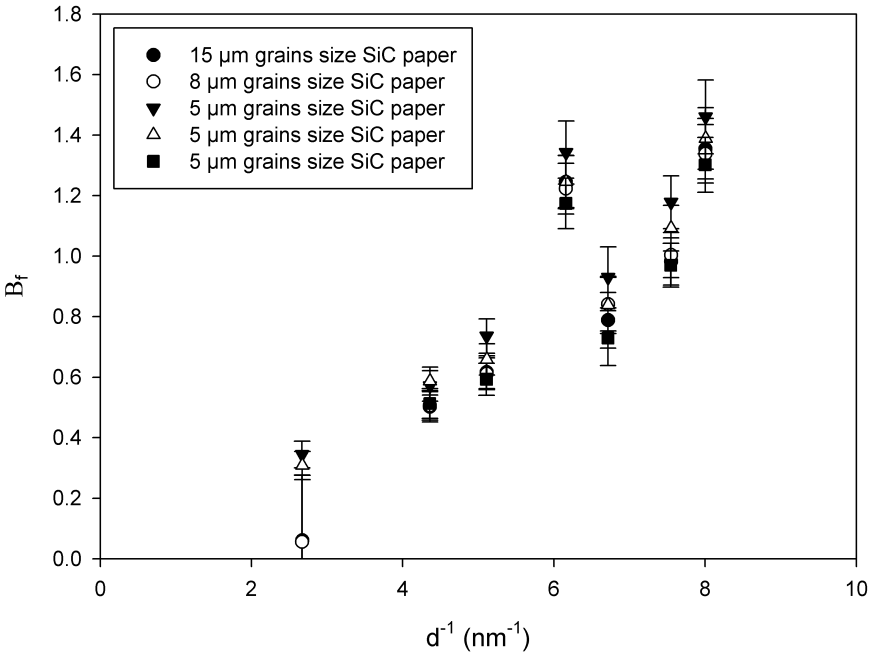

Figure 7-3: Williamson Hall plot of CdTe deposited directly onto roughened TCO. A possible hkl dependence can be seen for the peaks corresponding to d^{-1} equal to 6.2 and 8.0 nm^{-1}.

7.3 Polishing the TCO

To increase the reproducibility of the mechanical polishing the Tec 15 samples were mounted on discs so that they could be loaded into a Stuers RotoPol-15 polisher. This allowed the parameter for the polishing to be set: rotation rate (150 rpm), force (25 N) and time (30 or 60 seconds). Three different grain sizes of abrasive material were used and compared to un-polished samples. The most abrasive polishing used a SiC paper with a 5 µm grain size. Abrasive diamond suspensions with 3 µm and 1 µm grain size were also used with their appropriate polishing pads (MD-Dac and MD-Nap respectively used with green/blue lubricant). Two polishing times were used although no difference in the results for different polishing times was noticed so the two samples are reported

as having the same treatment. After polishing, the samples were thoroughly washed in acetone, CdS and then CdTe layers were then deposited.

The TCO layer on the Tec 15 substrates was roughened with the three different polishing procedures to produce different degrees of scratching on the surface. The Tec 15 glass is reported to have an approximately 300 nm thick multilayered conducting structure [6]. The polishing process could potentially increase the resistance of this layer structure by either reducing its thickness or introducing scratches that cut through its entire thickness. Consequently, the effect of polishing on the resistance of the Tec 15 glass was investigated using a four point probe.

The sheet resistances of the polished samples were found to be higher than the un-polished samples, although the change was small. A change from 13.9 Ω/□ for the un-polished samples to 15.5 Ω/□ for both the samples polished with 5 μm grain size SiC paper and 1 μm diamond suspension was observed. Samples polished with the 3 μm diamond suspension produced a slightly greater change in the resistance which rose to 16.9 Ω/□, a rise of approximately 3.0 Ω/□. There is currently no explanation of why the 3 μm suspension changes the resistance by a larger value than the 5 μm grain size SiC paper. Although it was noted that the polishing techniques were different with one being an abrasive paper with water lubricant, and the other being an abrasive suspension with a polishing pad which might produce different polishing effects. These changes in the resistance were small and so the current methods for increasing the roughness of the TCOs could be implemented in the production of solar cells, without degrading the electrical performance of the cells. It is desired that the roughening produces an increase in the performance of the device which is significant enough to warrant the additional complications in the fabrication process.

SEM images of the roughened TCO surface showed an increase in the number of scratches in the samples polished with the SiC paper (see figure 7-4) and the 3 μm diamond suspension compared with the un-polished samples. Occasional scratches were observed on the un-polished and polished with a 1 μm diamond suspension samples. The un-polished samples were easier to focus on during the SEM analysis than the samples polished with the 1 μm suspension. A possible explanation might be that the samples polished with the 1 μm suspension may have smoother surfaces than the samples which have not been polished.

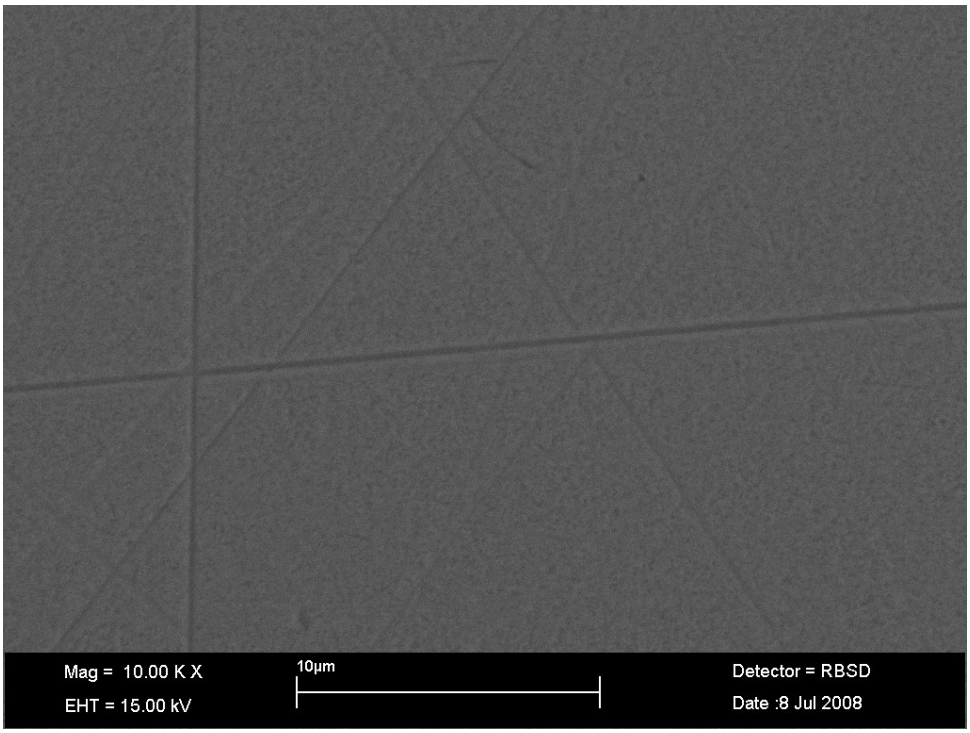

Figure 7-4: SEM image of TCO polished with 5 µm grain size SiC paper. The scale bar in the image represents 10 µm.

Attempts to measure the surface roughness of the TCO using an Alpha step surface profiler showed inconsistency between the measurements. This inconsistency is believed to be due to the non-uniformity of the polishing. The average root mean squared (rms) value calculated from the measurements for the roughness of the substrates is of the order of 19 nm. Occasional scratches on the un-polished samples skewed the rms value. Similarly for the samples polished with the 5 µm SiC paper a few scratches 150 nm deep were observed. These large scratches would reduce the thickness of the SnO_2 layer in the TCO to approximately half of its original 300 nm thickness.

7.4 CdS layers on roughened TCO

CdS was deposited on the roughened TCO by CBD. XRD analysis of the reflection at approximately 26.5 ° 2θ, fitted two peaks to the data where the low angle peak was assigned to the TCO (26.49 °) and the high angle peak to a CdS peak (26.81 °), this is similar to the as deposited material observed in section 6.4. Small variations in the intensities of the CdS peaks were observed and could be due to changes in the thickness of the CdS layers or changes in the preferred orientation. Alpha step surface profiler

measurements showed the CdS to be approximately 185 nm thick. No variation in the position of the fitted CdS peak was observed. This would suggest that any uniform strain in the CdS layer along this crystallographic direction is consistent and therefore independent of the roughness of the substrate.

SEM images of the CdS showed that scratches from the TCO layer could still be seen, see figure 7-5. This is not unexpected as the CdS layer is relatively thin and it shows that roughening the TCO layer allows a way of modifying the substrate for the CdTe deposition. This is comparatively easier than roughening the CdS layer.

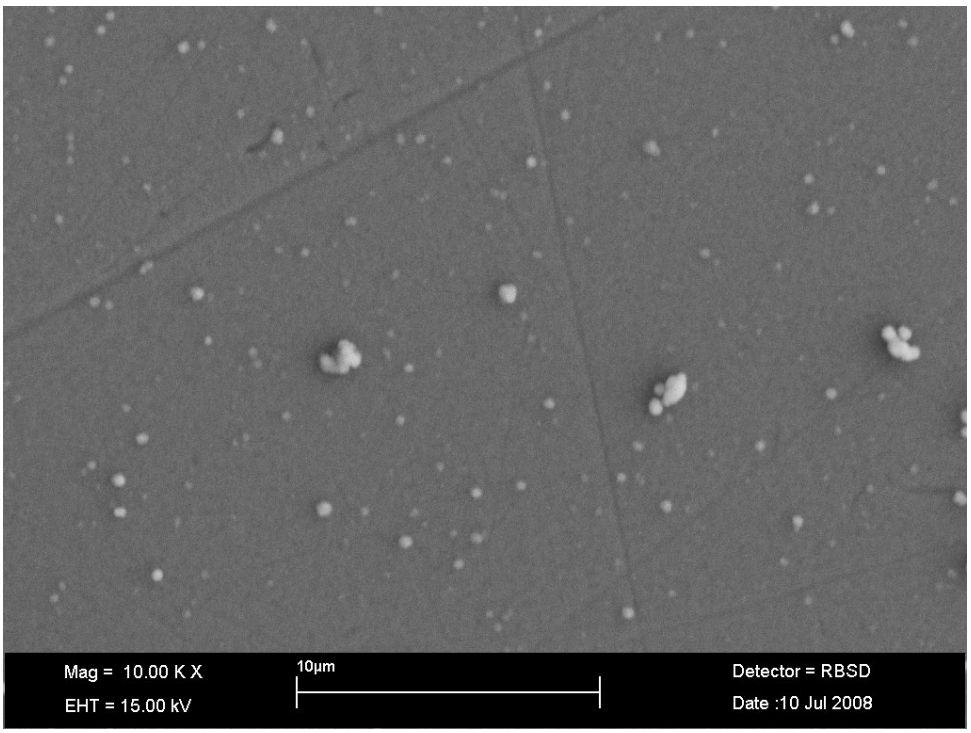

Figure 7-5: SEM image of CdS deposited on TCO polished with 5 µm grain size SiC paper. A similar surface texture can be seen to the just polished TCO. Particles of CdS can be seen on the surface. The scale bar in the image represents 10 µm.

7.5 CdTe layers on CdS/roughened substrates

CdTe was deposited in an environment of oxygen (0.2 l/min) and argon (1.8 l/min) producing a chamber pressure of 9 mbar. XRD analysis was carried out over the 2θ range of 20° to 110° with the smaller angular step size of 0.005° by the continuous measurement technique. The XRD measurements covering 11 CdTe reflections were all fitted with two phases apart from the 1^{st} reflection.

The thickness of the CdTe layers deposited on the CdS/roughened TCO was calculated from RBS measurements by assuming stoichiometric CdTe. The average value for the samples was 1350 nm. No variation in the grains of the CdTe could be observed between SEM images of the samples (not shown). Also of significance was the uniformity of the grain sizes. No lines of large grains could be seen on the deposited CdTe, which was expected to be similar to that observed for the CdTe deposited on the roughened TCO (section 7.2).

The CdTe deposited throughout this work consistently had a (111) preferred orientation with 11 reflections observed over the measurement range. As previously mentioned all reflections were fitted with two peaks due to asymmetry apart from the first peak (111). To calculate the amount of preferred orientation in the samples on the roughened substrates the texture coefficient were calculated for all 11 reflections. The intensities of the reflections were used to calculate the texture coefficient, this is not equivalent to using the combined maximum intensities of the two fitted phases, but is equivalent to the maximum of the superposition of the phases.

The results indicate that the 1 μm suspension polished samples had a greater degree of preferred orientation than the un-polished samples, see figure 7-6. The texture coefficient decreases with an increase in the grain size of the abrasive material used. The larger amount of preferred orientation for the samples polished with 1 μm diamond suspension compared to the un-polished samples may agree with one of the suggestions from SEM analysis, of the 1 μm polished samples having a smoother surface than the non polished samples. This assumes the increase in the preferred orientation is linked with the roughness of the substrate.

The Taylor Nelson plot was used to determine the lattice parameter for each phase. The lattice parameter for the 1^{st} phase did not seem to vary with roughness, see figure 7-7. The 2^{nd} phase lattice parameter did appear to increase as the substrates became smoother. The lattice parameter for stoichiometric CdTe was found to be 0.64921 ± 0.00045 nm by Wood *et al.* [7]. This is comparable with the parameter found for the 1st phase. For the second phase the sample polished with 5 μm grain size SiC paper had an average lattice parameter of 0.6471 ± 0.0002 nm. If this lattice parameter was caused soley by the formation of a CdS_xTe_{1-x} alloy then by using Vergards law the stoichiometry of the alloy could be calculated. Using the Vergards coefficients from work by Wood et al,

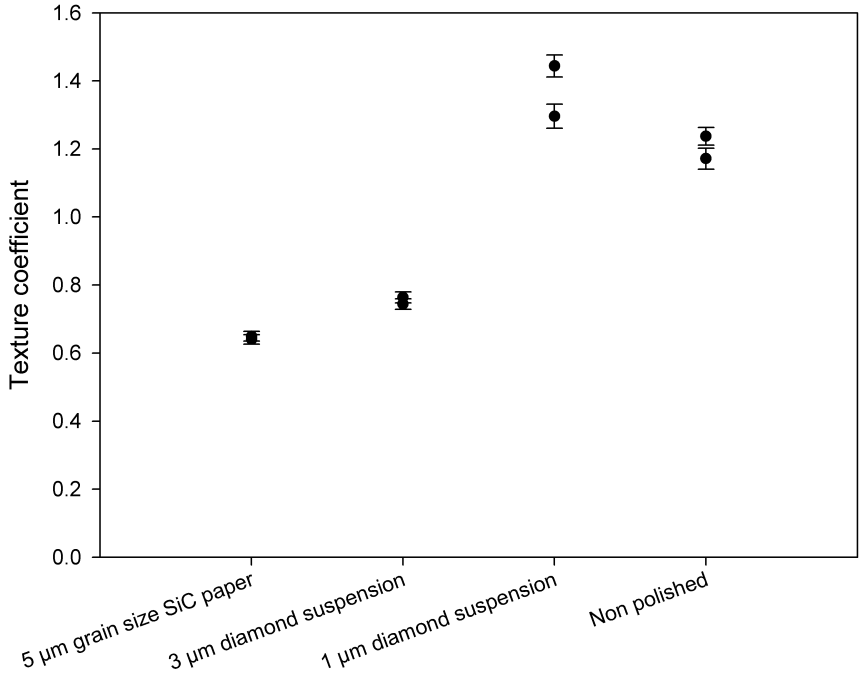

Figure 7-6: The texture coefficient calculated from the intensities of the 11 reflections for the CdTe material deposited on roughened substrates. A value equal to 0 would indicate a randomly oriented material where as a value of 3.2 would mean the CdTe is perfectly oriented along one direction.

this lattice parameter would suggest that stoichiometry of the alloy formed would be $CdS_{0.029}Te_{0.971}$. It should be noted that the largest variation in the lattice parameter was used to obtain this stoichiometric value. It has been shown that this alloy should form a zincblende structure which would agree with the XRD data [7]. This allows all or some of the uniform strain which causes the change in the lattice parameters to be caused by the stoichiometry of the material.

The Williamson Hall plots for the two phases shows that each phase clearly has a different amount of strain (10 peaks are plotted and the results do not include the (111) peak due to the reason discussed earlier), see figure 7-8. The results showed the 2^{nd} phase for all the samples had a larger amount of strain than the first phase. The linear regression fits to the second phase indicate that for the samples polished with the 5 µm SiC paper and the 3 µm diamond suspension the intercept is approximately zero. This would indicate the peak broadening due to the size of the crystallite in the material is small. However some of the 2^{nd} phase data from samples which were not polished, or

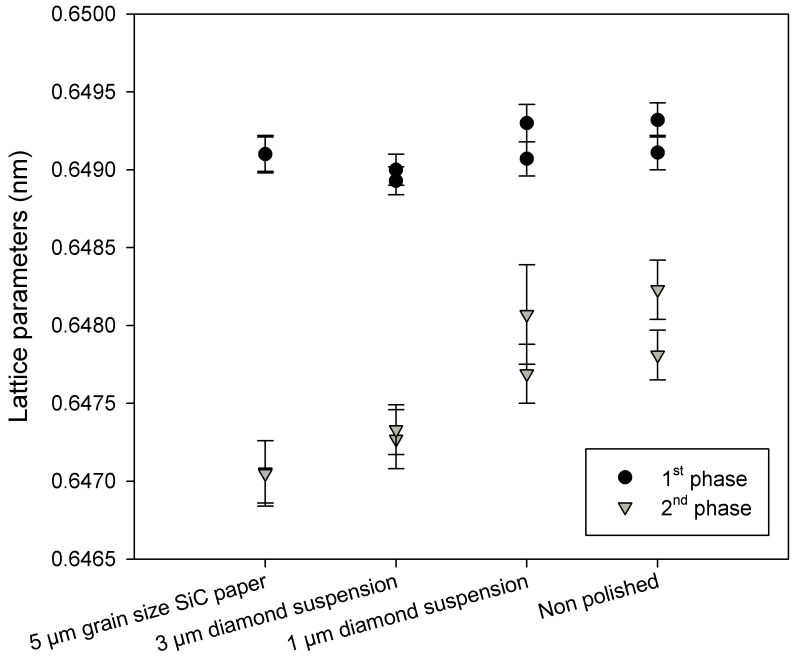

Figure 7-7: The lattice parameters obtained from Taylor Nelson plots of 10 peaks for the 1^{st} and 2^{nd} phases.

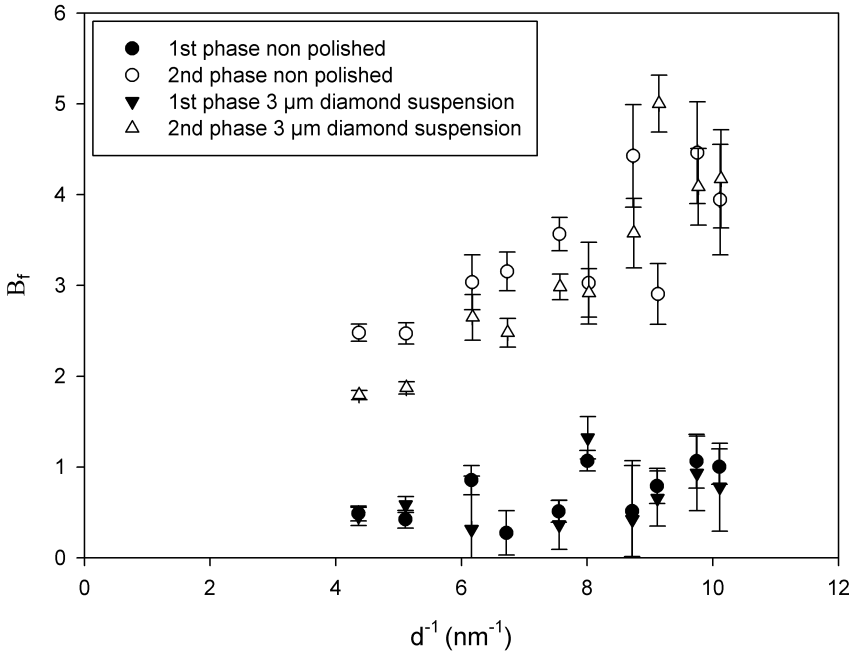

Figure 7-8: Williamson Hall plot of the two phases in two samples. A clear difference can be seen in the amount of strain present in the two phases.

were polished with 1 μm diamond suspension, fitted with a non zero intercept, suggesting a crystallite size component was contributing towards the strain.

The {hkl} dependence seen for the CdTe deposited directly onto the roughened TCO (figure 7-3) is not as apparent in the current samples (figure 7-8). For the 1^{st} phase the peak with a d^{-1} equal to approximately 8.0 nm^{-1} (the 511 direction) still appears to have a distinctly different strain affecting this direction. The peaks at d^{-1} equal to approximately 6.2 nm^{-1} (the 400 direction) do not have the same sign of an {hkl} dependence as they did for the CdTe deposited directly on to the roughened TCO.

7.6 Conclusions

The preliminary results where CdTe was deposited directly onto roughened TCO appears to show lines of CdTe grains. The depositions show the scratches on the surface of the TCO affect the nucleation of the CdTe. It has been assumed that these lines of grains correspond to scratches on the TCO surface. The SEM images also imply the films are thin, and this may have contributed towards the lack of variation in the grain sizes of the CdTe.

The auto polishing of the TCO was shown to affect the sheet resistivity. It should be possible, by adjusting the initial thicknesses of the deposited TCO layers, to minimise the change in the resistivity for a fabrication process involving a polishing step.

SEM images of the TCO polished with 5 and 3 μm suspension, and of the CdS deposited on top, showed it is possible to produce a CdS layer with a similar morphology to the roughened TCO layer. This indicates the potential of using polishing as a technique to vary the morphology of the CdTe substrate surface.

The XRD analysis has suggested the presence of two phases within the CdTe material. Two phases within the CdTe were only observed in material deposited on CdS. The preliminary study (section 7.2) and the material deposited under different pressures (section 5.8), both deposited directly onto the TCO did not indicate the presence of two phases. This supports the suggestion that the 2^{nd} phase is the result of the formation of a CdS_xTe_{1-x} alloy.

The change in the preferred orientation of the CdTe reflections may be linked to the different polishing techniques used. No information has been determined about the rela-

tive abundance of the two phases within the material. Information about the abundance of the second phase may help explain the texture coefficient results, if we assume the second phase forms with a random orientation. Since the texture coefficient calculation in this work used the reflection intensities the relative abundance of the two materials would affect the texture coefficient. Hence, assuming the 1^{st} phase has a (111) preferred orientation and the second phase has a random preferred orientation. The texture coefficient could be explained if the abundance of the second phase increased as the roughness of the substrate is increased. This explanation also assumes that the samples polished with the 1 µm diamond suspension are smoother than the un-polished samples. The relative d-spacings of the two phases also needs to be considered when explaining the relative preferred orientation of the CdTe reflections.

The variation of the lattice parameters of the second phase would suggest that different compositions of the CdS_xTe_{1-x} alloy formed on the different samples. With the amount of sulphur within the CdS_xTe_{1-x} alloy increasing with the increasing grain size of the abrasive material. The explanation of why this would occur is unclear, but it may be linked with the change in the nucleation of the CdTe.

The Williamson Hall plots show a larger gradient for the 2^{nd} phase compared to the 1^{st}. This indicates a larger strain which may be due to several factors including a gradient in the composition or a large amount of defects within the material. Any {hkl} dependence of the strain for either phase of the material is not as clear as it has been in other chapters. This is an indication of a difference strain with this material compared to the CdTe deposited on non polished TCO.

The CdTe deposited on the CdS did not have the same observed effect as seen with the CdTe on the TCO. This may have resulted from the CdTe deposited on the TCO being thinner and so the effect of the substrate is more observable on the back surface of CdTe. If this were true, then since a similar morphology was observed for the CdS on the TCO, it may be suggested that a similar process may occur for CdTe close to the CdS interface. The poor quality of CdS may have also caused the effect on the nucleation sites to be reduced due to polishing, due to the high number of particles seen on the CdS layers.

References

[1] H. Moutinho, M. Al-Jassim, F. Abufoltuh, D. Levi, P. Dippo, R. Dhere, and L. Kazmerski, in *26th IEEE Photovaltaic Specialists Conference* (1997).

[2] L. Woods, G. Robinson, and D. Levi, in *28th IEEE Photovoltaic Specialists Conference* (2000), p. 603.

[3] K. Durose, D. Boyle, A. Abken, C. J. Ottley, P. Nollet, S. Degrave, M. Burgelman, R. Wendt, J. Beier, and D. Bonnet, Physica Status Solidi B-Basic Research **229**, 1055 (2002).

[4] A. Martel, F. Caballero-Briones, A. I. Oliva, R. Castro-Rodriguez, A. Iribarren, P. Bartolo-Perez, and J. L. Pena, Physica Status Solidi B-Basic Research **220**, 261 (2000).

[5] A. I. Oliva, R. Castro-Rodriguez, O. Ceh, P. Bartolo-Perez, F. Caballero-Briones, and V. Sosa, Applied Surface Science **148**, 42 (1999).

[6] K. VonRottkay and M. Rubin, Mater. Res. Soc. Symp. Proc. **426**, 449 (1996).

[7] D. A. Wood, K. D. Rogers, D. W. Lane, G. J. Conibeer, and D. Parton, Journal of materials science letters **17**, 1511 (1998).

Chapter 8

Conclusions and future work

8.1 Conclusions

This work has focused on the construction and development of a CSS system for CdTe deposition. In addition, it has also focused on variations to the treatment and fabrication procedures of the TCO and CdS layers before the CdTe deposition, in order to influence the structure and electrical properties of the CdTe/CdS interface.

CBD is widely used for the growth of CdS layers in thin film solar cells. While this technique can produce uniform high quality films, it suffers from a poorly defined growth starting point. This has a negative affect on process control. In this study the CBD deposition has been monitored via an in situ optical fibre technique. A simple expression for the interface at the end of the fibre predicted the change in the reflectance for different thicknesses of film. This model assumed the optical properties of the solution to be equivalent to those of water, this was investigated and found to be valid. Results for longer deposition times consistently showed two regions of growth rate in agreement with the concept of two different mechanisms dominating during different periods of the CBD process, as suggested in the literature by Lincot and Borges [1]. The fibre optic monitoring technique seems well suited to monitor short depositions of thin films (less than 100 nm), with the starting point of the reaction being easily identifiable. The industrial application of the technique would allow far greater process control over the deposition of these thin layers, improving the yield of the manufacturing process and minimising waste. Both the change in the thickness of the film with time, observed using the optical fibre, and the model used in ellipsometry analysis have indicated the dominance of two different

growth mechanisms and a resulting two layer structure. This was clearly demonstrated by the ellipsometry data as an additional porous layer of CdS was necessary on top of a dense layer to fit both the ellipsometry and transmission data. This corresponds to a layer produced by homogeneous growth on top of a dense layer produced by ion by ion deposition.

A piece of equipment to deposit CdTe by CSS has been built as part of this study. It has been shown that in this equipment, the start and finish points of the deposition could be controlled using the heating profiles of the source and substrate. The CdTe source material has been shown to become Cd rich after several repeat depositions and this may be linked with an imbalance in the partial pressure of the Cd and Te_2 gases ($p_{Cd} \neq 2p_{Te_2}$). Samples deposited under different deposition pressures indicated a change in the percentage of tellurium incorporated into the deposited film, in agreement with the work by Romeo *et al.* [2]. These samples also indicated an increase in the texture coefficient and strain within the material with decreasing deposition pressure. This was attributed to a faster growth rate causing the faster growing (111) crystallographic direction to dominate, while incorporating an increased number of structural defects. The influence of the substrate temperature and the composition of the environment (i.e. Ar/O_2) were found to be consistent with what other groups have reported in the literature. CdTe deposited using the CSS equipment at Durham University showed similar texture coefficients and levels of strain within the material. This suggests that CdTe CSS growth procedure can be readily transferred from one set of equipment to another, and that the results presented in this thesis can be compared with confidence to those presented else where.

The device fabrication process was shown to be capable of producing six cells across a sample that had consistent electrical properties, and this enabled comparisons of the electrical and structural properties of the samples. CdS bilayer films were successfully deposited by a two stage deposition process and the presence of annealed and as-deposited material was confirmed by XRD measurements. CdTe layers were deposited at one of two deposition pressures. The IV measurements showed that thicker CdTe deposited under 3 mbar of pressure had better electrical properties (for examples higher efficiencies) compared to the thinner material. The I_{02} parameters indicated the annealed CdS single layers had less recombination in the depletion region than the equivalent bilayer samples. The texture coefficient of the CdTe was larger for the material deposited on the bilayers

than the material deposited on the single layers of CdS. This showed that the nature of the underlying CdS influences the preferred orientation of the entire CdTe layer deposited on top. However the reason for this remains uncertain. This could be caused by a reduction in the stress at the top surface of the CdS bilayers, and may simply result from the greater CdS thickness in these samples. The Williamson Hall plots indicated a difference in the {hkl} dependence of the strain for the material deposited under the two pressures.

Preliminary results indicated a possible way of affecting the grain size of as-deposited CdTe material by roughening the TCO. In this study roughening the TCO substrate has been shown to effect the nucleation of CdTe deposited on it. The presence of a 2^{nd} phase of material assigned to a CdS_xTe_{1-x}, alloy has been shown to vary depending on the grain size of the abrasive material used to polish the TCO. The abundance of the second phase is not known from the measurements made in this study. However the amount of sulphur within the second phase has been suggested to increase with increasing grain size of the abrasive material used to polish the TCO.

8.2 Future work

Although the CdS bilayers in this study did not demonstrate a benefit to the performance of the devices, it would be interesting to investigate the effect on the electrical and structural properties by varying the ratio of the thicknesses of the two layers within a bilayer. This could be done by varying the CBD parameters for the two layers whilst keeping the overall combined thickness of the CdS bilayers constant. If the first layer was $CdCl_2$ annealed, then as the thickness of the as-deposited CdS material within the bilayer was reduced, the performance of the device would be expected to improve steadily depending on the amount of as-deposited CdS incorporated. The proposed point of interest would be whether as the ratio of the two layer thicknesses were changed there was a point where the parameters of the device would improve above the expected trend.

To gain more information about the effect roughening the TCO substrate has on the CdTe/CdS material the abundance of the 2^{nd} phase within the material could be determined. This information may be obtained from combining XRD with RBS measurements on samples which could be successively etched. This would hopefully enable an understanding of how the degree of roughening effects the composition and the quantity of the

alloy formed. Electrical characteristic measurements of devices which included roughened TCO were attempted in the present work, but inconsistencies in the measurements prevented conclusions from being drawn and the results were not discussed here. However the roughening of the TCO has been shown to affect the resulting composition of the device and this would be expected to affect the electrical characteristics. The effect of the roughening process on the optical properties of the device could also be investigated and this would need to be considered when evaluating the effect of the roughening on the electrical properties of the devices.

The reasons for the used CdTe source material becoming Cd rich could be investigated through depositing a series of samples under different pressures. A small amount of new source material could be used for each deposition and its composition could be measured after the procedure. The used source material could also be examined by XRD to try and detect the presence of a second phase within the material.

The CSS system could be modified to enable it to be used to convert metal alloys into semiconductors via the process of sulphurisation. The graphite blocks used to support the sample and source material would require modification and the spacing between the blocks would need to be increased. However the remainder of the equipment would be suited to this application. The equipment would allow the evaporation of sulphur onto the surface of a metal alloy sample. The metal alloy could then be heated to allow a reaction with sulphur on the surface to occur.

References

[1] D. Lincot and R. O. Borges, Journal of The Electrochemical Society **139**, 1880 (1992).

[2] N. Romeo, R. Tedeschi, S. Pasquali, L. Ferrari, A. Bosio, V. Canevari, and R. Alfieri, in *16th European Photovoltaic Solar Energy Conference* (2000), vol. 1, p. 812.

Appendix A

A.1 Layer thickness calculation for Rutherford backscattering spectrometry

The thickness of the material layers within a RBS model were given in thin film units, 1 $\times 10^{15}$ atoms cm^{-2}. The following process can be used to convert the units to nanometers.

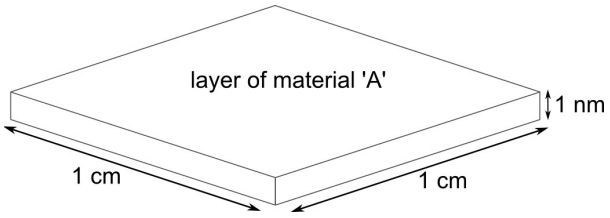

Figure A-1:

For a film 1 × 1 cm and 1 nm, the volume of the film = 1 $\times 10^{-7}$ cm^{-3}. The mass of a layer of 'A' atoms (with the dimensions in figure A-1), with a density ρ_A, is given by, ρ_A × 1 $\times 10^{-7}$ cm^{-3}. If the molecular mass of 'A' equals M_A, then the fraction of a mole of material 'A' in the layer = $\frac{\rho_A \times 1 \times 10^{-7}}{M_A}$. The number of atoms ($n_{atom}$) of 'A', in the layer can then be found by multiplying molar fraction of the material by Avogadro's number (N_A) and the number of atoms in a molecule of 'A' (n_A):

$$n_{atom} = \frac{\rho_A \times 1 \times 10^{-7}}{M_A} \times N_A \times n_A \qquad \text{(A-1)}$$

This is the number of atoms of material 'A' cm^{-2} in a 1 nm thick layer, and so can be used to convert the thickness of the layer in thin film units into nanometers.

A.2 Ellipsometry models

A Cauchy oscillator was used to model silica substrates and it produced a good fit with an MSE of 1.62.

Table A-1: Cauchy oscillator parameters used for silica substrates.

Substrate				**thickness**	**4.0 mm**
Oscillator	**Cauchy**				
A =	1.446	B =	0.00385	C =	0.00001
k amplitude =	0.0000	Exponent =	0.000	Band edge =	400.0 nm

A model of as-deposited CdS where a single layer was used to represent the CdS.

Table A-2: A model with a single Gen-Osc layer, used to represent the CdS layer.

Roughness	**= 37.15 nm**				
Gen-Osc layer				**thickness**	**126.01 nm**
E_∞ =	0.683				
Oscillator	**Cody-Lorentz**				
Amp =	42.730				
B_r =	15.519	E_0 =	10.974	E_g =	2.316
E_p =	0.189	E_t =	0.020	E_u =	15.000
Oscillator	**Lorentz**				
Amp =	0.175358	B_r =	0.1944	E_n =	2.645
Oscillator	**Lorentz**				
Amp =	3.658629	B_r =	0.8779	E_n =	4.619
Substrate				**thickness**	**4.0 mm**

A model of as-deposited CdS, with two model layers representing the CdS.

Table A-3: A model with a Gen-Osc and EMA layer, used to represent the CdS layer.

Roughness	**= 26.52 nm**				
EMA layer				**thickness**	**46.37 nm**
Material 1 =	Void				
Material 2 =	Coupled	+ layer 1			
EMA % =	74.7	Depolarization =	0.000	Anaylsis Mode =	Bruggeman
Gen-Osc layer				**thickness**	**84.32 nm**
E_∞ =	0.024				
Oscillator	**Cody-Lorentz**				
Amp =	51.670				
B_r =	15.470	E_0 =	11.065	E_g =	2.322
E_p =	0.239	E_t =	0.013	E_u =	15.000
Oscillator	**Lorentz**				
Amp =	0.383396	B_r =	0.4513	E_n =	2.588
Oscillator	**Lorentz**				
Amp =	2.506262	B_r =	1.5977	E_n =	5.287
Substrate				**thickness**	**4.0 mm**

Table A-4: The multilayered model used to represent Nippon TCO glass, for the wavelength range 245 to 1200 nm.

Roughness	**= off**				
Gen-Osc layer				**thickness**	**32.00 nm**
E_∞ =	0.937				
Oscillator	**Lorentz**				
Amp =	0.860005	B_r =	1.0770	E_n =	4.950
Oscillator	**Pole**				
Amp =	57.6526	E_n =	7.585		
EMA layer				**thickness**	**24.41 nm**
Material 1 =	Coupled	+ layer 5			
Material 2 =	Coupled	+ layer 3			
EMA % =	86.1	Depolarization =	0.000	Anaylsis Mode =	Linear
Gen-Osc layer				**thickness**	**332.15 nm**
E_∞ =	2.226				
Oscillator	**Cody-Lorentz**				
Amp =	6.994				
B_r =	0.600	E_0 =	4.773	E_g =	2.368
E_p =	7.927	E_t =	1.529	E_u =	6.580
Oscillator	**Drude(RT)**				
Resistivity =	0.000359	Scat. Time =	7.496		
Oscillator	**Pole**				
Amp =	60.5306	E_n =	6.715		
SiO_2				**thickness**	**123.64 nm**
Gen-Osc layer				**thickness**	**20.55 nm**
E_∞ =	0.000				
Oscillator	**Pole**				
Amp =	199.7436	E_n =	9.037		
Oscillator	**Harmonic**				
Amp =	360.106285	B_r =	0.2612	E_n =	0.023
Cauchy					

Table A-5: The multilayered model used to represent Tec 15 TCO glass.

Roughness	**= off**				
Gen-Osc layer				**thickness**	**25.30 nm**
E_∞ =	1.328				
Oscillator	**Lorentz**				
Amp =	0.240448	B_r =	0.8588	E_n =	3.600
Oscillator	**Pole**				
Amp =	58.3364	E_n =	7.844		
EMA layer				**thickness**	**32.41 nm**
Material 1 =	Coupled	+ layer 5			
Material 2 =	Coupled	+ layer 3			
EMA % =	79.3	Depolarization =	0.520	Anaylsis Mode =	Bruggeman
Gen-Osc layer				**thickness**	**254.13 nm**
E_∞ =	2.015				
Oscillator	**Cody-Lorentz**				
Amp =	2.502				
B_r =	0.922	E_0 =	4.823	E_g =	3.376
E_p =	1.700	E_t =	0.502	E_u =	0.549
Oscillator	**Drude(RT)**				
Resistivity =	0.000402	Scat. Time =	5.715		
Oscillator	**Pole**				
Amp =	81.2310	E_n =	6.653		
SiO_2				**thickness**	**1.86 nm**
Gen-Osc layer				**thickness**	**62.76 nm**
E_∞ =	2.868				
Oscillator	**Pole**				
Amp =	11.7418	E_n =	5.382		
Oscillator	**Harmonic**				
Amp =	0.827012	B_r =	0.3304	E_n =	0.894
Cauchy					

Table A-6: A model with a Gen-Osc and EMA layer, used to represent an etched CdTe layer on a silica substrate.

Roughness	**= off**				
Gen-Osc layer				**thickness**	**2135.61 nm**
E_∞ =	0.963				
Oscillator	**Cody-Lorentz**				
Amp =	9.272				
B_r =	1.803	E_0 =	3.509	E_g =	1.474
E_p =	0.029	E_t =	0.009	E_u =	15.000
Oscillator	**Lorentz**				
Amp =	0.176056	B_r =	0.4821	E_n =	1.487
Oscillator	**Lorentz**				
Amp =	2.9985641	B_r =	0.2609	E_n =	3.283
Oscillator	**Lorentz**				
Amp =	3.224465	B_r =	0.4539	E_n =	3.872
Oscillator	**Lorentz**				
Amp =	13.355812	B_r =	1.1178	E_n =	5.515
EMA layer				**thickness**	**162.24 nm**
Material 1 =	Coupled	+ layer 2			
Material 2 =	Void				
EMA % =	42.6	Depolarization =	0.000	Anaylsis Mode =	Linear
Substrate				**thickness**	**4.0 mm**

A.3 Box plots of IV parameters

The IV parameters for the series of samples deposited to evaluate the reproducibility of the fabrication procedure, are represented as box plots in figures A-2 and A-3.

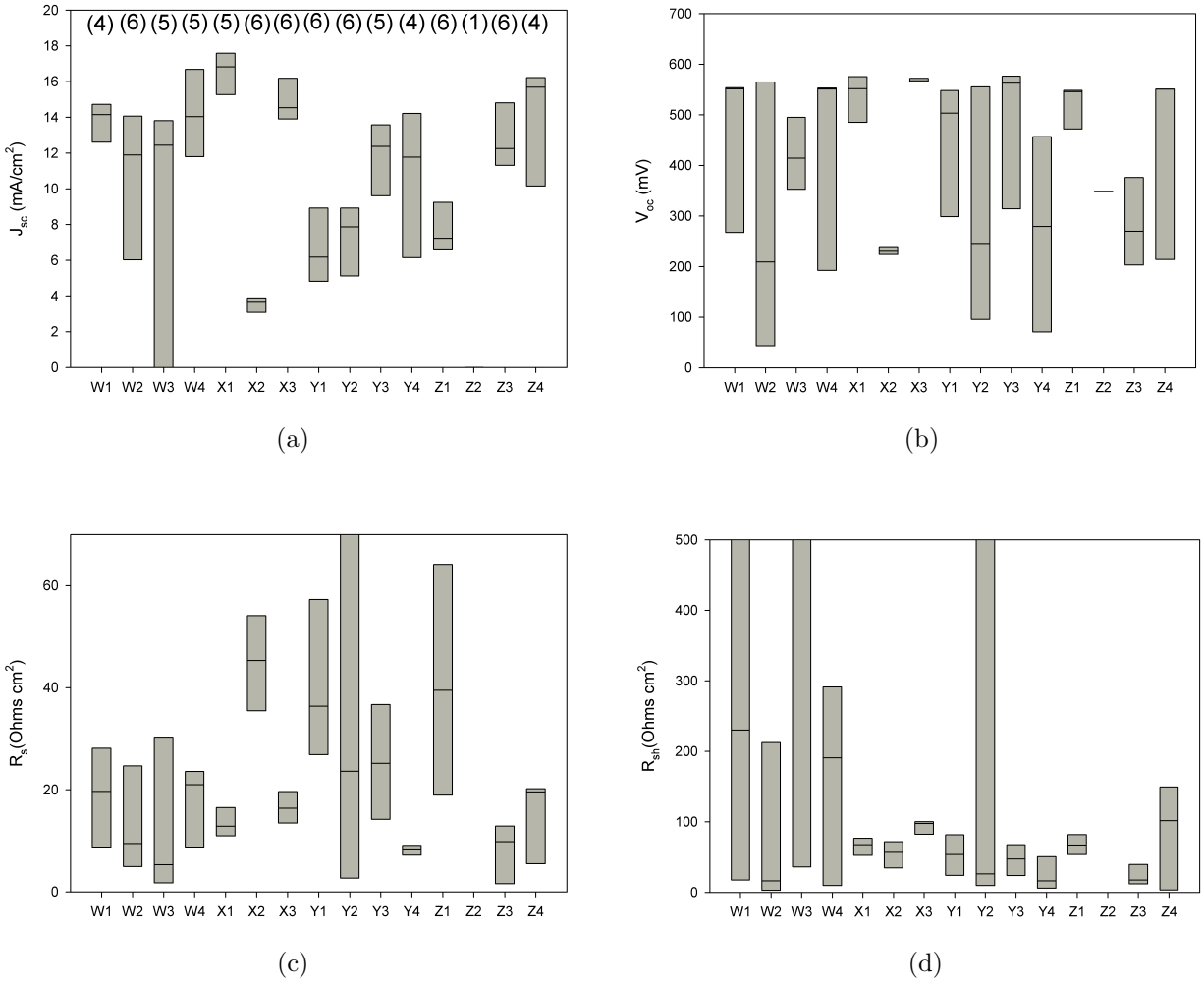

Figure A-2: The box plot for four of the IV parameters are presented; (a) short circuit current density, (b) open circuit voltage, (c) series resistance and (d) shunt resistance. The numbers in brackets in the short circuit current density plot show the number of cells which are represented for each of the samples.

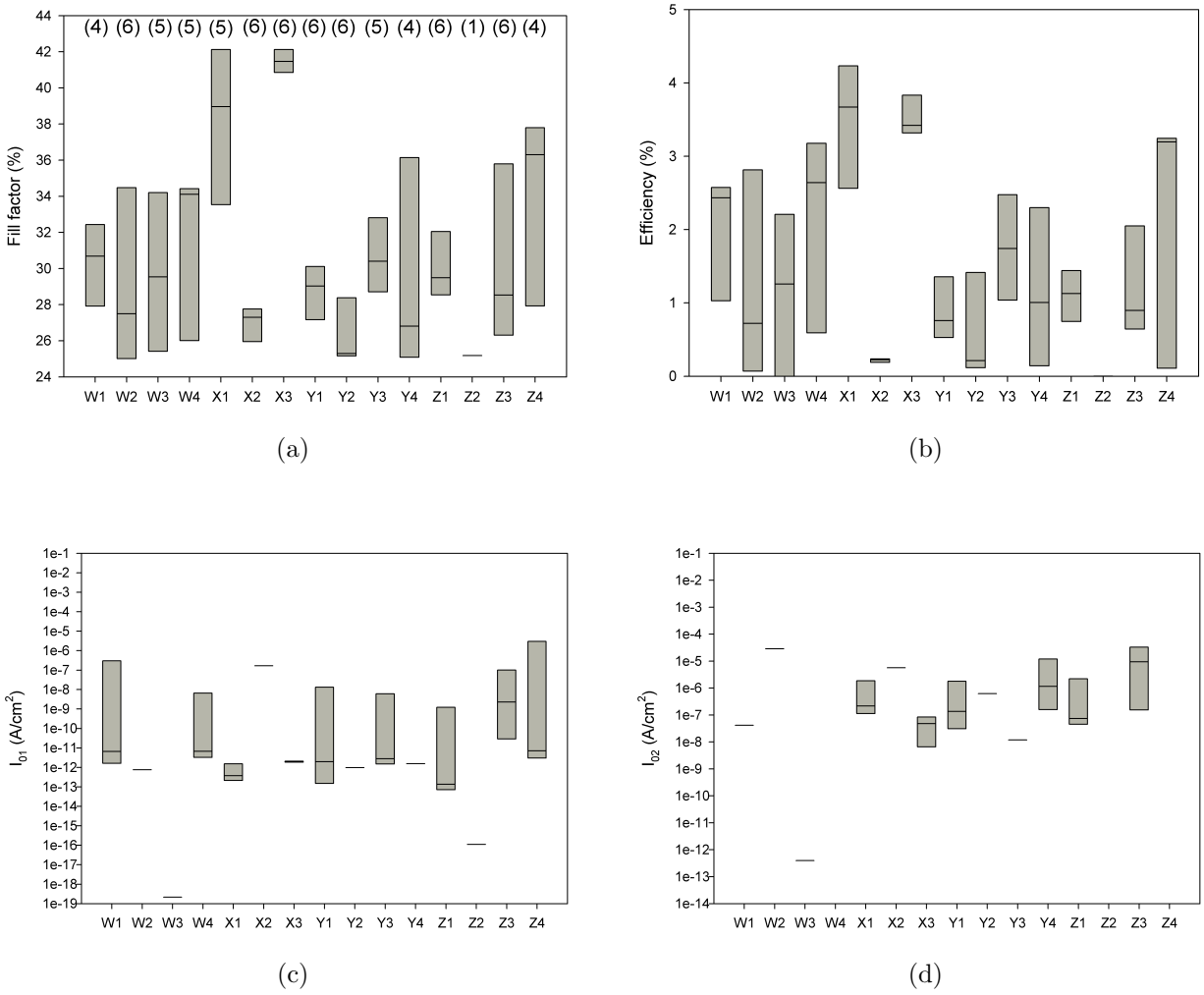

Figure A-3: The box plot for four of the IV parameters are presented; (a) fill factor, (b) efficiency, and the saturation current density for the two diodes in the model (c) and (d). The numbers in brackets in the fill factor plot show the number of cells which are represented for each of the samples.

The IV parameters for the series of samples which included CdS bilayers represented as box plots which can be seen in figure A-4 and A-5.

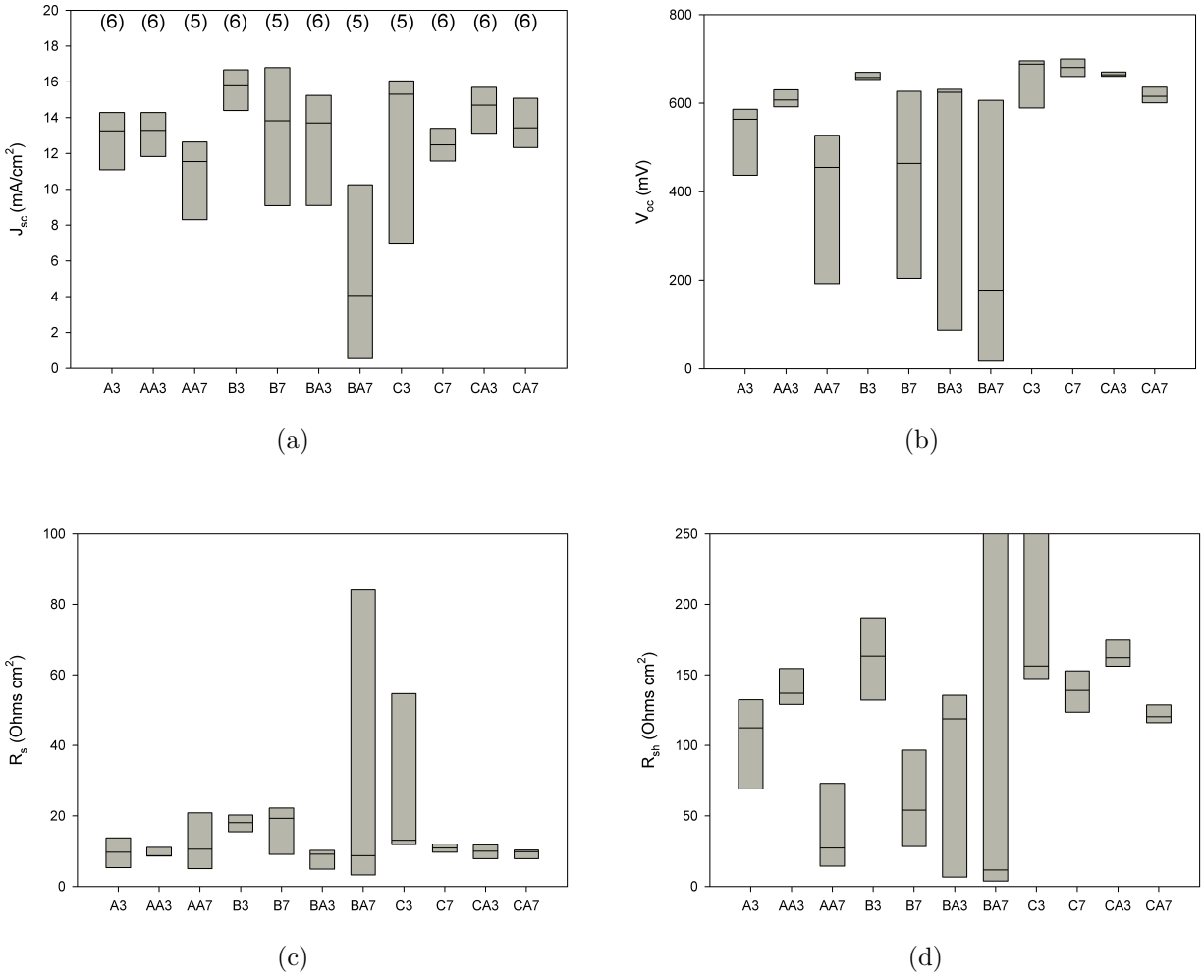

Figure A-4: The box plot for four of the IV parameters are presented; (a) short circuit current density, (b) open circuit voltage, (c) series resistance and (d) shunt resistance. The numbers in brackets in the short circuit current density plot show the number of cells which are represented for each of the samples.

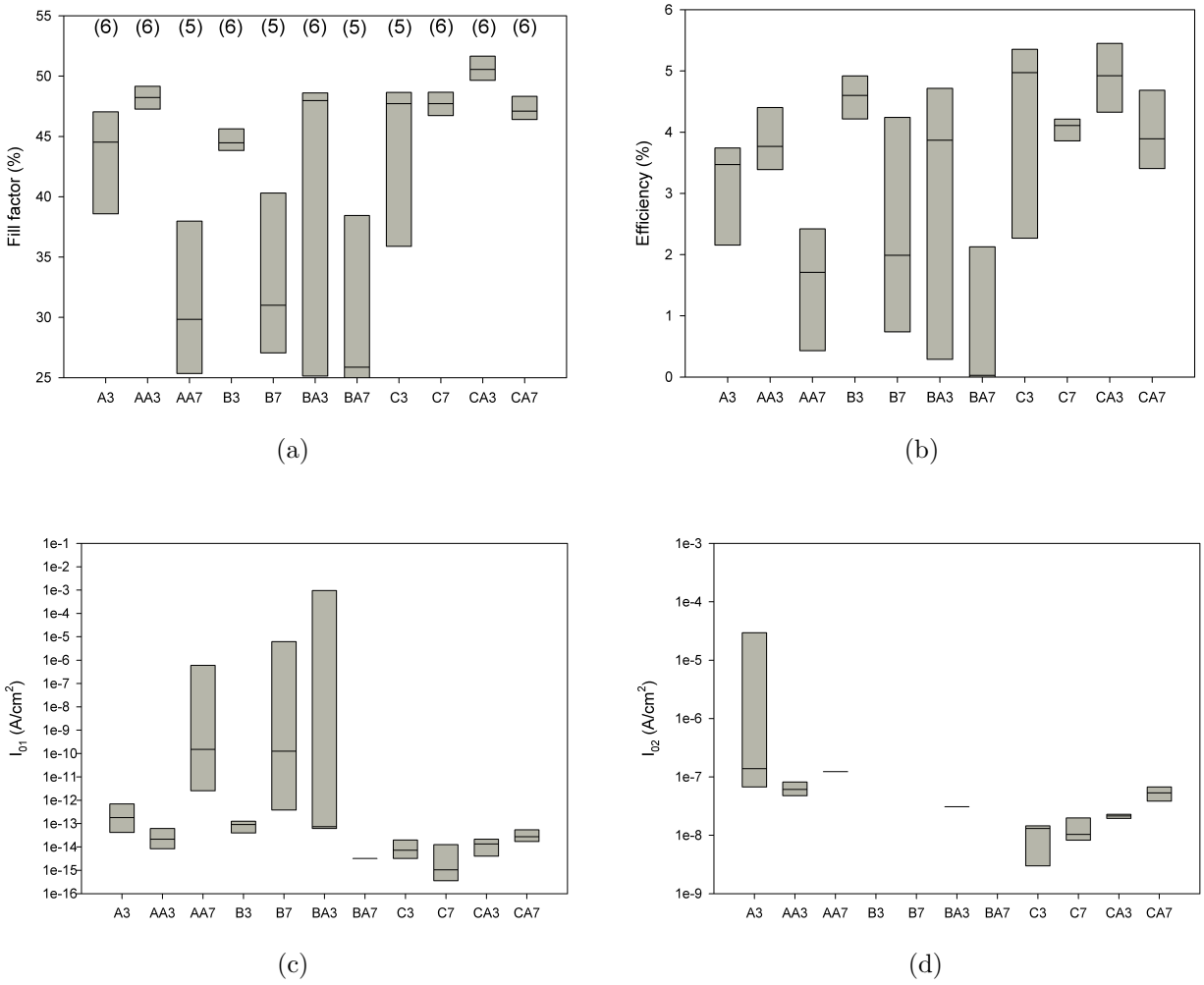

Figure A-5: The box plot for four of the IV parameters are presented; (a) fill factor,(b) efficiency, and the saturation current density for the two diodes in the model (c) and (d). The numbers in brackets in the fill factor plot show the number of cells which are represented for each of the samples.